PERGAMON

International Journal of Solids and Structures 38 (2001) 2335–2385

INTERNATIONAL JOURNAL OF SOLIDS and STRUCTURES

www.elsevier.com/locate/ijsolstr

A multi-level computational model for multi-scale damage analysis in composite and porous materials

Somnath Ghosh *, Kyunghoon Lee [1], Prasanna Raghavan

Department of Mechanical Engineering, The Ohio State University, 206 West 18th Avenue, Columbus, OH 43210, USA

Received 13 June 1999; in revised form 13 April 2000

Abstract

An adaptive multi-level methodology is developed in this paper to create a hierarchy of computational sub-domains with varying resolution for multiple scale problems. It is intended to concurrently predict evolution of variables at the structural and microstructural scales, as well as to track the incidence and propagation of microstructural damage in composite and porous materials. The microstructural analysis is conducted with the Voronoi cell finite element model (VCFEM), while a conventional displacement based FEM code executes the macroscopic analysis. The model introduces three levels in the computational domain which include macro, macro–micro and microscopic analysis. It differentiates between non-critical and critical regions and ranges from macroscopic computations using continuum constitutive relations to zooming in at 'hotspots' for pure microscopic simulations. Coupling between the scales in regions of periodic microstructure is accomplished through asymptotic homogenization. An adaptive process significantly increases the efficiency while retaining appropriate level of accuracy for each region. Numerical examples are conducted for composite and porous materials with a variety of microscopic architectures to demonstrate the potential of the model.

Keywords: Multi-level model; Voronoi cell FEM; Particle cracking; Adaptivity; Elastic–plastic

1. Introduction

Heterogeneous structures with second phase inclusions or voids in the microstructure are conventionally analyzed with macroscopic properties obtained from homogenization of response at smaller (meso, micro) length scales. The mathematical homogenization theory, which uses asymptotic expansions of displacement, strain and stress fields about macroscopic values, has been used as a tool for analyzing multiple scale responses in Benssousan et al. (1978), Sanchez-Palencia (1980), Parton and Kudryavtsev (1993) and Bakhvalov and Panasenko (1984). The method is based on the assumptions of spatial periodicity of microscopic representative volume elements (RVE) and local uniformity of macroscopic fields within each RVE. It decomposes the multiscale boundary value problem into a decoupled set of microscale RVE

* Corresponding author. Tel.: +1-614-292-2599; fax: +1-614-292-7369.
E-mail address: ghosh.5@osu.edu (S. Ghosh).
[1] Present address: Scientific Forming Technologies Corporation, Columbus, OH 43220, USA.

0020-7683/01/$ - see front matter
PII: S0020-7683(00)00167-0

problem and a macroscale problem. Concurrent finite element analyses are executed at each scale for information transfer between the scales. Multiple scale analysis of linear elastic reinforced composites by this method have been conducted by Fish and Belsky (1995), Fish and Wagiman (1993), Guedes and Kikuchi (1991) and Hollister and Kikuchi (1992). For non-linear materials, the homogenization methods have been extended by Suquet (1985), Fish et al. (1997), Guedes (1990) and Cheng (1992). The method has also been implemented to simulate damage by fiber–matrix debonding in linear elastostatics by Lene (1986) and fiber rupture using a phenomenological damage model by Devries et al. (1989).

Despite its advantages, asymptotic homogenization has suffered shortcomings arising from efficiency and accuracy considerations. Enormous computational efforts can result with this method due to the fact that at each integration point in the macroscopic model, boundary value problems of the microstructural RVE should be solved twice. To economize computations, many studies have assumed simple unit cell models of the microscopic RVE. Such idealizations may however be unrealistic for deformation and failure analysis of many materials. The homogenization method has another major limitation stemming from its basic assumptions, viz. (a) uniformity of the macroscopic fields within each RVE and (b) spatial periodicity of the RVE. The uniformity assumption is not appropriate in critical regions of high gradients, where the macroscopic fields can vary considerably. Free edges, interfaces, macrocracks, neighborhood of material discontinuities and most importantly in the regions of evolving microscopic damage and instability are the potential sites of non-uniformity. Furthermore, statistical periodicity implies that the RVE may be repeated to represent the entire neighborhood of a macroscopic point. For non-uniform microstructures, sufficiently large portions should be considered as RVE for homogenization analysis. Unit cell models are severely limited in this respect. Even higher-order theories of homogenization may be computationally unviable. A few effective global–local techniques based on hierarchical decomposition and superposition of field variables have been proposed by Belytschko et al. (1994), Robbins and Reddy (1996) and Hughes (1995). Pagano and Rybicki (1974) had discussed the breakdown of effective modulus theory for composite laminates with free edges and the need for global–local techniques. Fish and Belsky (1995) and Fish et al. (1994) have used global–local techniques with multigrid methods to extend the multiple scale modeling to non-periodic materials. Zohdi et al. (1996), Oden and Zohdi (1997) and Oden et al. (1999) have developed a homogenized Dirichlet projection method (HDPM), which resolves the microstructural effects at different scales on the macroscopic response of heterogeneous structures.

Adaptivity in the computational modules for multiple scale problems entails minimizing two types of errors, viz. the discretization error and the modeling error due to homogenized material properties as discussed in Oden and Zohdi (1997) and Oden et al. (1999). In the present work, an adaptive multi-level method is proposed to address the latter type of modeling error. It is aimed at improving the accuracy of analyses of elastic–plastic composite and porous structures with microstructural damage. The model uses computational hierarchy to concurrently predict the evolution of variables at structural and microstructural scales, as well as to track the incidence and propagation of microstructural damage. Analysis of microstructural response with arbitrary distributions, shapes and sizes of heterogeneities is conveniently done by the Voronoi Cell finite element model (VCFEM) (Moorthy and Ghosh, 1996, 1998; Ghosh et al., 1997). A high level of computational efficiency with sufficient accuracy and resolution has been achieved for elastic and elastic–plastic materials by this method. Progressive damage by particle cracking has been done in Ghosh and Moorthy (1998). Recently, an adaptive VCFEM has been successfully proposed by Moorthy and Ghosh (2000), where element adaptation is executed in two consecutive stages based on a-posteriori evaluation of error measures. In the first stage, displacement function adaptations are carried out by a *h*-refinement and *p*-enrichment strategy, which is followed by an enrichment of stress functions to reduce the error in kinematic relations.

For periodic RVE of elastic and elastic–plastic materials, the microstructural VCFEM has been coupled with structural analysis codes by using asymptotic homogenization in Ghosh et al. (1995, 1996). This method fails for problems, where assumptions of macroscopic uniformity and statistical periodicity are

questionable. Consequently, it becomes necessary to implement a combination of homogenization and global local methods, which is a non-trivial undertaking due to the lack of apriori knowledge of regions that require differential resolution. The multi-level methodology developed in this paper addresses this issue by differentiating between non-critical and critical regions and ranging from macroscopic computations using continuum constitutive relations to zooming in at 'hotspots' for pure microscopic simulations. The zoom-in is accomplished by a mesh-enrichment technique or *h*-adaptation, where macroscopic elements are successively dissected in regions of steep solution gradients. Also, the adaptations are based on local estimates of 'error' or solution gradients. The limitations of the *h*-adaptation and possible remedies are discussed in Section 12. The paper introduces three levels of the computational domain, for (a) fully macroscopic analysis with homogenized material parameters, (b) macro–microscopic analysis for periodic RVE's and (c) fully microscopic analysis. Additionally a new way of developing a piecewise continuous elastic–plastic constitutive model is presented in this paper. This model accounts for the details of microstructural morphology and variables. A number of numerical examples are solved with various microscopic architectures to support the development of this multi-level model.

2. Two way coupling for multiple scale modeling

Multiple scale modeling of heterogeneous materials is necessary to concurrently account for spatial variability at the macro and microscales. An effective model of this class requires two-way coupling for efficient computing, as well as for accurate representation of the necessary variables at different scales. The first is a 'bottom up' coupling for the determination of equivalent homogeneous behavior at a macroscopic point $\mathbf{x}$, as a function of the microstructural geometry and behavior of the constitutive phases, but independent of applied loads to the structure. In the homogenization procedure, an isolated RVE $Y(\mathbf{x}) \subset \Re^3$ is identified at microstructural scale of heterogeneities (Fig. 1(b)). The scale $\mathbf{y}$ of the RVE domain $Y(\mathbf{x})$ is large with respect to the characteristic length $\boldsymbol{l}$ of microscopic heterogeneities, but is significantly small compared

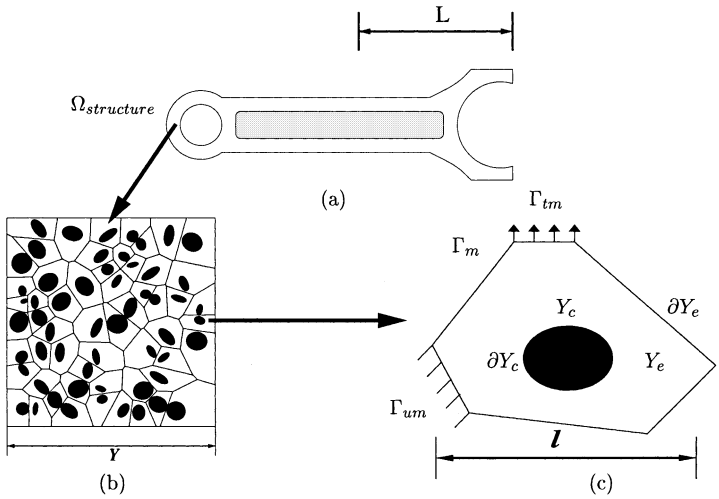

Fig. 1. A heterogeneous structure showing various scales (a) The structure at the macroscopic scale of applied loads (b) A representative volume element (RVE) at the microscopic scale with the VCFE model and (c) A Voronoi cell element at the scale of a single heterogeneity or basic structural element.

to the macroscopic length scale $\boldsymbol{L}$ of the structure and applied loads. Homogenized variables at the macroscopic scale are obtained by volume averaging of variables in the RVE, following the definition:

$$\langle f \rangle_{Y(\mathbf{x})} = \frac{1}{|Y|} \int_Y f(y) \mathrm{d}y \quad \text{where } |Y| = \int_Y \mathrm{d}Y. \tag{1}$$

The condition for macroscopic homogeneity, according to the Hill–Mandel hypothesis (Hill, 1965), assumes equivalence of strain energy for the actual and equivalent homogenized media. Thus, for a statically admissible stress field $\boldsymbol{\sigma}(\mathbf{y})$ and kinematically admissible strain field $\boldsymbol{\epsilon}(\mathbf{y})$,

$$\langle \boldsymbol{\sigma} : \boldsymbol{\epsilon} \rangle_Y = \langle \boldsymbol{\sigma} \rangle_Y : \langle \boldsymbol{\epsilon} \rangle_Y \quad \forall\ \mathbf{y} \in Y. \tag{2}$$

The microscopic stress $\boldsymbol{\sigma}(\mathbf{y})$ and strain $\boldsymbol{\epsilon}(\mathbf{y})$ fields satisfying the homogeneity condition (2) may be obtained by solving boundary value problems for the RVE Y with prescribed homogeneous stress/strain or periodicity boundary conditions, stated as

$$\begin{aligned}
&\text{uniform traction} \qquad \mathbf{T}^{\mathrm{b}} = \langle \boldsymbol{\sigma} \rangle_Y \cdot \mathbf{n}(\mathbf{y}) = \boldsymbol{\sigma} \cdot \mathbf{n}(\mathbf{y}) \quad \text{on } \partial Y, \\
&\text{uniform strain} \qquad \mathbf{u}^{\mathrm{b}} = \langle \boldsymbol{\epsilon} \rangle_Y \cdot \mathbf{y} \quad \text{on } \partial Y, \\
&Y\text{-periodicity} \qquad \mathbf{u}^{\mathrm{b}} = \langle \boldsymbol{\epsilon} \rangle_Y \cdot \mathbf{y} + \hat{\mathbf{u}}(\mathbf{y}) = \langle \boldsymbol{\epsilon} \rangle_Y \cdot \mathbf{y} + \hat{\mathbf{u}}(\mathbf{y} + \mathbf{k}\hat{\mathbf{Y}}) \quad \text{on } \partial Y,
\end{aligned} \tag{3}$$

where $\mathbf{k}$ is a 3×3 array of integers and $\hat{\mathbf{Y}}$ is the period of Y-periodic displacement functions $\hat{\mathbf{u}}$, interpreted as local perturbations to macroscopic strain based displacement fields. The macroscopic constitutive equations are obtained by solving a boundary value problem of the RVE Y with any one of the three sets of boundary conditions in Eqs. (3a)–(3c), followed by the averaging process in Eq. (1). For linear elastic constituent phases in Y, the relation between the strain energy functions has been established in Suquet (1987) as

$$\langle \boldsymbol{\epsilon} \rangle : \mathbf{E}^{\mathrm{h}}_{\mathrm{tr}} : \langle \boldsymbol{\epsilon} \rangle \leqslant \langle \boldsymbol{\epsilon} \rangle : \mathbf{E}^{\mathrm{h}}_{\mathrm{per}} : \langle \boldsymbol{\epsilon} \rangle \leqslant \langle \boldsymbol{\epsilon} \rangle : \mathbf{E}^{\mathrm{h}}_{\mathrm{str}} : \langle \boldsymbol{\epsilon} \rangle \quad \forall \mathbf{E} \subset \Re^9, \tag{4}$$

where $\mathbf{E}^{\mathrm{h}}_{\mathrm{tr}}, \mathbf{E}^{\mathrm{h}}_{\mathrm{per}}, \mathbf{E}^{\mathrm{h}}_{\mathrm{str}}$ are, respectively, the homogenized stiffness tensors evaluated with uniform traction, periodicity and uniform strain boundary conditions, and $\langle \boldsymbol{\epsilon} \rangle$ is the macroscopic (applied or averaged) strain field. The difference in stiffnesses with the kinematic and kinetic boundary conditions, reduce with decreasing sizes of Y. It is generally concluded by Hollister and Kikuchi (1992) that for the same RVE size, the periodicity boundary conditions are expected to yield more accurate statistically homogenized constitutive parameters and macroscopic properties.

The other coupling is the 'top down', where the evolution of variables are evaluated in the microstructure from known macroscopic variables, by a process termed as *localization*. In those regions, where the microstructure may admit a RVE Y, the microscopic variables can be evaluated by solving a boundary value problem with imposed macroscopic strains and the local periodicity condition in Eq. (3c). In other regions, where assumptions of local periodicity of the RVE may be unrealistic, the localization process will entail direct interfacing of the microstructural and macroscopic regions.

3. A multi-level model for coupling different scales

In the spirit of true two-way coupling of multiple scale problems, the computational domain in this paper is adaptively decomposed into three levels of hierarchy based on the requirements of the resolution. Such hierarchy is intended to increase computational efficiency as well as accuracy in concurrent prediction of variables at the continuum and microstructural scales. As proposed in Lee et al. (1999), the model uses homogenization of microstructural RVE solutions to evaluate homogenized properties and cascades down

the scales at hotspots of evolving damage. The three levels of hierarchy with requirements of increasing resolution (Fig. 2) are as follows:

(i) Computational subdomain level-0: These correspond to non-critical macroscopic regions in Fig. 2(a), where deformation variables are relatively uniform and periodicity conditions may be assumed for the underlying material RVE. Scale effects are negligible in this region and local constitutive relations may be derived from postulates of the RVE approaching zero volume. Continuum level anisotropic plasticity constitutive relations, that are consistent with the actual microstructural constitution, are developed for macroscopic modeling of these regions.

The level-0 macroscopic simulations are accompanied by element refinement or *h*-adaptation for two reasons. The first is to identify and reduce a chosen 'error measure' in the macroscopic computational model. A second attribute is that it enables the computational model to 'zoom in' on regions of evolving non-uniformity due to microscopic non-homogeneity. This reduces the disparity in size of the macro and micro scale elements by successive refinement of macroscopic elements in the critical regions as shown in Fig. 2a.

(ii) Computational subdomain level-1: These are regions that face imminent microscopic non-homogeneity and resulting macroscopic non-uniformities (Fig. 2(a) and (b)). Although, the computations are still macroscopic, concurrent monitoring of the development of damage and instabilities in the RVE is possible in this level. For concurrent macro and micro scale analyses the asymptotic homogenization methods,

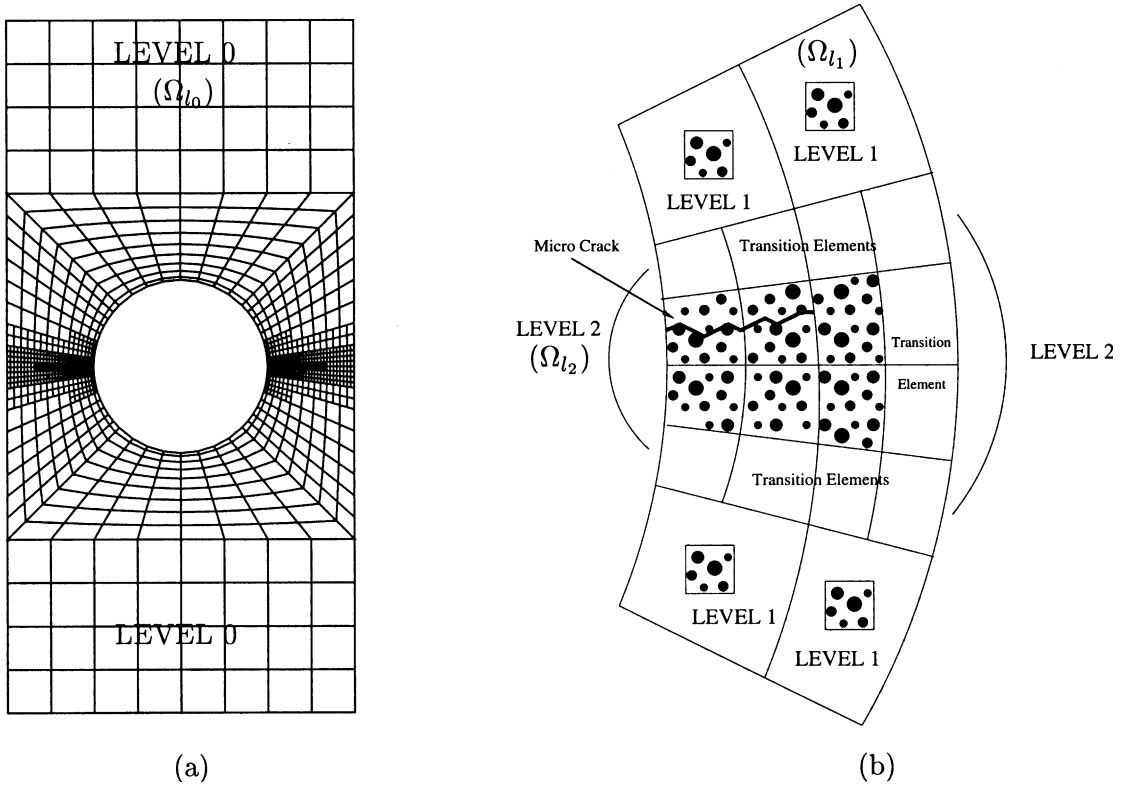

Fig. 2. A hierarchical multi-level computational domain; level-0 for macroscale continuum modeling (a) level-1 for coupled macro-microscopic (RVE) modeling with asymptotic homogenization and (b) level-2 for pure microscopic modeling.

which is based on the existence of an RVE, is used. Macroscopic element refinement by *h*-adaptation continues for this level.

(iii) Computational subdomain level-2: These critical regions materialize with the evolution of microstructural damage in the form of evolved microcracks or instabilities (Fig. 2(b)), leading to high macroscopic field gradients. The assumptions of macroscopic uniformity and local periodicity are unrealistic. To realize scale effects, it is required that the level-1 macro–micro computational model switch to a completely microscopic model, encompassing large portions of the microstructure. A detailed flow chart of the adaptive hierarchical process is depicted in Fig. 3.

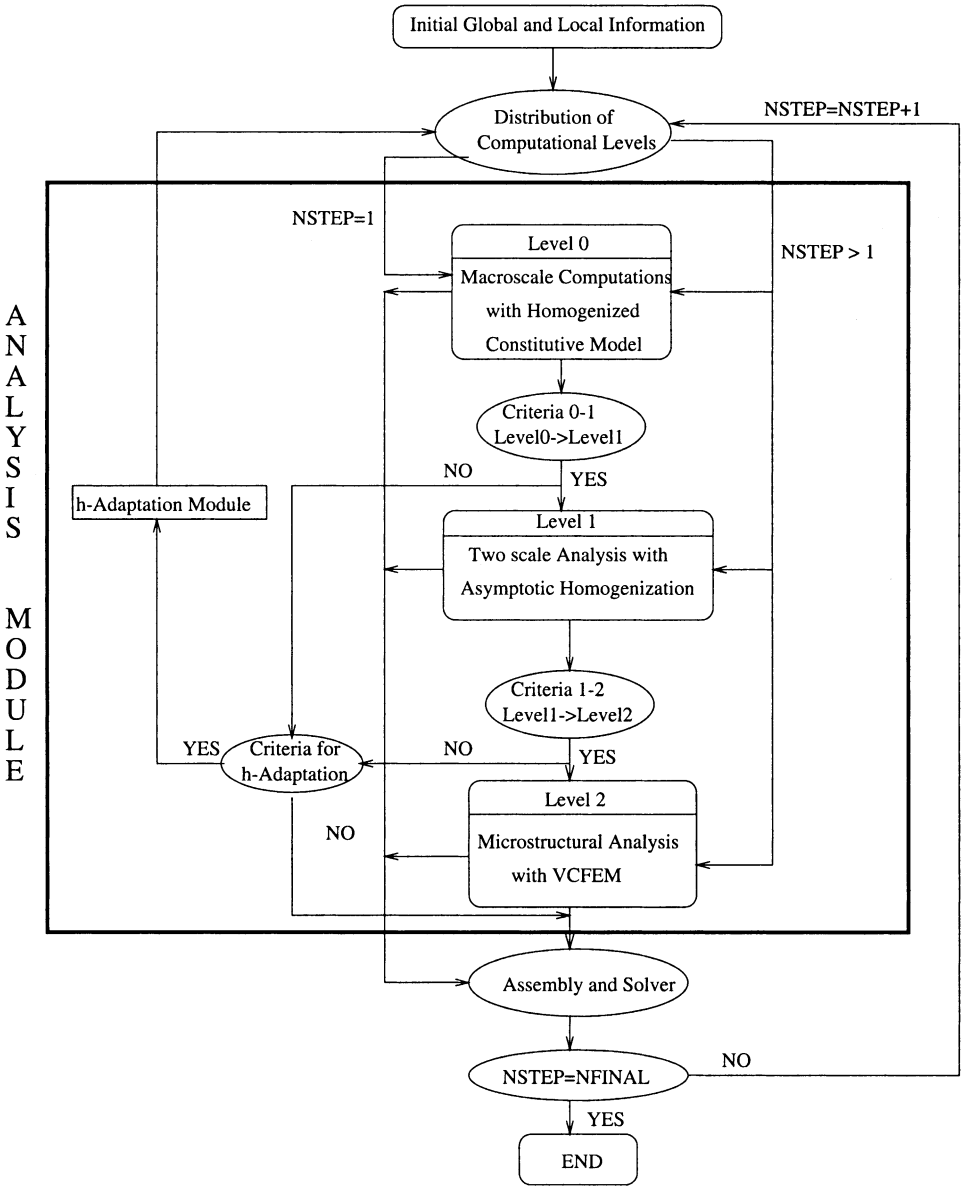

Fig. 3. Flow chart of the sequence of operations in the multiple-scale model.

The substructured computational domain is delineated as an elastic–plastic body of material domain Ω_{MAT} that consists of regions $\Omega_{\mathrm{MAT(p)}}$ for which the RVE is repeated periodically, and also of regions $\Omega_{\mathrm{MAT(np)}}$ where the periodicity assumptions do not hold, i.e.

$$\Omega_{\mathrm{MAT}}(\mathbf{x},\mathbf{u}) = \Omega_{\mathrm{MAT(p)}}(\mathbf{x},\mathbf{u}) \cup \Omega_{\mathrm{MAT(np)}}(\mathbf{x},\mathbf{u}). \tag{5}$$

The macroscopic regions of periodicity are further constituted of repeating a large number of RVEs Y, i.e.

$$\Omega_{\mathrm{MAT(p)}} = \cup_{k=1}^{N(\mathrm{p})} \bar{Y}_k^{\mathrm{MAT(p)}}, \quad \text{where} \quad \bar{Y}_k^{\mathrm{MAT(p)}} = \cup_{l=1}^{\infty} Y_k^l. \tag{6}$$

Here $N(\mathrm{p})$ corresponds to the number of different RVE's Y_k^l in the periodic regions, and for all practical purposes, ∞ corresponds to a sufficiently large number. The non-periodic region $\Omega_{\mathrm{MAT(np)}}$ is defined as the set of all microstructural regions for which the $N(\mathrm{np})$ RVE's are not repeated, i.e.

$$\Omega_{\mathrm{MAT(np)}} = \cup_{k=1}^{N(\mathrm{np})} Y_k^{\mathrm{MAT(np)}}, \quad Y_k \cap Y_l = 0 \ \ \forall k \neq l. \tag{7}$$

The level-0 and level-1 of the computational domain Ω correspond to the periodic regions, while the level-2 belongs to the non-periodic regions as

$$\Omega_{\mathrm{l0}} \cup \Omega_{\mathrm{l1}} \subset \Omega_{\mathrm{MAT(p)}}, \qquad \Omega_{\mathrm{l2}} \subset \Omega_{\mathrm{MAT(np)}}. \tag{8}$$

4. Homogenization with Voronoi cell finite element method

4.1. Asymptotic homogenization with microstructural periodicity

Consider a heterogeneous structure occupying a region $\Omega_{\mathrm{structure}}$ (Fig. 1a), for which the heterogeneous microstructure constitutes of spatially repeated RVEs $Y(\mathbf{x})$ about a macroscopic point $\mathbf{x}$ as shown in Fig. 1b. The RVE is discretized into a mesh of Voronoi cells, which naturally evolve from the microstructure by Dirichlet tessellation. In the Voronoi cell finite element method (VCFEM), each Voronoi cell represents a basic structural element (BSE), which is the neighborhood of a heterogeneity in the microstructure. The dimensions of the $Y(\mathbf{x})$ are typically very small in comparison with the structural dimensions L, i.e. l/L is a very small positive number ϵ. Due to variation of evolutionary variables in a small neighborhood ϵ of the macroscopic point $\mathbf{x}$, all variables are assumed to exhibit dependence on both length scales i.e. $\Phi^\epsilon = \Phi(\mathbf{x},\mathbf{x}/\epsilon)$, where $\mathbf{y} = \mathbf{x}/\epsilon$. The superscript ϵ denotes association of the function with the two length scales and hence Ω^ϵ corresponds to a connected structural and microstructural domain. The assumption of periodic repetition of the microstructure about $\mathbf{x}$ makes the dependence of the function on $\mathbf{y}(=\mathbf{x}/\epsilon)$, Y-periodic (Bakhvalov and Panasenko, 1984; Guedes and Kikuchi, 1991; Hollister and Kikuchi, 1992; Devries et al., 1989). For small deformation elasto-plasticity, the rate forms of the equilibrium, kinematic and constitutive relations are given as

$$\begin{aligned} &\text{Equilibrium} \quad \dot{\sigma}^\epsilon_{ij,j} = -\dot{f}_i, \qquad \text{Kinematics} \quad \dot{e}^\epsilon_{kl} = \tfrac{1}{2}\left(\frac{\partial \dot{u}^\epsilon_k}{\partial x^\epsilon_l} + \frac{\partial \dot{u}^\epsilon_l}{\partial x^\epsilon_k}\right), \\ &\text{Constitutive} \quad \dot{\sigma}^\epsilon_{ij} = E^\epsilon_{ijkl}\dot{e}^\epsilon_{kl} \quad \text{in } \Omega^\epsilon, \end{aligned} \tag{9}$$

where $\dot{\sigma}^\epsilon_{ij}(\mathbf{x},\mathbf{y})$, $\dot{e}^\epsilon_{ij}(\mathbf{x},\mathbf{y})$ and $\dot{u}^\epsilon_i(\mathbf{x},\mathbf{y})$ are Y-periodic rates of stress, strain and displacement fields, respectively. Furthermore, the periodic boundary conditions may be specified as

$$\dot{u}^\epsilon_i(\mathbf{x},\mathbf{y}) = \dot{u}^\epsilon_i(\mathbf{x},\mathbf{y}+\mathbf{kY}) \quad \text{on RVE boundary } \partial Y \quad \text{and} \quad \dot{\sigma}^\epsilon_{ij} \text{ is continuous across } \partial Y. \tag{10}$$

The Y-periodic displacement rate field is approximated by an asymptotic expansion about $\mathbf{x}$ with respect to the parameter ϵ:

$$\dot{u}_i^{\epsilon}(\mathbf{x}) = \dot{u}_i^0(\mathbf{x},\mathbf{y}) + \epsilon\dot{u}_i^1(\mathbf{x},\mathbf{y}) + \epsilon^2\dot{u}_i^2(\mathbf{x},\mathbf{y}) + \cdots, \quad \mathbf{y} = \mathbf{x}/\epsilon. \tag{11}$$

Noting that the spatial $\mathbf{x}^{\epsilon}$ derivative of any function depends on the two length scales and is given as

$$\frac{\partial}{\partial x_i^{\epsilon}}\left(\Phi\left(\mathbf{x},\mathbf{y}=\frac{\mathbf{x}}{\epsilon}\right)\right) = \frac{\partial\Phi}{\partial x_i} + \frac{1}{\epsilon}\frac{\partial\Phi}{\partial y_i}, \tag{12}$$

the stress rate tensor $\dot{\sigma}_{ij}^{\epsilon}$ can be expressed as

$$\dot{\sigma}_{ij}^{\epsilon} = \frac{1}{\epsilon}\dot{\sigma}_{ij}^0 + \dot{\sigma}_{ij}^1 + \epsilon\dot{\sigma}_{ij}^2 + \epsilon^2\dot{\sigma}_{ij}^3\cdots \tag{13}$$

where

$$\dot{\sigma}_{ij}^0 = E_{ijkl}^{\epsilon}\frac{\partial\dot{u}_k^0}{\partial y_l}, \qquad \dot{\sigma}_{ij}^1 = E_{ijkl}^{\epsilon}\left(\frac{\partial\dot{u}_k^0}{\partial x_l} + \frac{\partial\dot{u}_k^1}{\partial y_l}\right), \qquad \dot{\sigma}_{ij}^2 = E_{ijkl}^{\epsilon}\left(\frac{\partial\dot{u}_k^1}{\partial x_l} + \frac{\partial\dot{u}_k^2}{\partial y_l}\right). \tag{14}$$

From Eqs. (9) and (13), and using the periodicity condition on the RVE boundary $\int_{\mathrm{d}\Gamma_Y} f\,\mathrm{d}\Gamma_Y = 0$, it can be proved (Ghosh et al., 1995, 1996) that

$$\dot{\sigma}_{ij}^0 = 0, \quad \dot{u}_i^0 = \dot{u}_i^0(\mathbf{x}) \quad \text{and} \quad \frac{\partial\dot{\sigma}_{ij}^1}{\partial y_j} = \frac{\partial}{\partial y_j}\left[E_{ijkl}^{\epsilon}\left\{\frac{\partial\dot{u}_k^0}{\partial y_l} + \frac{\partial\dot{u}_k^1}{\partial y_l}\right\}\right] = 0. \tag{15}$$

By neglecting the terms associated with ϵ or higher in Eq. (13), the constitutive relation in the Y-domain is expressed as

$$\dot{\sigma}_{ij}^{\epsilon} = \dot{\sigma}_{ij}^1 = E_{ijkl}^{\epsilon}\dot{e}_{kl}^{\epsilon} = E_{ijkl}^{\epsilon}\left(\frac{\partial\dot{u}_k^0}{\partial x_l} + \frac{\partial\dot{u}_k^1}{\partial y_l}\right). \tag{16}$$

Here $\dot{e}_{kl}^{\epsilon}$ is the microstructural strain rate tensor, for which $e_{kl} = \frac{1}{2}(\partial\dot{u}_k^0/\partial x_l + \partial\dot{u}_l^0/\partial x_k)$ is an averaged macroscopic part and $e_{kl}^1 = \frac{1}{2}(\partial\dot{u}_k^1/\partial y_l + \partial\dot{u}_l^1/\partial y_k)$ is denoted as a fluctuating strain rate tensor (Suquet, 1985). Due to linearity of the rate problem, $\dot{\sigma}_{ij}^1$, $\dot{u}_i^1$ and the microscopic equilibrium condition can be expressed as

$$\dot{\sigma}_{ij}^1 = \hat{\sigma}_{ij}^{kl}(\mathbf{y})\frac{\partial\dot{u}_k^0}{\partial x_l}, \qquad \dot{u}_i^1 = \chi_i^{kl}(\mathbf{y})\frac{\partial\dot{u}_k^0}{\partial x_l}, \qquad \frac{\partial\hat{\sigma}_{ij}^{kl}(\mathbf{y})}{\partial y_j} = 0. \tag{17}$$

In Eq. (17), $\hat{\sigma}_{ij}^{kl}$ is a Y-antiperiodic function and χ_i^{kl} is a Y-periodic function representing characteristic modes of the deformation in the RVE. Substituting Eq. (17) in the constitutive relations of Eq. (9) yields the microscopic constitutive relations as

$$\hat{\sigma}_{ij}^{kl}(\mathbf{y}) = E_{ijpm}^{\epsilon}\left[\delta_{kp}\delta_{lm} + \frac{\partial\chi_p^{kl}}{\partial y_m}\right], \tag{18}$$

where δ_{ij} is Kronecker delta. The mean of Eq. (18) yields the homogenized elastic–plastic tangent modulus for use in the macroscopic analysis, in the form

$$E_{ijkl}^{\mathrm{H}} = \langle\hat{\sigma}_{ij}^{kl}\rangle_Y = \frac{1}{|Y|}\int_Y \hat{\sigma}_{ij}^{kl}\mathrm{d}Y = \frac{1}{|\mathbf{Y}|}\int_Y E_{ijpm}^{\epsilon}\left(\delta_{kp}\delta_{lm} + \frac{\partial\chi_p^{kl}}{\partial y_m}\right)\mathrm{d}Y. \tag{19}$$

The macroscopic stress and strain relation can thus be stated as

$$\dot{\Sigma}_{ij}(\mathbf{x}) = \left\langle E^{\epsilon}_{ijkl}\left(\delta_{km}\delta_{ln} + \frac{\partial \chi^{mn}_{k}}{\partial y_l}\right)\frac{\partial \dot{u}^{0}_{m}}{\partial x_n}\right\rangle_{Y} = E^{\mathrm{H}}_{ijmn}\dot{e}_{mn}(\mathbf{x}), \tag{20}$$

where the homogenized variables are $\Sigma(\mathbf{x}) = \langle \boldsymbol{\sigma}^{\epsilon}(\mathbf{x},\mathbf{y})\rangle_Y$ and $\mathbf{e}(\mathbf{x}) = \langle \boldsymbol{\epsilon}^{\epsilon}(\mathbf{x},\mathbf{y})\rangle_Y$. The incremental small deformation analysis for elastic–plastic materials can be conducted with the homogenized modulus at the macroscopic level and by using the VCFEM for solving the microscopic problem.

4.2. The Voronoi cell finite element method for microstructural analysis

The VCFEM has been successfully developed for composite and porous materials in Moorthy and Ghosh (1996, 1998, 2000). Arbitrary dispersion patterns, shapes and sizes of heterogeneities are readily modeled by VCFEM. The computational model naturally evolves by Dirichlet tessellation of the microstructure as shown in Fig. 1b. Each Voronoi cell with the embedded inclusion or void is treated as an element in this formulation. In Moorthy and Ghosh (1998), the VCFEM formulation has been extended to include damage evolution in the form of particle cracking, where the crack is realized as an elliptical void. Each Voronoi cell element is amenable to change in topology from two constituent phases (matrix and inclusions) in undamaged cells, to three phases (matrix, inclusion and crack) in damaged cells. Complete particle cracking or splitting is assumed to occur at the very onset of damage.

The VCFE formulation constructs a hybrid element by combining the aspects of finite element methods with important micromechanics considerations. Use of a hybrid stress based formulation results in a high level of accuracy with a significantly reduced degree of freedom, compared to displacement based FEM models. Consider a typical representative volume element Y consisting of N undamaged and/or damaged particles, that are contained in each of the N Voronoi cell elements, as shown in Fig. 1(b). In VCFEM, the RVE Y comprises the Voronoi cell elements Y_e, i.e. $Y = \cup_{e=1}^{N} Y_e$. The assumed stress hybrid formulation in VCFEM requires independent assumptions of an equilibriated stress field ($\boldsymbol{\sigma}$) in each of the matrix and inclusion phases of each element $Y_e = Y_e^{\mathrm{m}} \cup Y_e^{\mathrm{c}}$, and compatible displacement fields $\mathbf{u}$ on the element boundary ∂Y_e, $\mathbf{u}'$ on the matrix-inclusion interface ∂Y_{c} and $\mathbf{u}''$ on the crack boundary ∂Y_{cr}. In an incremental formulation for elasto-plasticity, the incremental variational formulation introduces an element energy functional,

$$\begin{aligned}
\Pi_e^C(\Delta\boldsymbol{\sigma},\Delta\mathbf{u}) = &-\int_{Y_e}\Delta B(\boldsymbol{\sigma},\Delta\boldsymbol{\sigma})\,\mathrm{d}Y - \int_{Y_e}\boldsymbol{\epsilon}:\Delta\boldsymbol{\sigma}\,\mathrm{d}Y \\
&+\int_{\partial Y_e}(\boldsymbol{\sigma}+\Delta\boldsymbol{\sigma})\cdot\mathbf{n}^{\mathrm{e}}\cdot(\mathbf{u}+\Delta\mathbf{u})\,\mathrm{d}\partial Y \quad \text{(inter-element traction reciprocity)} \\
&-\int_{\Gamma_{tm}}(\bar{\mathbf{t}}+\Delta\bar{\mathbf{t}})\cdot(\mathbf{u}+\Delta\mathbf{u})\,\mathrm{d}\Gamma \quad \text{(boundary traction)} \\
&-\int_{\partial Y_{\mathrm{c}}}(\boldsymbol{\sigma}^{\mathrm{m}}+\Delta\boldsymbol{\sigma}^{\mathrm{m}}-\boldsymbol{\sigma}^{\mathrm{c}}-\Delta\boldsymbol{\sigma}^{\mathrm{c}})\cdot\mathbf{n}^{\mathrm{c}}\cdot(\mathbf{u}'+\Delta\mathbf{u}')\,\partial Y \quad \text{(matrix-inclusion interface traction)} \\
&-\int_{\partial Y_{\mathrm{cr}}}(\boldsymbol{\sigma}^{\mathrm{c}}+\Delta\boldsymbol{\sigma}^{\mathrm{c}})\cdot\mathbf{n}^{\mathrm{cr}}\cdot(\mathbf{u}''+\Delta\mathbf{u}'')\,\partial Y \quad \text{(crack boundary traction)},
\end{aligned} \tag{21}$$

where ΔB is the increment of complimentary energy density. Variables ($\boldsymbol{\sigma}$,$\mathbf{u}$) correspond to values at the beginning of an increment, while variables ($\Delta\boldsymbol{\sigma}$, $\Delta\mathbf{u}$) are the corresponding increments in a load increment or step. Outward normals on ∂Y_e, ∂Y_{c} and ∂Y_{cr} are denoted by $\mathbf{n}^{\mathrm{e}}$, $\mathbf{n}^{\mathrm{c}}$ and $\mathbf{n}^{\mathrm{cr}}$ respectively. Superscripts m, c and cr are associated with the matrix, inclusion and crack phases, respectively, in each Voronoi cell element. The total energy for the entire RVE of N Voronoi cells is obtained as $\Pi^C = \sum_{e=1}^{N}\Pi_e^C$. Setting the first variation of Π_e^C in Eq. (21) with respect to stress increments $\Delta\boldsymbol{\sigma}$ to zero yields the element compatibility as

the Euler equation, while setting the first variations of Π^C with respect to the independent boundary displacements $\Delta\mathbf{u}$, $\Delta\mathbf{u}'$ and $\Delta\mathbf{u}''$ to zero, yield the inter-element boundary traction reciprocity, matrix-inclusion interface traction reciprocity and zero traction crack boundary condition, respectively. Independent assumptions on stress increments $\Delta\boldsymbol{\sigma}$ are made in the matrix and inclusion phases in each element, thus allowing stress discontinuities across the interface. In this process special forms of Airy's stress function $\boldsymbol{\Phi}(x,y)$ to enhance computational efficiency, has been developed in Moorthy and Ghosh (1996, 1998) for equilibriated stress fields. The functions facilitate stress concentration near the interface and crack boundary, accounting for the shape of the inclusion and crack and also help satisfy traction reciprocity at the interfaces ∂Y_c and ∂Y_{cr}. Furthermore, they decay at large distances from the interfaces. Compatible displacement increments are generated on each of the boundaries/interfaces ∂Y_e, ∂Y_c and ∂Y_{cr} by interpolating nodal displacements using polynomial shape functions. The stress and displacement interpolations may be expressed as

$$\begin{aligned}
&\{\Delta\boldsymbol{\sigma}^m\} = [\mathbf{P}^m(x,y)]\{\Delta\boldsymbol{\beta}^m\} \quad \text{(in matrix)} \quad \text{and} \quad \{\Delta\boldsymbol{\sigma}^c\} = [\mathbf{P}^c(x,y)]\{\Delta\boldsymbol{\beta}^c\} \quad \text{(in inclusion)},\\
&\{\Delta\mathbf{u}\} = [\mathbf{L}^e]\{\Delta\mathbf{q}\} \quad \text{(on element boundary)},\\
&\{\Delta\mathbf{u}'\} = [\mathbf{L}^c]\{\Delta\mathbf{q}'\} \quad \text{(on interface)}, \quad \text{and} \quad \{\Delta\mathbf{u}''\} = [\mathbf{L}^{cr}]\{\Delta\mathbf{q}''\} \quad \text{(on crack face)},
\end{aligned} \tag{22}$$

where $\{\Delta\mathbf{q}\}$, $\{\Delta\mathbf{q}'\}$ and $\{\Delta\mathbf{q}''\}$ are the nodal displacement increment vectors, and $[\mathbf{L}^e]$, $[\mathbf{L}^c]$ and $[\mathbf{L}^{cr}]$ are the corresponding interpolation matrices.

4.3. Coupling asymptotic homogenization with Voronoi cell frame element model

In the incremental formulation, the equilibriated microscopic stress increment corresponds to $\Delta\boldsymbol{\sigma}^1(=\Delta\boldsymbol{\sigma}^\epsilon)$ in Eq. (17) and the microstructural strain increments are designated as $\Delta\boldsymbol{e}^\epsilon$ in Eq. (16). Similarly, the increments in microscopic displacements on the cell boundaries ∂Y_e are identified with $\Delta\mathbf{u}^1$ in Eq. (17) and those on the interface and crack surface are denoted by $\Delta\mathbf{u}^{1\prime}$ and $\Delta\mathbf{u}^{1\prime\prime}$, respectively. In the absence of explicit traction boundaries due to periodicity conditions on the boundary, the incremental energy functional for each Voronoi cell element in Eq. (21) is modified for the asymptotic homogenization process as

$$\begin{aligned}
\Pi_e^C = &-\int_{Y_e}\frac{1}{2}S^\epsilon_{ijkl}\Delta\sigma^\epsilon_{ij}\Delta\sigma^\epsilon_{kl}\,\mathrm{d}Y - \int_{Y_e}\boldsymbol{\epsilon}^\epsilon : \Delta\boldsymbol{\sigma}^\epsilon \mathrm{d}Y\\
&+\int_{\partial Y_e}(\boldsymbol{\sigma}^\epsilon+\Delta\boldsymbol{\sigma})^\epsilon\cdot\mathbf{n}^e\cdot(\mathbf{u}^1+\Delta\mathbf{u}^1)\,\mathrm{d}\partial Y - \int_{\partial Y_c}(\boldsymbol{\sigma}^{\epsilon m}+\Delta\boldsymbol{\sigma}^{\epsilon m}-\boldsymbol{\sigma}^{\epsilon c}-\Delta\boldsymbol{\sigma}^{\epsilon c})\cdot\mathbf{n}^c\cdot(\mathbf{u}^{1\prime}+\Delta\mathbf{u}^{1\prime})\partial Y\\
&-\int_{\partial Y_{cr}}(\boldsymbol{\sigma}^{\epsilon c}+\Delta\boldsymbol{\sigma}^{\epsilon c})\cdot\mathbf{n}^{cr}\cdot(\mathbf{u}^{1\prime\prime}+\Delta\mathbf{u}^{1\prime\prime})\,\partial Y + \int_{Y_e}(\mathbf{e}+\Delta\mathbf{e})\Delta\boldsymbol{\sigma}^\epsilon \mathrm{d}Y,
\end{aligned} \tag{23}$$

where S^ϵ_{ijkl} is an instantaneous elastic–plastic compliance tensor. The last term in Eq. (23) incorporates the effect of macroscopic strains $\mathbf{e}$ in the microstructure. The stationary condition of Π_e^C with respect to stress increment $\Delta\sigma^\epsilon_{ij}$ yields as Euler's equations, the incremental form of kinematic relations

$$e^\epsilon_{ij}+\Delta e^\epsilon_{ij} = e_{ij}+\Delta e_{ij}+\frac{\partial(u_i^1+\Delta u_i^1)}{\partial y_j} \text{ in the element matrix and inclusion phases.} \tag{24}$$

Stationarity of the total energy functional $\Pi^C=\sum_{e=1}^N\Pi_e^C$ with respect to displacement increments Δu_i^1, $\Delta u_i^{1\prime}$ and $\Delta u_i^{1\prime\prime}$, result in the inter-element, interface and crack boundary traction reciprocity conditions, respectively.

$$
\begin{aligned}
&(\sigma_{ij}^{\epsilon} + \Delta\sigma_{ij}^{\epsilon}) \cdot n_j^{e+} = -(\sigma_{ij}^{\epsilon} + \Delta\sigma_{ij}^{\epsilon}) \cdot n_j^{e-} \quad \text{on } \partial Y_e,\\
&(\sigma_{ij}^{\epsilon c} + \Delta\sigma_{ij}^{\epsilon c}) \cdot n_j^{c} = (\sigma_{ij}^{\epsilon m} + \Delta\sigma_{ij}^{\epsilon m}) \cdot n_j^{c} \quad \text{on } \partial Y_c,\\
&(\sigma_{ij}^{\epsilon c} + \Delta\sigma_{ij}^{\epsilon c}) \cdot n_j^{cr} = 0 \quad \text{on } \partial Y_{cr}.
\end{aligned} \tag{25}
$$

The microscopic VCFEM module is executed for two purposes in each increment of the macroscopic module. The first is to evaluate the microscopic stress increments $\Delta\boldsymbol{\sigma}^{\epsilon}$ from the given values of the macroscopic strain $\bar{\mathbf{e}}$ at the beginning of the step, and its increment $\Delta\bar{\mathbf{e}}$. The second is to calculate the instantaneous homogenized tangent modulus E_{ijkl}^{H} at the end of the increment in the macroscopic module. The details of the calculation of microscopic stress and homogenized tangent modulus calculation procedure are given in Ghosh et al. (1995, 1996). The VCFEM is incorporated in a macroscopic analysis module with the interface being created by the homogenization procedure. The macroscopic analysis is performed using a displacement based finite element code with plane strain QUAD4 elements. Numerical integration in these elements uses one-point reduced integration and hourglass control (Koh and Kikuchi, 1987). Material constitutive relations at each integration point of elements are obtained from homogenization of microscopic VCFEM results. Microscopic stresses σ_{ij}^{ϵ} are averaged to yield macroscopic stresses Σ_{ij}. The microscopic VCFEM is also invoked to evaluate the homogenized elastic–plastic tangent modulus E^{H} by applying unit components of macroscopic strain.

5. Computational subdomain level-0 in the hierarchical model

Level-0 corresponds to macroscopic regions ($\Omega_{l0} \subset \Omega_{MAT(p)}$) in Fig. 2a, where deformation variables like stresses and strains are relatively uniform in their macroscopic behavior. Scale effects are negligible and local constitutive relations may be derived from postulates of zero RVE volume in the limit and periodicity. It is assumed that macroscopic analyses with homogenized constitutive relations are sufficient for these regions. Anisotropic constitutive relations with varying parameters are developed for continuum analysis of heterogeneous microstructures with elastic–plastic constituent phases. To account for the details of microstructural morphology, the constitutive model is based on two-scale analysis using the asymptotic homogenization method and microstructural analysis by VCFEM. A continuum constitutive model can greatly enhance computational efficiency over two-scale analysis.

5.1. An elastic–plastic constitutive model

Various continuum constitutive models have been proposed, based on unit cell analyses of composite and porous microstructures. One parameter plastic potential functions with assumptions of anisotropy have been introduced in Sun and Chen (1991) and Xie and Adams (1995) for composite materials, where the parameter is determined by least squares fitting of unit cell characteristic responses. Bao et al. (1991) have used the same hardening exponent for the composite as for the matrix material. A widely used continuum constitutive model for porous materials is that of Gurson (1977), which has been modified by Tvergaard (1982) with unit cell analysis to incorporate the effects of void growth and coalescence. Besides, the limitations in representing actual microstructural heterogeneities, a number of these constitutive models do not adequately accommodate variations in constitutive parameters with evolving deformation and do not account for post-yield anisotropy. Terada and Kikuchi (1995) have tried to overcome this by using the asymptotic homogenization to develop an extensive numerical response database in the strain space. Instantaneous overall composite properties are determined from discrete values of homogenized stress–strain values at points of this database. This approach, however, leads to huge database to cover all possible deformation paths and requires solving an inordinately large number of RVE boundary value problems. Fish et al. (1997) have used the idea of transformation strain fields, introduced by Dvorak and Benveniste

(1992), to develop a two-point averaging scheme based on the mathematical homogenization theory with piecewise constant transformation fields. However, approximating the eigenstrains with low order polynomial functions may not be able to fully account for large gradients in stresses and strains between phases.

Motivated by two considerations, a piecewise continuous elastic–plastic constitutive model with an anisotropic yield function is developed in this paper. The first is an accuracy consideration, in that it should account for the microstructural morphology, e.g. spatial distributions, shapes, sizes and properties of the individual phases, phase interactions, as well as the evolving stress and strain fields. This can be achieved if the model is developed from detailed finite element analyses of the RVE (e.g. VCFEM analysis), subjected to a wide variety of loading conditions. The second is an efficiency consideration, since the creation of a prohibitively large numerical database with a very large number of numerical experiments is of no consequence. The efficient development of a constitutive model, accounting for underlying evolution of state variables, is accomplished by generating piecewise continuous model parameters from data in a discretized strain space (Fig. 4). Numerical data points in the strain space are systematically created through a sequence of computational RVE analyses subject to an ordered set of macroscopic strains and strain paths. The strain space in Fig. 4 is discretized into cubic elements, each containing 32 nodes or data points. From the computational RVE analysis, constitutive parameters like yield function coefficients and plastic work are generated for each nodal point. The constitutive relation at any point in the strain space are then obtained by interpolating nodal values using conventional shape functions. Elastic–plastic models developed in the ensuing sections are for plane strain assumptions.

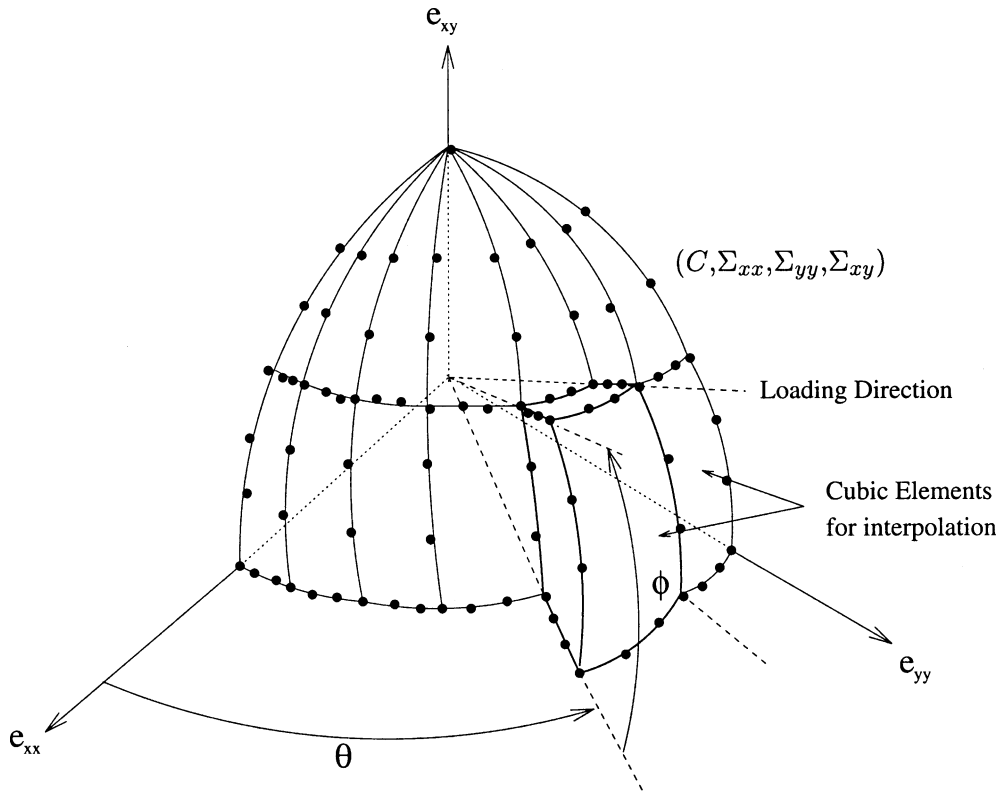

Fig. 4. A $e_{xx} - e_{yy} - e_{xy}$ strain sub-space, discretized into cubic elements for interpolating constitutive model parameters. The nodal values of stresses and plastic work are numerically generated.

5.1.1. Linear elasticity

Orthotropic homogenized elastic material properties are obtained by asymptotic homogenization in conjunction with the VCFE analysis of the composite and porous microstructures from Eq. (19) as explained in Ghosh et al. (1995). With plane strain assumptions, three separate VCFE analyses are conducted, each corresponding to an independent component of the macroscopic strain $\{e_{xx}, e_{yy}, e_{xy}\}$. The orthotropic elasticity tensor is stored for macroscopic analysis.

5.2. Elasto-plasticity with anisotropic yield function

The inclusion phase in composites are assumed to be linear elastic, while the matrix phase is assumed elastic–plastic for both composite and porous materials. In plane strain modeling, an assumption that the total plastic strain in the out of plane or 'third' direction is zero, is made. The yield function can then be described in terms of the macroscopic in-plane stress components (Σ_{xx}, Σ_{yy} and Σ_{xy}). The yield function for porous and composite are written using Hill's 1948 anisotropic yield function (Hill, 1965; Xie and Adams, 1995) in conjunction with the hydrostatic stress dependent models of the Tvergaard–Gurson (Gurson, 1977; Tvergaard, 1982) as

$$\Phi = \frac{C(\Sigma_{xx} - \Sigma_{yy})^2 + 3\,\Sigma_{xy}^2}{Y_f^2(W_\mathrm{p})} + H\cosh\left(\frac{\sqrt{3}}{2}\frac{(\Sigma_{xx} + \Sigma_{yy})}{Y_f(W_\mathrm{p})}\right) - 1 = 0, \tag{26}$$

where e_{xx}, e_{yy}, e_{xy} are the macroscopic in-plane strains, $C(e_{xx}, e_{yy}, e_{xy}, W_\mathrm{p})$ is a strain dependent yield surface parameter and $Y_f(W_\mathrm{p})$ is the flow stress in shear. For the composite materials the dependence of pressure on yielding is deemed negligible and the hydrostatic stress coefficient H is ignored. Coefficients $C(e_{xx}, e_{yy}, e_{xy}, W_\mathrm{p})$, $Y_f(W_\mathrm{p})$ and H are determined from computational experiments detailed next. The increment of plastic strain is obtained from the yield function Φ by using the associated flow rule for hardening materials, i.e. $\dot{e}_{ij}^p = \dot{\lambda}(\partial\Phi/\partial\Sigma_{ij})$.

5.2.1. Coefficient evaluation

5.2.1.1. H and $Y_f(W_\mathrm{p})$: Computational exercises indicate that the variation of H with increasing hydrostatic loading is not significant. It is therefore, assumed to be a constant for all load histories. This assumption is consistent with the Tverggard–Gurson models, where H is determined in terms of the initial void volume fraction. The constitutive parameters H and $Y_f(W_\mathrm{p})$ are evaluated in a coupled manner by solving the microstructural RVE boundary value problems with two distinct loading conditions viz. (i) biaxial tension loading ($\Sigma_{xx} = \Sigma_{yy} = \Sigma_\mathrm{hyd}$, $\Sigma_{xy} = 0$) and (ii) pure shear loading ($\Sigma_{xy} = \Sigma_\mathrm{sh}$, $\Sigma_{xx} = \Sigma_{yy} = 0$). For load condition (i), Eq. (26) becomes

$$\Phi(\Sigma_\mathrm{hyd}, \Sigma_\mathrm{hyd}, 0, W_\mathrm{p}) = H\cosh\left(\sqrt{3}\frac{\Sigma_\mathrm{hyd}}{Y_f(W_\mathrm{p})}\right) - 1 = 0, \tag{27}$$

and for load condition (ii), it becomes

$$\Phi(0, 0, \Sigma_\mathrm{sh}, W_\mathrm{p}) = \frac{3\Sigma_\mathrm{sh}^2}{Y_f^2(W_\mathrm{p})} + H - 1 = 0 \quad \text{or} \quad Y_f(W_\mathrm{p}) = \sqrt{\frac{3\Sigma_\mathrm{sh}^2}{1-H}}. \tag{28}$$

The values of H and $Y_f(W_\mathrm{p})$ are determined iteratively from Eq. (28) and further validated against Eq. (27). The steps are as follows:

1. Solve a macro–micro boundary value problem with RVE homogenization, with incremental pure shear loading. Obtain macroscopic plastic work by averaging the the microstructural plastic work ($\dot{W}_\mathrm{p} = \frac{1}{V_\mathrm{RVE}}\int_\Omega \sigma_{ij}\dot{\epsilon}_{ij}^p \,\mathrm{d}\Omega$) and plot the macroscopic shear stress as a function of plastic work W_p.

2. Assume a starting value for H (e.g. $3\bigstar f_0$ as in Gurson (1977) and Tvergaard (1982) and evaluate $Y_f(W_p)$ from Eq. (28).
3. Solve a pure macroscopic boundary value problem with incremental biaxial loading, using the homogenized elastic–plastic constitutive relation and associated flow rule with yield function (26).
4. Plot the $e_{xx} - \Sigma_{hyd}$ and $e_{yy} - \Sigma_{hyd}$ curves for the entire history of biaxial loading.
5. Solve a macro–micro boundary value problem with RVE homogenization with the same incremental biaxial loading as in the previous step. Plot the $\Sigma_{hyd} - e_{xx}$ and $\Sigma_{hyd} - e_{yy}$ curves for the entire history of loading.
6. Compare the results of steps 4 and 5. If the two curves from both methods are within a preset tolerance everywhere, then the process is terminated and value of H in step 2 is accepted. Otherwise, the entire sequence is repeated with a different value of H.

5.2.1.2. $\underline{C}(e_ij, W_p)$*:* The coefficient C in Eq. (26) is found to vary considerably with the evolution of plastic deformation and examples of its variation with straining and plastic work are shown in Fig. 5. While it is assumed to be a function of the total strain and plastic work, its dependence on load history is assumed to be negligible. In the discretized strain space of Fig. 4, the value of a piecewise continuous C at any point may then be obtained by interpolation from nodal values according to

$$C(e_{xx}, e_{yy}, e_{xy}, W_p) = \sum_{\alpha=1}^{32} C_\alpha(W_p) N_\alpha(e_{xx}, e_{yy}, e_{xy}), \tag{29}$$

where C_α are the nodal values and N_α are shape functions for a 32-noded brick element.

Generation of discretized strain space and nodal parameters: The nodal values of macroscopic stresses $(\Sigma_{xx}, \Sigma_{yy}, \Sigma_{xy})$ and the corresponding plastic work W_p are first evaluated at each nodal point in a subspace of the $e_{xx} - e_{yy} - e_{xy}$ space by solving incremental macro-microscopic boundary value problems with VCFEM

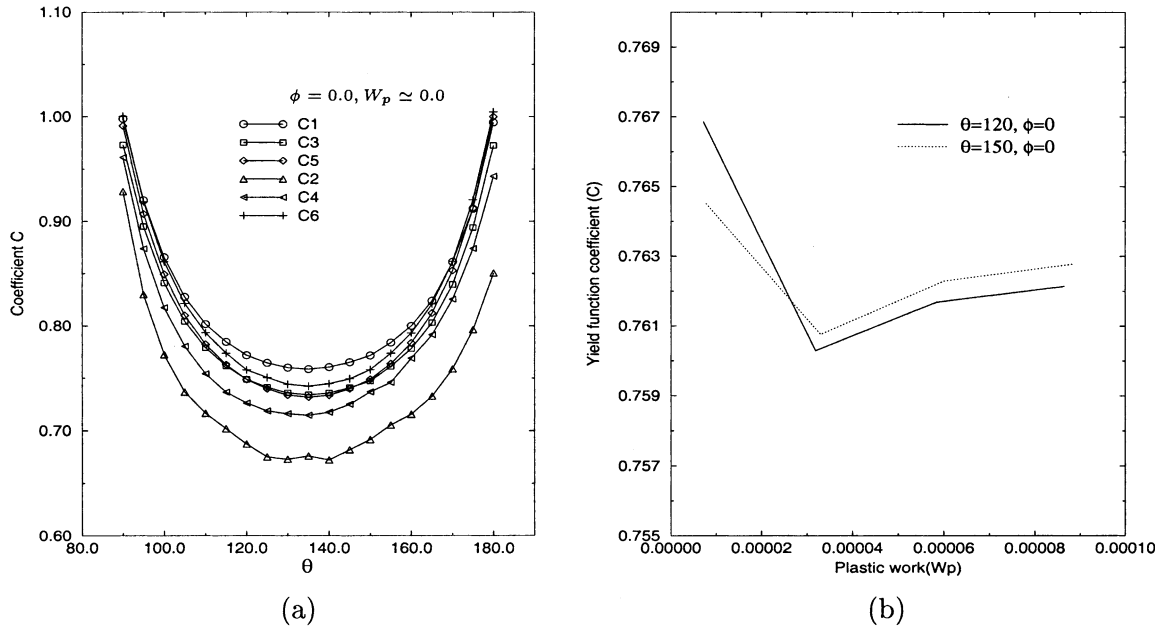

Fig. 5. Variation of the yield function coefficient $C(e_{xx}, e_{yy}, e_{xy}, W_p)$, (a) as a function of θ or normal strains for different microstructures, (b) as a function of plastic work W_p.

and asymptotic homogenization. In this process, macroscopic strain increments are applied to the RVE subjected to periodic boundary conditions (see e.g. Ghosh et al. (1996, 1997)). Strain increments are applied along a radial line in the strain space, such that a constant ratio between strain components is maintained, i.e. $\Delta e_{xx} : \Delta e_{yy} : \Delta e_{xy} = 1 : \tan\theta : (1 + \tan^2\theta)\tan\phi$, where θ and ϕ are the angular coordinates in the strain space of Fig. 4. The flow stress $Y_f(W_p)$ at each node in Fig. 4 can be obtained from the shear stress–plastic work plot and Eq. (28). From the values of macroscopic variables $(\Sigma_{xx}, \Sigma_{yy}, \Sigma_{xy}, Y_f(W_p))$ at a node corresponding to the end of an increment, the coefficient $C(e_{xx}, e_{yy}, e_{xy}, W_p)$ is calculated using Eq. (26).

From the symmetry conditions, only a quarter of the $e_{xx} - e_{yy} - e_{xy}$ strain space is considered for loading such that $0^\circ \leqslant \theta \leqslant 180^\circ$ in the $e_{xx} - e_{yy}$ plane and $0^\circ \leqslant \phi \leqslant 90^\circ$ outside of this plane. This is indicated in Fig. 4. This chosen subspace of the strain space is divided into 16 cubic brick element with 32 nodal points each. The location of elements in the strain space are selected to optimally account for the variations in C. These variations in C with the coordinate angle θ (location in the $e_{xx} - e_{yy}$ plane) and the plastic work W_p for the different microstructures are plotted in Fig. 5. The parabolic form of C in Fig. 5(a) is consistent with the quadratic term $(\Sigma_{xx} - \Sigma_{yy})^2$ in the yield function. The minimum values occur near $\theta = 135^\circ$ corresponding to a pure deviatoric state. The coefficient subsequently increases to account for the increase in plastic work in the yield function Φ. In Fig. 5(b), the coefficient C as a function of the plastic work, which corresponds to the radial direction in the strain space, is plotted. The value of C stabilizes beyond a value of the plastic work, which is used as the outer boundary of the strain space envelope in Fig. 4.

5.3. Numerical implementation of the constitutive model

The elastic–plastic constitutive model for composite and porous materials is derived from the anisotropic yield function (26) with associated flow rule and isotropic hardening. In an incremental form, the stress increments $\Delta\Sigma_{ij}$ are related to elastic increments of strains $(\Delta e_{kl} - \Delta e^p_{kl})$ admitting additive decomposition, as

$$\Delta\Sigma_{ij} = E^{\mathrm{H}}_{ijkl}(\Delta e_{kl} - \Delta e^p_{kl}), \tag{30}$$

where E^{H}_{ijkl} is the homogenized elasticity tensor. Using associated flow rule, components of the plastic strain increment are obtained as

$$\Delta e^p_{ij} = \Delta\lambda \frac{\partial\Phi}{\partial\Sigma_{ij}}. \tag{31}$$

Elimination of the flow parameter $\Delta\lambda$ from the above equations results in two equations,

$$\Delta e^p_{xx}\left(\frac{\partial\Phi}{\partial\Sigma_{yy}}\right) - \Delta e^p_{yy}\left(\frac{\partial\Phi}{\partial\Sigma_{xx}}\right) = 0, \qquad \Delta e^p_{xx}\left(\frac{\partial\Phi}{\partial\Sigma_{xy}}\right) - \Delta e^p_{xy}\left(\frac{\partial\Phi}{\partial\Sigma_{xx}}\right) = 0. \tag{32}$$

These equations are solved using the backward Euler integration method, with gradients evaluated at the end of the increment. With known increments of strain, the resulting set of Eq. (32) together with the yield function (26) are solved iteratively by using the Newton–Raphson method. The stress increments are obtained by the following steps:

1. Initialize values of $\Delta\Sigma_{xx}$, $\Delta\Sigma_{yy}$ and $\Delta\Sigma_{xy}$.
2. Calculate the gradient $\left(\partial\Phi/\partial\Sigma_{ij}\right)$ of the yield function and solve for the increments of plastic strain Δe^p_{xx}, Δe^p_{yy} and Δe^p_{xy} from Eqs. (30) and (32). Update the stresses and plastic work using the relation $\Delta W_p = \Sigma_{xx}\Delta e^p_{xx} + \Sigma_{yy}\Delta e^p_{yy} + \Sigma_{xy}\Delta e^p_{xy}$.
3. If $\Phi \leqslant \mathrm{tol}_1$ and correction to plastic strain increment $\delta e^p_{ij} \leqslant \mathrm{tol}_2$, where tol_1 and tol_2 are prescribed tolerances, then stop. Otherwise go to step 2.

The parameter C is then obtained from the interpolation Eq. (29).

5.4. Numerical examples with the continuum constitutive model

The elastic–plastic constitutive model is validated by comparing the results of macroscopic numerical simulations with those generated by macro–micro scale analysis using asymptotic homogenization. Examples are conducted for both composite and porous materials with different microstructure morphologies, viz. different shapes, sizes and spatial distributions of the heterogeneities.

5.4.1. Analysis of composite microstructures

Six microstructural RVE's of 20% V_f Alumina–aluminum composite with Alumina fiber in aluminum matrix, as shown in Fig. 6, are analyzed. The RVE's are classified as

(a): Square edge pattern with a circular inclusion (C1),
(b): Square edge pattern with an elliptical inclusion (aspect ratio $a/b = 3$) (C2),
(c): Random pattern with 25 identical circular inclusions (C3),
(d): Horizontally aligned random pattern with 25 identical elliptical inclusions (C4),
(e): Randomly oriented random pattern with 25 identical elliptical inclusions (C5),
(f): Random pattern with 17 random shape and size inclusions (C6),

The material properties for the elastic alumina fiber are Young's Modulus $(E_c) = 344.5$ GPa, Poisson ratio $(v_c) = 0.26$; and for the elastic–plastic aluminum matrix are Young's Modulus $(E_m) = 68.3$ GPa, Poisson ratio $(v_m) = 0.30$, initial yield stress (Y_0): 55 MPa, and Post Yield hardening law: $\sigma_{\text{eqv}} = Y_0 + 2.08\epsilon^{pl}_{\text{eqv}}$.

The RVE's are subjected to four different types of loading viz.

- L1: Pure shear loading with increments $(\Delta\Sigma_{xx} = \Delta\Sigma_{yy} = 0, \Delta\Sigma_{xy} = \Delta\Sigma)$
- L2: Uniaxial tension loading with increments $(\Delta\Sigma_{xx} = \Delta\Sigma, \Delta\Sigma_{yy} = \Delta\Sigma_{xy} = 0)$
- L3: Biaxial tension loading with increments $(\Delta\Sigma_{xx} = \Delta\Sigma_{yy} = \Delta\Sigma, \Delta\Sigma_{xy} = 0)$
- L4: Biaxial tension–compression loading with increments $(\Delta\Sigma_{xx} = -\Delta\Sigma_{yy} = \Delta\Sigma, \Delta\Sigma_{xy} = 0)$

The stress–strain response of the six composite microstructural RVE's with the four loading conditions are conducted and the results for simple tension (L1) are depicted in Fig. 7. The results by the constitutive model and two-scale asymptotic homogenization approach are generally found to agree very well for the entire range of loading upto fairly high level of straining. The only discrepancy is found with the biaxial tension loading condition (L3), for which the deviation strains are shown in Table 1. However, the deviations occurs at high strains levels, for which the stresses are nearly twice the matrix yield stress. It is important to note that the deviation of continuum model response from the two-scale asymptotic homogenization response can be used as a signal for switching from the former to the latter type of analysis in a multiple scale simulation.

As an example of a structural analysis with the two approaches, a square plate with a square hole is solved with tension loading on two opposite faces. A quarter of the plate with symmetry and loading conditions is shown in Fig. 8(a). A total traction of 55 MPa is applied in 10 equal increments. The material is a 20% V_f Alumina–aluminum composite with the microstructural RVE consisting of 15 identical circular inclusions dispersed randomly in the matrix (Fig. 8(b)). The material properties are the same as in the previous example. Comparison of the results are made through contour plots of the macroscopic stress Σ_{xx} (shown in Fig. 9) and macroscopic plastic work W_{p} (not shown). The figures reveal that at all locations the difference in the two approaches is less than 1%. However, the computational efficiency of the macroscopic analysis with the continuum constitutive model is far superior than the two scale analysis. The scale up in

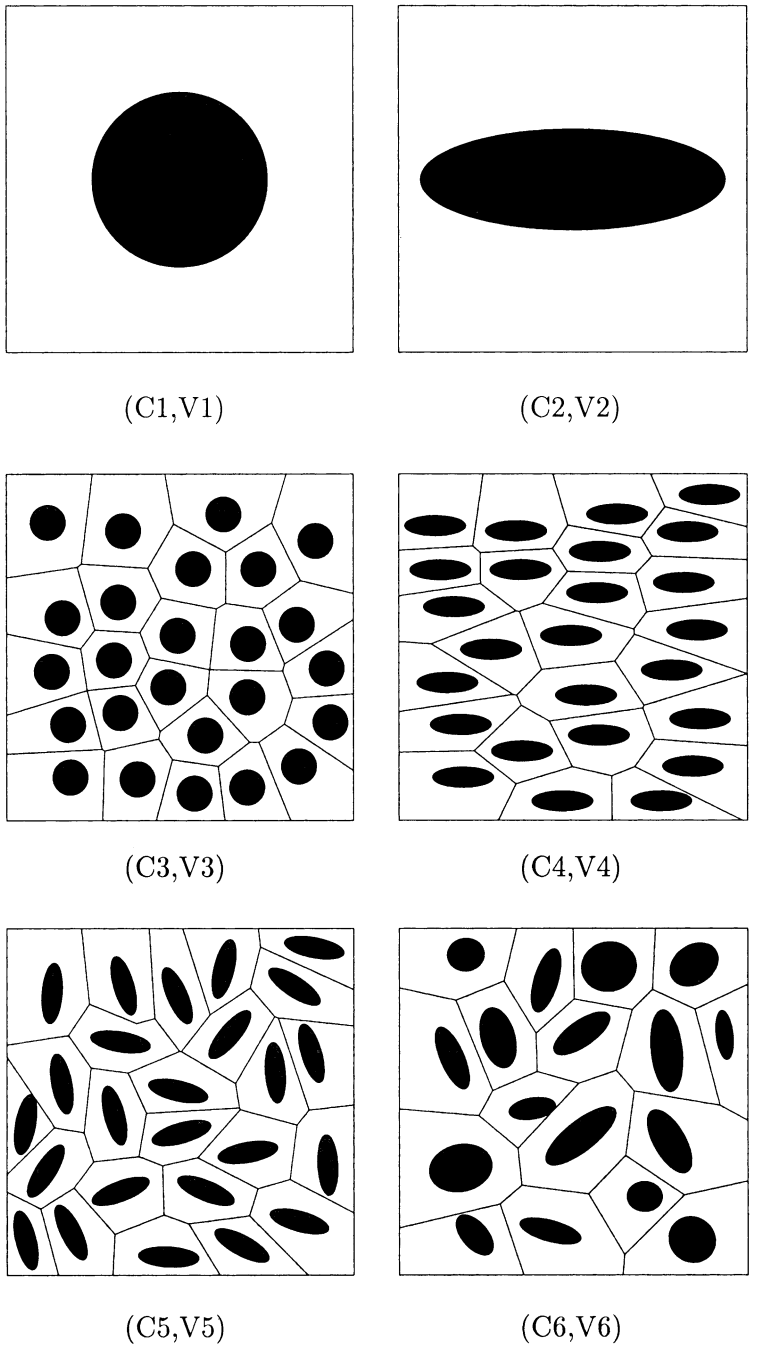

Fig. 6. Microstructures with different shape, size, orientation and spatial distribution, for 20% volume fraction composite (C1,C2,C3,C4,C5,C6) and porous (V1,V2,V3,V4,V5,V6) materials.

efficiency for this problem is approximately 75 000%, and is therefore very desirable when only macroscopic results are of interest.

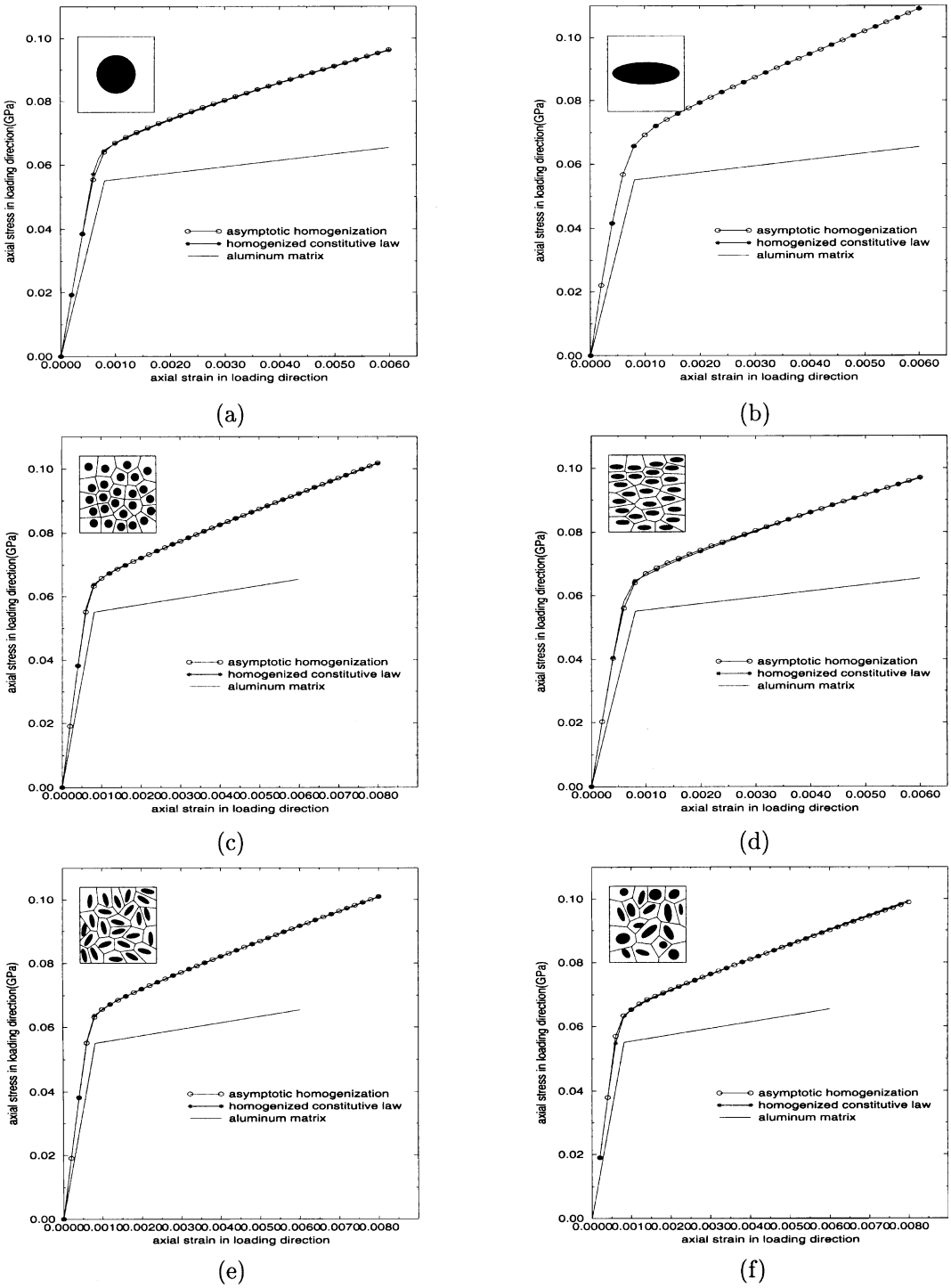

Fig. 7. Comparison of the stress–strain results in the composite for the uniaxial loading test by (i) macroscopic analysis with the homogenized constitutive model and (ii) two-scale analysis with asymptotic homogenization model for (a) C1, (b) C2, (c) C3, (d) C4, (e) C5 and (f) C6 microstructures.

Table 1
Maximum strain (%) in the loading direction at which the constitutive model starts to deviate from the two-scale homogenization computations

Model/loading	C1	C2	C3	C4	C5	C6
L3	0.07%	0.04%	0.08%	0.055%	0.08%	0.075%

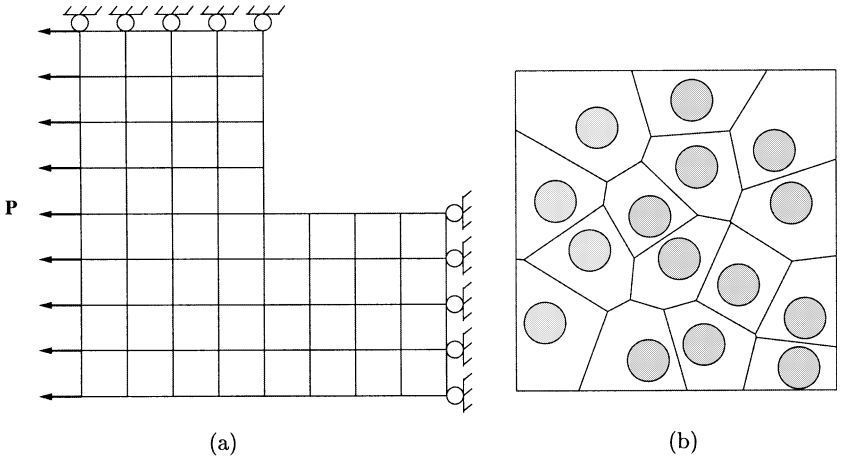

Fig. 8. (a) Finite element model for a quarter of the square composite plate with square hole and (b) the VCFE model of the microstructural composite RVE.

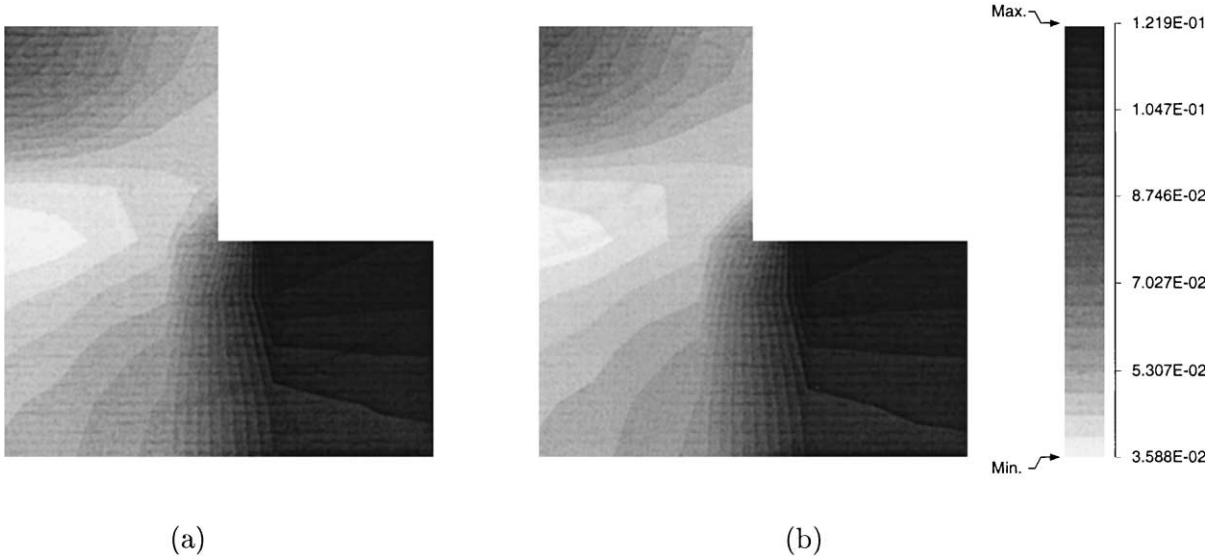

Fig. 9. Comparison of macroscopic stress (Σ_{xx}) contours in composite material with (a) the homogenized constitutive model and (b) two-scale analysis with asymptotic homogenization.

5.4.2. Analysis of porous microstructures

The six microstructural RVEs are analyzed again for porous materials, with voids replacing the inclusions in Fig. 6. The material considered is an aluminum alloy with 20% void volume fraction and the

following elastic–plastic properties: Young's modulus (E_m) = 68.3 GPa, Poisson ratio (v_m) = 0.30, initial yield stress (Y_0) = 55 MPa, and post yield hardening law: $\sigma_{\text{eqv}} = Y_0 + 2.08\epsilon_{\text{eqv}}^{pl}$. The same four load histories (L1,L2,L3,L4) are applied. An important difference between the composite and porous microstructures, is that in the latter plastic strain localization in small regions is a common occurrence depending on the void morphology and the nature of loading. Such non-homogeneous distribution of plastic strains is a major source of discrepancies between responses by the two approaches and act as 'limiters' for the range of application of the continuum model. Microstructures with homogeneous and non-homogeneous distributions of plastic strain are shown in Fig. 10. For the microstructure V1 (square edge pattern with a circular void) the strain distribution is quite uniform in pure shear loading, while for the microstructure V2 (square edge with an elliptical void) there is intense localization with narrow ligaments. Consequently, the continuum model ceases to be effective.

As in the case with composites, the main challenge for the homogenized constitutive model is encountered during simulations with biaxial tension loading, i.e. ($\Delta\Sigma_{xx} = \Delta\Sigma_{yy} = \Delta\Sigma_b$ and $\Delta\Sigma_{xy} = 0$). The first term in the yield function (26) drops out for this loading and the model delivers the same amounts of plastic

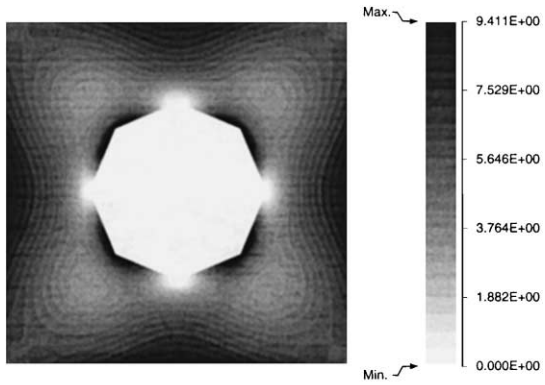

(a)

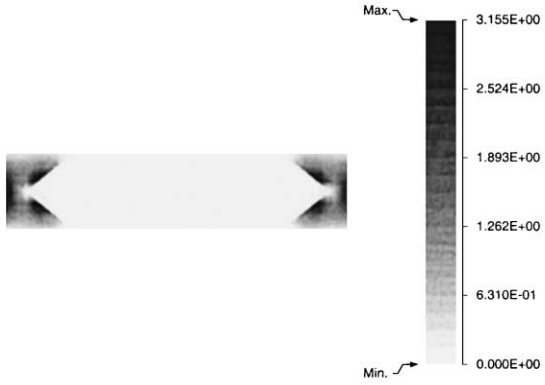

(b)

Fig. 10. Contour plot of the microscopic plastic strain $\bar{\epsilon}^p$ in the voided microstructures under pure shear loading condition, for (a) V1 (b) V2 microstructures.

Table 2
Chart showing the divergence of the constitutive model from the two-scale homogenization computations; y: acceptable for the entire range of loading (1% strain); n: error exceeds a given tolerance at early stages

Model/loading	V1	V2	V3	V4	V5	V6
L1	y	n	y	n	n	n
L2	y	n	y	n	n	n
L3	y	n	y	n	n	n
L4	y	n	y	n	n	n

strains in the x and y directions. Due to the lack of anisotropy in the hydrostatic term in the yield function, the continuum model is effective only for those microstructures that exhibit near isotropic plastic behavior for this loading. Microstructures V2 (square edge with elliptical void) and V4 (horizontally aligned elliptical voids with random spatial distribution) shows very different strain responses for each direction with biaxial loading. Thus, the continuum constitutive model is largely ineffective for these RVE's. The microstructures V5 (randomly oriented identical elliptical voids with random spatial distribution) and V6 (random spatial distribution with random shape and size) also show significant plastically induced directional effects and the constitutive models are therefore restricted to the elastic range. The list of performance and strain ranges of all the microstructures with the different loading are given in Table 2. The microstructures V1 and V3 exhibit relatively isotropic responses and yield satisfactory agreement between responses by the constitutive model and the two-scale asymptotic homogenization. Comparisons of stress–strain responses for biaxially and uniaxially loaded RVE's are made in Fig. 11. These show very good agreement. The RVE's V2 and V4 exhibit intense localization early on in the straining, while the RVE's V5 and V6 exhibit marked anisotropy with biaxial loading. Plastic flow predictions for these RVE's with the continuum model are therefore not reliable.

5.5. Level-0/1 mesh enrichment by h-adaptation

The transition between various levels in this model is augmented by an adaptive mesh refinement involving element subdivision or h-refinement in the level-0 and level-1 regions. This local mesh enrichment is intended to serve two purposes, viz. (a) to identify and reduce discretization error in the computational model and (b) to reduce modeling error by zooming in on regions of evolving localization due to microscopic non-homogeneity. The latter is also effective in bridging the gap between the macro and microscale elements by successive element refinement in critical regions, as shown in Figs. 2(a) and 16. The adaptive h-refinement has been extensively discussed in literature (Zhu and Zienkiewicz, 1988, 1992; Melosh and Marcal, 1977; Demkowicz et al., 1985; Bass and Oden, 1987) and the latest advances in adaptive methods in mechanics have been presented in a compilation by Ladeveze and Oden (1998). Within the category of h-adaptive procedures, two methods, viz. the mesh enrichment or refinement methods (Zhu and Zienkiewicz, 1988; Bass and Oden, 1987) and mesh regeneration methods (Zhu et al., 1993; Paulino et al., 1999) have evolved. While the mesh regeneration methods have been preferred for their relatively higher efficiency, the enrichment method is deemed more suitable for the present work. This is due to the fact that the regeneration method alters element locations with respect to the underlying material RVE and will necessitate cumbersome mapping.

Following procedures outlined in Bass and Oden (1987), the mesh refinement procedure entails subdividing each quadrilateral QUAD4 element into four smaller elements, thus adding four new nodes on the boundary and one in the center. For compatibility with the displacement fields on the boundary of larger adjacent elements, linear constraint relations are imposed on the new boundary nodes of the subdivided

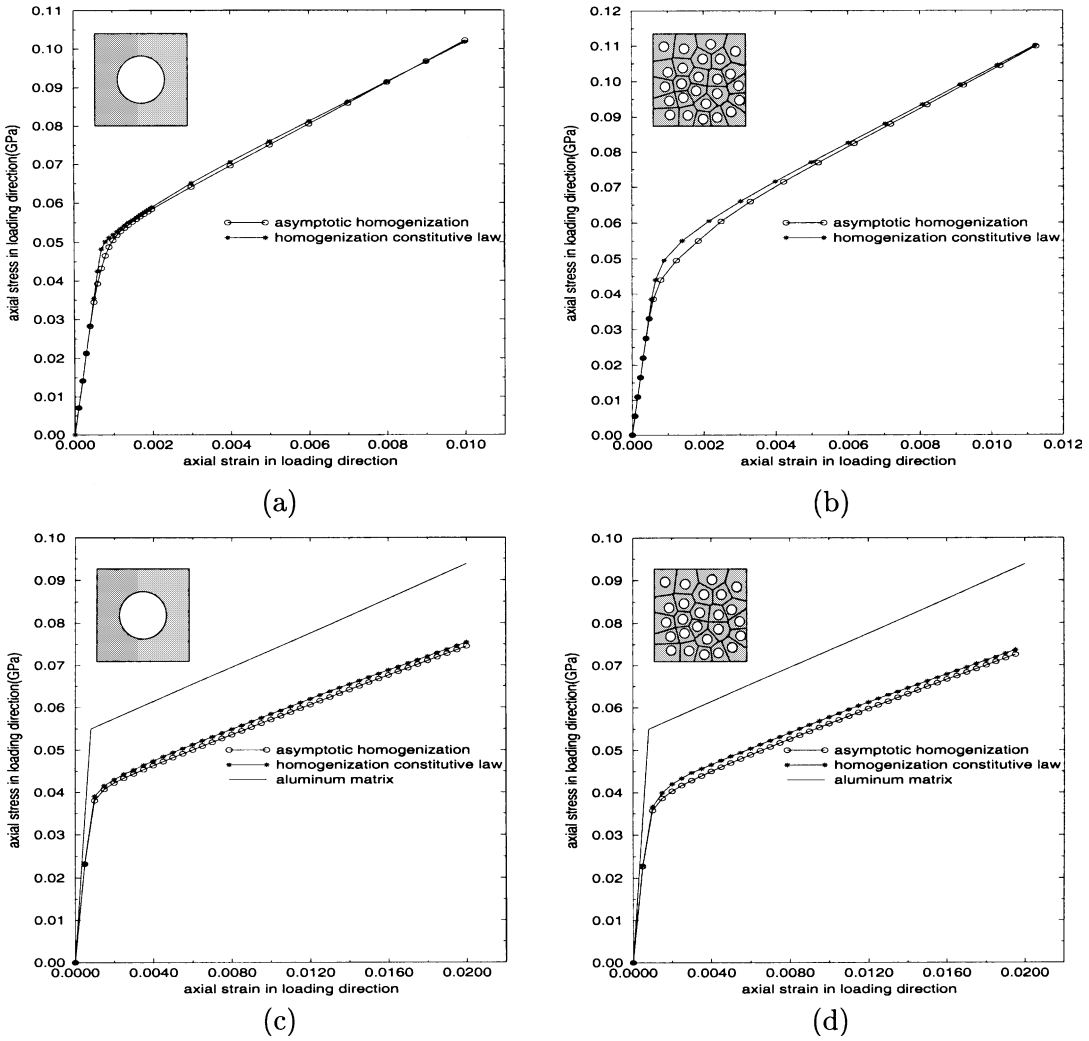

Fig. 11. Comparison of the stress–strain results in the porous material for (a) bi-axial tension for V1 microstructure (b) bi-axial tension for V3 microstructure, (c) uniaxial tension for V1 microstructure and (d) uniaxial tension for V3 microstructure.

element. A static condensation process is then used to eliminate the explicit inclusion of the new nodes in the global stiffness and load vectors (see Bass and Oden (1987) for details). Numerical integration in each QUAD4 element after adaptation is performed by one point reduced integration with hourglass control (Koh and Kikuchi, 1987).

6. Computational subdomain level-1 in the hierarchical model

The level-1 regions ($\Omega_{l1} \subset \Omega_{\mathrm{MAT(p)}}$) in the computational domain are intended as 'swing' or 'transition' regions, where microscopic information in the RVE is used to decide whether microscopic computations

are necessary for these regions. They are identified by locally high gradients of macroscopic variables e.g. stresses, strains strain energy etc. that are indicators of imminent damage evolution or localization in the microstructure. Computations in these regions are still based on assumptions of macroscopic uniformity and periodicity of the RVE. Concurrent with macroscopic simulations, computations are necessary in the the microstructure to monitor the initiation and growth of damage. The RVE response for level-1 elements is explicitly calculated using asymptotic homogenization and VCFEM analysis. The computations in elements belonging to the level-1 domain undergo a sequence of finite element analyses as follows:

(a) Microstructural analysis of the RVE, subjected to the sequence of unit macroscopic strains or increments with periodicity boundary conditions to generate homogenized tangent modulus (E^{H}_{ijkl}).
(b) Macroscopic analysis of the structure using (E^{H}_{ijkl}) of step (a), to evaluate macroscopic variables e.g. stresses and strains due to applied loads.
(c) Microstructural analysis of the RVE at each sampling point (e.g. integration point) of macroscopic elements, with actual macroscopic strains and increments obtained from step (b) and periodicity conditions on the RVE boundary. Microscopic stresses and strains ($\boldsymbol{\sigma}^{\epsilon}, \boldsymbol{\epsilon}^{\epsilon}$) are thus calculated in the RVE's of each element. For linear elastic constituent phases, the microstructural stress recovery process can be achieved by using a linear combination of solutions with unit strains from step (a). However, explicit solution of non-linear equations are required for problems with non-linearity. This is executed in an iterative manner in this paper.

Computational requirements of elements in this level are considerably higher than that for level 0. At each integration point in the macroscopic computational mesh, a complete microstructural analysis of the RVE problem is done several times (at least three times for step (a) and once for step (c) in the present case) within each iteration loop. Thus, the level-1 elements are computationally more expensive compared to level-0 elements. It is therefore important to design robust criteria to avoid redundant element transition from level-0 to level-1. It is also critical that this level be discontinued once the microstructural damage or instability evolved beyond pre-determined threshold values.

7. Computational subdomain level-2 in the hierarchical model

Level-2 regions (Fig. 2(b)) are classified as those with severe microstructural non-uniformities in the form of evolving damage. This results in loss of statistical periodicity of the assumed RVE and these regions may be identified with $\Omega_{\mathrm{MAT(np)}}$ in Eq. (5). In the computational model, the level-2 elements ($\Omega_{l2} \subset \Omega_{\mathrm{MAT(np)}}$) materialize from the microstructure of level-1 elements. It is assumed that prior to this transition, the level-1 elements have been refined to reach sufficiently high spatial resolution. In Ω_{l2}, the macro–micro model of level-1 switches to a completely microscopic model.

The method of generating the level-2 microstructure in each element is illustrated in Fig. 12. An extended microstructure is first created by repeating RVE's in succession, to cover the entire region of the macroscopic level-1 elements in transition to level-2. In Eq. (7), a local non-periodic region is created as

$$Y_k^{\mathrm{MAT(np)}} = \cup_{l=1}^{N^{\infty}} Y_k'^{l}, \tag{33}$$

where $Y_k'^{l}$ corresponds to the RVE's in a periodic domain, adjusted for microscopic evolution. This is then overlayed by the macroscopic elements to accurately encase the level-2 region with clearly delineated boundaries. Each level-2 element now contains a heterogeneous material distribution (Y_k^e) that is defined as the intersection of the non-periodic material region $Y_k^{\mathrm{MAT(np)}}$ and the element domain Ω_{l2}^e

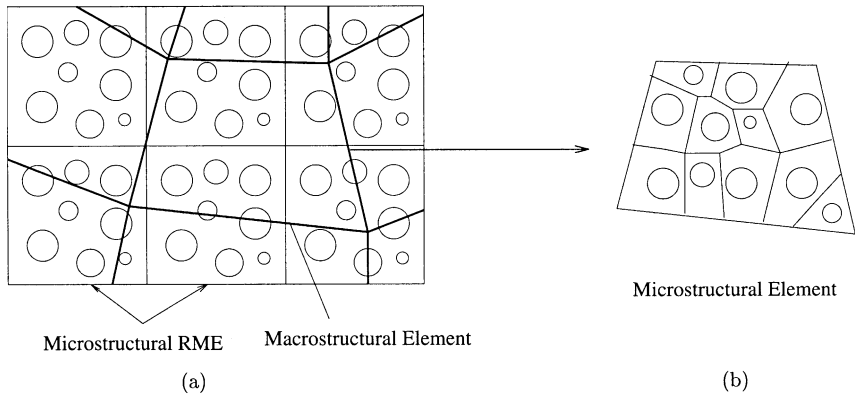

Fig. 12. Creating extended microstructure; (a) a mesh of macroscopic elements with an underlying microstructure of repeated RVEs, (b) the extended microstructure by Voronoi tessellation.

$$Y_k^e = Y_k^{\mathrm{MAT(np)}} \cap \Omega_{l2}^e. \tag{34}$$

This region is subsequently tessellated into a mesh of Voronoi cell elements (Fig. 12(b)). Traction continuity between level-2 microstructural region and neighboring level-0/level-1 elements is incorporated through a layer of transition elements.

7.1. Damage criterion for particle cracking in level-2

The level-2 VCFEM modeling consist of brittle reinforcing particles and a ductile matrix material. For the brittle particulate materials, microstructural damage initiation is assumed to be governed by a maximum principal stress based criterion. In this criterion, a crack is initiated when the maximum principal stress in tension exceeds a critical fracture stress σ^{cr} at a point. In the computational procedure, complete particle splitting is assumed to occur in the form of an elliptical void, normal to the principal direction, as soon as the principal tensile stress reaches σ^{cr}. In the case of particle splitting, the crack tip extends nominally into the matrix. In the incremental computational procedure, more than one point may exceed the critical σ^{cr} value during increment. The location of a single crack is determined by a weighted averaging method as

$$x_{\mathrm{damage}} = \frac{\sum x \frac{\sigma_I^{\mathrm{c}}(x,y)}{\sigma^{\mathrm{cr}}}}{\sum \frac{\sigma_I^{\mathrm{c}}(x,y)}{\sigma^{\mathrm{cr}}}}, \qquad y_{\mathrm{damage}} = \frac{\sum y \frac{\sigma_I^{\mathrm{c}}(x,y)}{\sigma^{\mathrm{cr}}}}{\sum \frac{\sigma_I^{\mathrm{c}}(x,y)}{\sigma^{\mathrm{cr}}}} \quad \forall [\sigma_I^{\mathrm{c}}(x,y) \geqslant \sigma^{\mathrm{cr}}], \tag{35}$$

where $\sigma_I^{\mathrm{c}}(x,y)$ corresponds to all values of maximum tensile principal stress larger than σ^{cr} in the particle. The crack is oriented at right angles to the principal stress directions at $(x_{\mathrm{damage}}, y_{\mathrm{damage}})$ and extends to the interface on both sides.

8. Coupling the levels in the hierarchical FE model

While level-0 elements ($E_{l0} \in \Omega_{l0}$) and level-1 elements ($E_{l1} \in \Omega_{l1}$) are coupled naturally through the familiar assembly process, the interfacing of level-2 ($E_{l2} \in \Omega_{l2}$) elements with either of the first two requires more attention. The mismatch in the number of boundary nodes in these elements necessitate the intro-

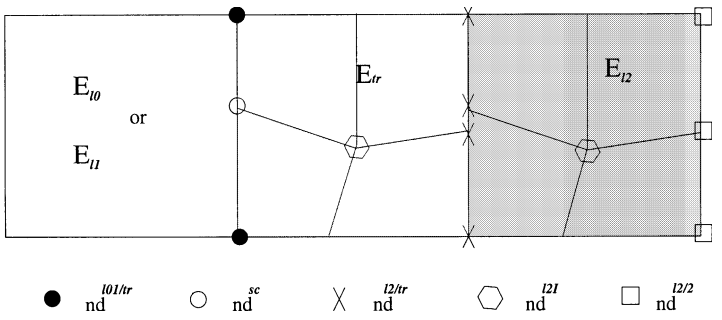

Fig. 13. Interfaces between the level 0/1 E_{l0} and E_{l1} elements, transition E_{tr} elements and the level-2 E_{l2} elements.

duction of transition elements ($E_{\mathrm{tr}} \in \Omega_{l2}$), acting as buffer zones as shown in Fig. 13. Both E_{l2} and E_{tr} elements employ VCFEM for setting up the element stiffness matrices and load vectors. The entire computational domain is thus comprised of

$$\Omega^{\epsilon} = \{\Omega_{l0} \cup \Omega_{l1} \cup \Omega_{l2} : \Omega_{l0} = \cup_{k=1}^{N_{l0}} E_{l0};\ \Omega_{l1} = \cup_{k=1}^{N_{l1}} E_{l1};\ \Omega_{l2} = \cup_{k=1}^{N_{l2}} E_{l2} \cup \cup_{k=1}^{N_{\mathrm{tr}}} E_{\mathrm{tr}}\}$$

for which the nodes are differentiated as (see Fig. 13)

(i) ($\mathbf{nd}^{l2\mathrm{I}}$) or internal level-2 Voronoi cell element nodes that are not on any interface or boundary,
(ii) ($\mathbf{nd}^{l2/2}$) or Voronoi cell element nodes on the E_{l2}–E_{l2} interface,
(iii) ($\mathbf{nd}^{l2/\mathrm{tr}}$) or Voronoi cell element nodes on E_{l2}–E_{tr} interface,
(iv) ($\mathbf{nd}^{l01/\mathrm{tr}}$) or nodes on $E_{l0/1}$–E_{tr} interface that belong to E_{l0} and E_{l1} elements,
(v) ($\mathbf{nd}^{\mathrm{sc}}$) or Voronoi cell element nodes on $E_{l0/1}$–E_{tr} interface that do not belong to E_{l0} and E_{l1} and need to be statically condensed. In an incremental analysis for elasto-plasticity, the principle of virtual work for the computational domain at the end of the nth increment may be written as a scalar valued function G in terms of variables at different levels as

$$\begin{aligned} G^{n+1}(\Delta\mathbf{u}, \delta\mathbf{u}) = & \int_{\Omega_{l0}^{n+1}} \Sigma_{ij}(\mathbf{u}^n + \Delta\mathbf{u}) \frac{\partial \delta u_i}{\partial x_j} \mathrm{d}\Omega - \int_{\Omega_{l0}^{n+1}} f_i \delta u_i \,\mathrm{d}\Omega + \int_{\Omega_{l1}^{n+1}} \Sigma_{ij}(\mathbf{u}^n + \Delta\mathbf{u}) \frac{\partial \delta u_i}{\partial x_j} \mathrm{d}\Omega \\ & - \int_{\Omega_{l1}^{n+1}} f_i \delta u_i \,\mathrm{d}\Omega + \int_{\Omega_{l2}^{n+1}} \sigma_{ij}(\mathbf{u}^n + \Delta\mathbf{u}) \frac{\partial \delta u_i}{\partial x_j} \mathrm{d}\Omega - \int_{\Omega_{l2}^{n+1}} f_i \delta u_i \,\mathrm{d}\Omega - \int_{\Gamma_{l0}^{n+1}} t_i \delta u_i \,\mathrm{d}\Gamma \\ & - \int_{\Gamma_{l1}^{n+1}} t_i \delta u_i \,\mathrm{d}\Gamma - \int_{\Gamma_{l2}^{n+1}} t_i \delta u_i \,\mathrm{d}\Gamma. \end{aligned} \tag{36}$$

In an iterative solution process with the Newton–Raphson method, a consistent linearization by taking the directional derivative of G^{n+1} along incremental displacement vector $\Delta\mathbf{u}$, yields the tangent stiffness matrix. For the ith iteration, the assembled equations have the following structure:

$$\begin{bmatrix} K^{l0/1,l0/1} & K^{l0/1,l2} \\ K^{l2,l0/1} & K^{l2,l2} \end{bmatrix}^i \begin{Bmatrix} \Delta U^{l0/1} \\ \Delta U^{l2\mathrm{B}} \end{Bmatrix}^i = \begin{Bmatrix} \Delta F^{l0/1} \\ \Delta F^{l2} \end{Bmatrix}^i. \tag{37}$$

Here $\Delta U^{l0/1}$ corresponds to displacements at nodes ($\mathbf{nd}^{l0/1}$) that belong to elements E_{l0} and E_{l1} in the computational region $\Omega_{l_0} \cup \Omega_{l_1}$ as shown in Fig. 13. It should be noted that they also include nodes at the interface of elements E_{l0}/E_{l1} and elements E_{tr}. The displacements $\Delta U^{l2\mathrm{B}}$ on the other hand corresponds to nodes ($\mathbf{nd}^{l2/\mathrm{tr}}$) on the interfaces of elements E_{tr} and elements E_{l2} or to nodes ($\mathbf{nd}^{l2/2}$) on the interfaces

between two E_{l2} elements. Contributions to the stiffness matrix $[K]$ and load vector $\{F\}$ for elements in $\Omega_{l_0} \cup \Omega_{l_1}$ may be obtained as

$$(K^{l0/1,l0/1}_{i\alpha j\beta})^i = \int_{\Omega^{n+1}_{l_0} \cup \Omega^{n+1}_{l_1}} \frac{\partial N^G_\alpha}{\partial x_i} \frac{\partial \Sigma_{ij}}{\partial e_{kl}} \frac{\partial N^G_\beta}{\partial x_l} \mathrm{d}\Omega,$$

$$(F^{l0/1}_{i\alpha})^i = \int_{\Omega^{n+1}_{l_0} \cup \Omega^{n+1}_{l_1}} f_i N^G_\alpha \,\mathrm{d}\Omega + \int_{\Gamma^{n+1}_{l_0} \cup \Gamma^{n+1}_{l_1}} t_i N^G_\alpha \,\mathrm{d}\Gamma - \int_{\Omega^{n+1}_{l_0} \cup \Omega^{n+1}_{l_1}} \Sigma_{ij}(\mathbf{u_n} + \Delta \mathbf{u}^i) \frac{\partial N^G_\alpha}{\partial x_j} \mathrm{d}\Omega,$$

α, β correspond to the node numbers and N_α are the shape functions of macroscopic elements. For the elements E_{tr} and E_{l2} belonging to Ω_{l_2}, contributions to the stiffness matrix and load vectors are obtained by VCFEM calculations, together with static condensation. The transition element facilitates continuous variation from microscopic to macroscopic elements without jumps or discontinuities. On the $E_{l0/1}$–E_{tr} interfaces, this is accomplished by constraining displacements at nodes $\mathbf{nd}^{\mathrm{sc}}$ to conform to displacement interpolation of the adjacent E_{l0} or E_{l1} elements. The constraints at the nodes $\mathbf{nd}^{\mathrm{sc}}$ are applied in terms of displacements at $\mathbf{nd}^{l01/\mathrm{tr}}$ as

$$\{\Delta U^{\mathrm{sc}}\} = [Q]\{\Delta U^{l01/\mathrm{tr}}\}, \tag{38}$$

where $[Q]$ is the constraining matrix. For bilinear QUAD4 level-0/1 elements, each row of $[Q]$ consists of the inverse of the distance of the constrained node to the corner nodes. The interfaces with the E_{l2} elements, i.e. the E_{l2}–E_{tr} interfaces are treated in the same way as E_{l2}–E_{l2} interfaces.

The displacements $\Delta U^{l2\mathrm{B}}$ in Eq. (37) correspond to those at the boundary nodes ($\mathbf{nd}^{l2/2}$, $\mathbf{nd}^{l2/\mathrm{tr}}$, $\mathbf{nd}^{l01/\mathrm{tr}}$ and $\mathbf{nd}^{\mathrm{sc}}$) of level-2 elements that contain the microstructural VCFE model. To account for the contribution of the internal nodes ($\mathbf{nd}^{l2\mathrm{I}}$), it is therefore necessary to use static condensation and recovery process for representing the VCFEM displacement solutions at the internal nodes $\Delta U^{l2\mathrm{I}}$ in terms of the displacements at boundary nodes $\Delta U^{l2\mathrm{B}}$, where

$$\{\Delta U^{l2\mathrm{B}}\} = \begin{Bmatrix} \Delta U^{l2/2} \\ \Delta U^{l2/\mathrm{tr}} \\ \Delta U^{l01/\mathrm{tr}} \\ \Delta U^{\mathrm{sc}} \end{Bmatrix} = \begin{bmatrix} I & 0 & 0 & 0 \\ 0 & I & 0 & 0 \\ 0 & 0 & I & 0 \\ 0 & 0 & 0 & Q \end{bmatrix} \begin{Bmatrix} \Delta U^{l2/2} \\ \Delta U^{l2/\mathrm{tr}} \\ \Delta U^{l01/\mathrm{tr}} \end{Bmatrix}, \tag{39}$$

where $[I]$ and $[Q]$ are the identity and constraint matrices respectively. In a VCFEM solution process the stiffness matrix and the load vector may be partitioned accordingly as

$$\begin{bmatrix} K^{l2\mathrm{B},l2\mathrm{B}} & K^{l2\mathrm{B},l2\mathrm{I}} \\ K^{l2\mathrm{I},l2\mathrm{B}} & K^{l2\mathrm{I},l2\mathrm{I}} \end{bmatrix} \begin{Bmatrix} \Delta U^{l2\mathrm{B}} \\ \Delta U^{l2\mathrm{I}} \end{Bmatrix} = \begin{Bmatrix} \Delta F^{l2\mathrm{B}} \\ \Delta F^{l2\mathrm{I}} \end{Bmatrix}. \tag{40}$$

Static condensation of the internal degrees of freedom yields

$$\left[\left[K^{l2\mathrm{B},l2\mathrm{B}}\right] - \left[K^{l2\mathrm{B},l2\mathrm{I}}\right]\left[K^{l2\mathrm{I},l2\mathrm{I}}\right]^{-1}\left[K^{l2\mathrm{I},l2\mathrm{B}}\right]\right]\left\{\Delta U^{l2\mathrm{B}}\right\} = \left\{\Delta F^{l2\mathrm{B}}\right\} - \left[K^{l2\mathrm{B},l2\mathrm{I}}\right]\left[K^{l2\mathrm{I},l2\mathrm{I}}\right]^{-1}\left\{\Delta F^{l2\mathrm{I}}\right\}. \tag{41}$$

These stiffness matrices and load vectors are then used in the assembly process of Eq. (37).

9. Adaptation criteria for various levels

It is evident that appropriate criteria need to be established for transitioning the computational subdomains from one level to another. In addition to level transitions, element refinement by *h*-adaptation is also executed in level-0 and level-1 regions for reducing discretization error, identifying regions of high

solution gradients and zooming in to reduce the scale gap between macroscopic and microscopic elements. The criteria used for element refinement and level transition are delineated below.

Level 0/1 h-adaptation may be executed based on an error measure may be defined as

$$E_e = \|f(\mathbf{u} - \mathbf{u}_h)\|, \tag{42}$$

where $\mathbf{u}$ is the true solution, $\mathbf{u}_h$ is its finite element approximation, f is any appropriate function of deformation e.g. energy, stresses, strains etc., and $\|\cdot\|$ denotes a norm of the function. Work on h-method of mesh refinement (Zhu and Zienkiewicz, 1988; Melosh and Marcal, 1977; Demkowicz et al., 1985) have proposed various forms of f and norms to optimize the computational effort and improve reliability. In this work, elements are subdivided based on an element level parameter defined as

$$(E_e)_{\mathrm{cr}} = qi\frac{\|f(\mathbf{u}_{\mathrm{h}})\|}{\sqrt{NE}}, \tag{43}$$

where $(E_e)_{\mathrm{cr}}$ corresponds to a threshold element parameter, above which the element needs to be refined and qi is a prescribed quality index. $\|f(\mathbf{u}_h)\| = \sum_{e=1}^{NE} \|f(\mathbf{u}_h)\|_e$ is the sum of element norms of any function for the entire computational domain and NE is the number of elements. Such error criteria is conventionally used to equi-distribute errors due to discretization by mesh refinement for relatively well behaved problems. However, for mesh dependent problems with inherent localizations or singularities in the solutions, the above criteria may be used for signaling steep gradients in the solution variables and may be used for increasing the resolution in the region of high local gradients. In this work $\|f(\mathbf{u}_h)\|_e$ is taken to be the maximum difference in plastic work with neighboring elements, i.e.

$$\|f(\mathbf{u}_h)\|_e = \mathrm{Max}\left|\left(\int_\Omega \Sigma_{ij}\bar{\epsilon}^p_{ij}\,\mathrm{d}\Omega\right)^e - \left(\int_\Omega \Sigma_{ij}\bar{\epsilon}^p_{ij}\,\mathrm{d}\Omega\right)^{\mathrm{adjacent}}\right|$$

with a value of $qi = 1.5$.

Level-0 to level-1 transition of E_{l0} elements takes place in accordance with criteria based on macroscopic variables e.g. (Σ, **e**) in the continuum model that are related to critical microscopic variables. Additionally, this transition is activated when the continuum level model in Section 5.1 starts to decrease considerably from the results of two-scale homogenization. Different criteria are used for composite and porous materials.

(A) For composite microstructure with inclusions

$$(\Sigma_I) \geqslant \Sigma^{\mathrm{cr}} = r * \sigma^{\mathrm{cr}} \quad \text{and/or} \quad \frac{(\Sigma_{xx} + \Sigma_{yy})}{2} \geqslant \Sigma^{\mathrm{cr}}_h. \tag{44}$$

Here Σ_I is the maximum principal stress in E_{l0}, Σ^{cr} is a critical stress that is a pre-determined fraction r of the critical fracture stress (σ^{cr}) for microstructural inclusions. The fraction r is selected to be $1/3$ in this study. The second condition is established since the earliest digression from the homogenization results is observed for biaxial loading, and Σ^{cr}_h established from the results of Section 5.4.

(B) For porous microstructure with voids: Strain based criteria are deemed more important in the case of damage in porous materials and hence transition is activated when

$$(\bar{e}^p) \geqslant (\bar{e}^p)^{\mathrm{cr}} = r * (\epsilon^p)^{\mathrm{cr}} \quad \text{and/or} \quad \frac{(e_{xx} + e_{yy})}{2} \geqslant e^{\mathrm{cr}}_H \tag{45}$$

where $\bar{e}^p\left(= \sqrt{\frac{1}{2}e^p_{ij}e^p_{ij}}\right)$ is the macroscopic effective plastic strain in E_{l0} and $(\bar{e}^p)^{\mathrm{cr}}$ is a pre-determined fraction r of a suitably assessed high microstructural plastic strain $(\epsilon^p)^{\mathrm{cr}}$. Again e^{cr}_H is established from the limiting values of biaxial strain in Section 5.4.

Level-1 to level-2 transition of E_{l1} elements occur when a sufficiently high spatial resolution is attained by *h*-refinement and when the RVE is deemed to be on the verge of significant damage evolution. The adaptive criteria, which monitor the transition from elements E_{l1} to E_{l2} are prescribed in terms of topological evolution of microscopic damage as

(A) For composite microstructure with inclusions,

$$R_{\text{damage}} = \frac{NDP}{NP} \geqslant R_{\text{cr}}. \tag{46}$$

(B) For porous microstructure with voids,

$$R_{\text{damage}} = \frac{ADR}{AR} \geqslant R_{\text{cr}}, \tag{47}$$

where R_{damage} is the ratio of the number of damaged inclusions (NPD) to the total number of inclusions (NP) for composites. For porous microstructures, it is the ratio of the damaged area corresponding to regions which have high plastic strains to the total RVE area. R_{cr} is a prescribed critical ratio and varies from problem to problem.

10. Numerical examples with the adaptive multi-level model

Numerical examples are solved to understand the effect of structural geometry and microstructural morphologies on the macroscopic and microscopic responses. In all examples, the inclusions are assumed to be linear elastic which can crack by the principal stress criterion and the matrix is elastic–plastic. In the first example, a RVE consisting of a single circular inclusion is modeled by level-1 and level-2 elements under applied uniaxial tension loading. In the first case, the E_{l1} macroscopic element is coupled with the microscopically periodic RVE by asymptotic homogenization, while in the second case, the tension load is directly applied on one edge of the Voronoi cell element E_{l2} model of the RVE. The loading is continued beyond the level of inclusion cracking. This is represented by the loss of stress carrying capacity in the averaged stress–stain plot of Fig. 14(a). Though the response is similar in the initial elastic phase, it diverges with the onset of plastic flow. The damage occurs earlier in the level-1 element due to the additional constraint of periodicity. The contour plots of inclusion maximum principal stress, normalized by the critical stress σ^{cr}, are compared at a macroscopic strain 2.1% in Fig. 14. This is just before cracking by the level-1 model. A considerably lower stress level is seen for the level-2 model. Such over-estimation of stresses with periodicity boundary condition near free boundaries necessitate the use of the proposed multi-level models.

10.1. Effects of inhomogeneity size (scale effect)

Neglecting scale effects, that reflect the actual size of microstructural constituents, is a characteristic of homogenization with assumptions of statistical periodicity of a vanishingly small RVE. While elements E_{l0} and E_{l1} conform to this restriction, the level-2 elements E_{l2} in this work depict the actual size of the microstructure through the multi-level coupling and hence scale effects prevail.

In this example the effect of particle or void size on the evolution of damage is investigated. The two different microstructural RVE's considered in Fig. 15(b) (i) and (ii) have identical distribution (square edge) and same particle or void area fraction of $V_f = 20\%$. But the RVE sizes are different in that, the size of the smaller RVE (i) is 0.5 mm $\times$ 0.5 mm, while that of the larger RVE (ii) is 1 mm $\times$ 0.5 mm. The macroscopic

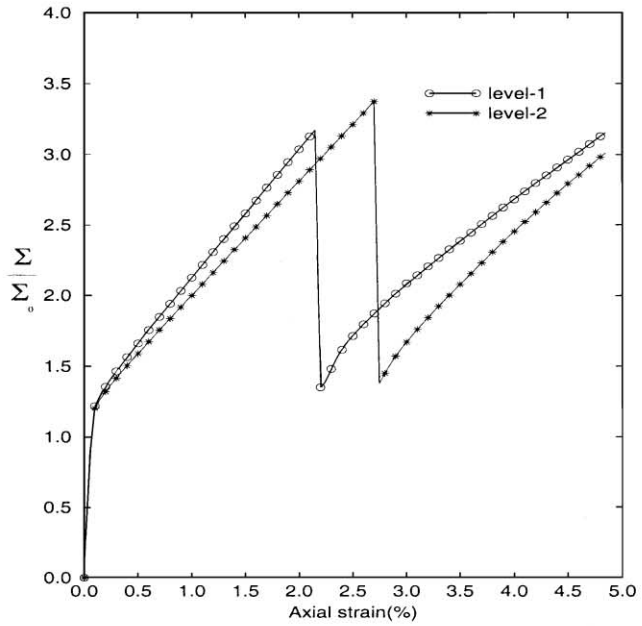

(a)

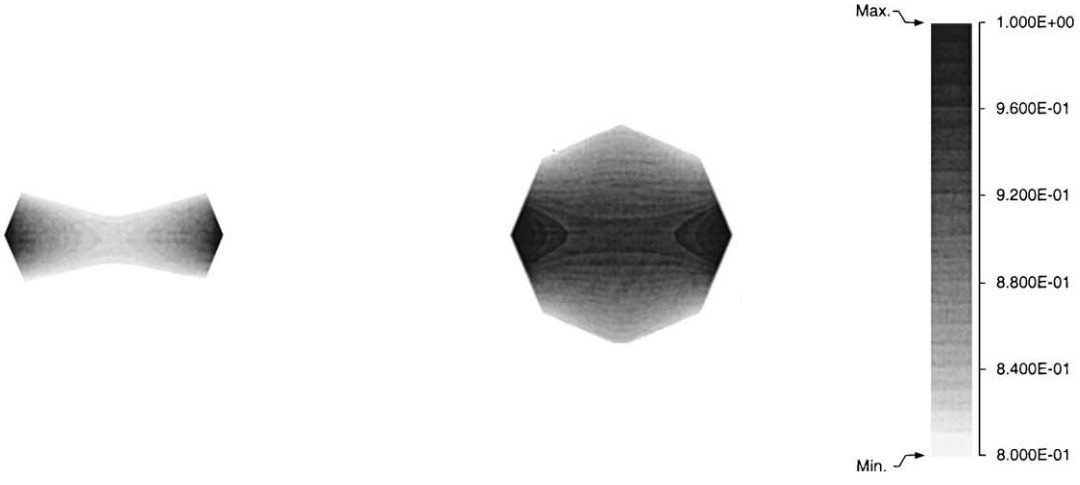

(b) (c)

Fig. 14. (a) Macroscopic axial stress–strain plots for a single RVE in tension modeled by level-1 and level-2 elements; Maximum principal stress distribution in the inclusion by (b) level-2 element and (c) level-1 element.

structure is a square plate with a square hole, for which the initial level-0 mesh with dimensions is shown in Fig. 15(a). Only a quarter of the plate is modeled from symmetry considerations. The smallest size of macroscopic element allowed in this analysis by *h*-adaptation is set to 1 mm. Thus, the E_{l2} elements contain

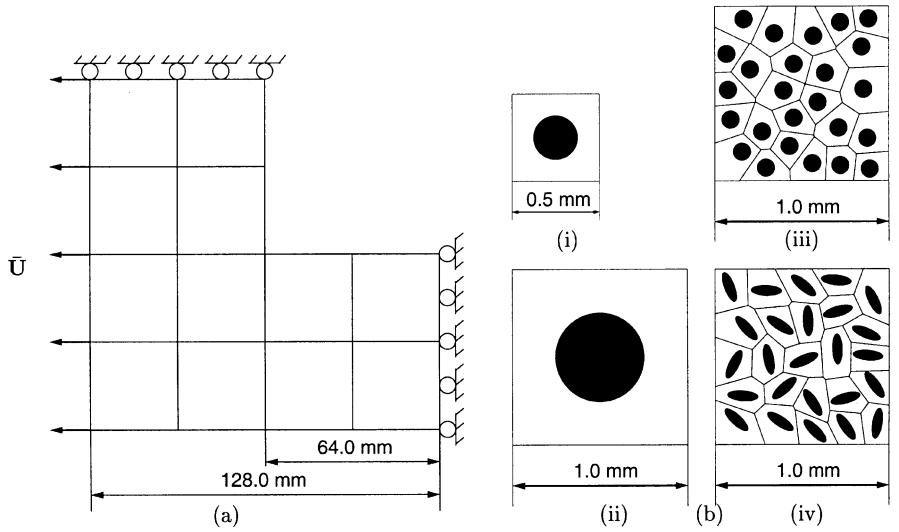

Fig. 15. (a) A quarter of the level-0 starting macroscopic model of a square plate with a square hole, (b) four different microstructural RVE's for the plate model.

only one element in the VCFEM model for the larger RVE (ii) but four elements in the VCFEM model for the smaller RVE (i). The material properties for both composite and porous materials are as follows:

Aluminum matrix (elastic–plastic): Young's modulus $(E_m) = 68.3$ GPa, Poisson ratio $(\nu_m) = 0.30$, initial yield stress $(Y_0) = 55$ MPa, and post yield hardening law: $\sigma_{\text{eqv}} = Y_0 + 2.08\epsilon^{pl}_{\text{eqv}}$.
Alumina particle (elastic): Young's modulus $(E_c) = 344.5$ GPa, Poisson ratio $(\nu_c) = 0.26$, critical particle cracking stress $(\sigma^{\text{cr}}) = 0.3$ GPa.

The load is applied in 20 equal increments upto a total displacement of 1 mm as shown in Fig. 15(a).

For the composite microstructures, Fig. 16 depicts the evolved macroscopic and level-2 computational domains at the end of loading stages. The level-0, level-1, level-2 elements are shown in white, grey and black, respectively, for the adapted macroscopic mesh in Fig. 16(a) and (b). The evolution of the levels and mesh with *h*-adaptation is provided in Table 3. The effect of the microstructure size becomes more pronounced with increasing deformation. A larger level-2 domain (29 macroscopic elements) with a smaller level-0 domain is evidenced for the smaller RVE (i). The effect of RVE size on the pattern of particle cracking is very significant. The level-2 region shows 24 cracked particles for the RVE (i) as opposed to six cracked particles for the RVE (ii). The path of evolution of cracked particles is quite different for the two models. For the RVE (ii), the aggregate microscopic cracks is found to propagate perpendicular to the macroscopic loading direction and all the microcracks have the same orientation as the chain or macrocrack. For the smaller particles in RVE (i), the chain of microcracks or the macrocrack is observed to move at 45° to the loading direction with individual microcracks predominantly at 90° to the loading direction.

The contour plots of macroscopic and microscopic plastic strain distribution at the final loading stage are shown in Figs. 17 and 18 for the two microstructures. The macroscopic strain distribution for both models shows higher strain concentration at the corner of square hole with increased loading. While the macroscopic strains are not very different for the two RVE's, significantly larger local plastic strains are seen in the level-2 microstructure of RVE (i). A better representation of this difference is seen in the graphs of Figs. 19 and 20. The macroscopic (averaged) stress Σ_{xx} history at the critical corner in Fig. 19 does not indicate significant difference and hence exhibits little scale effect. The stress drops in this figure correspond

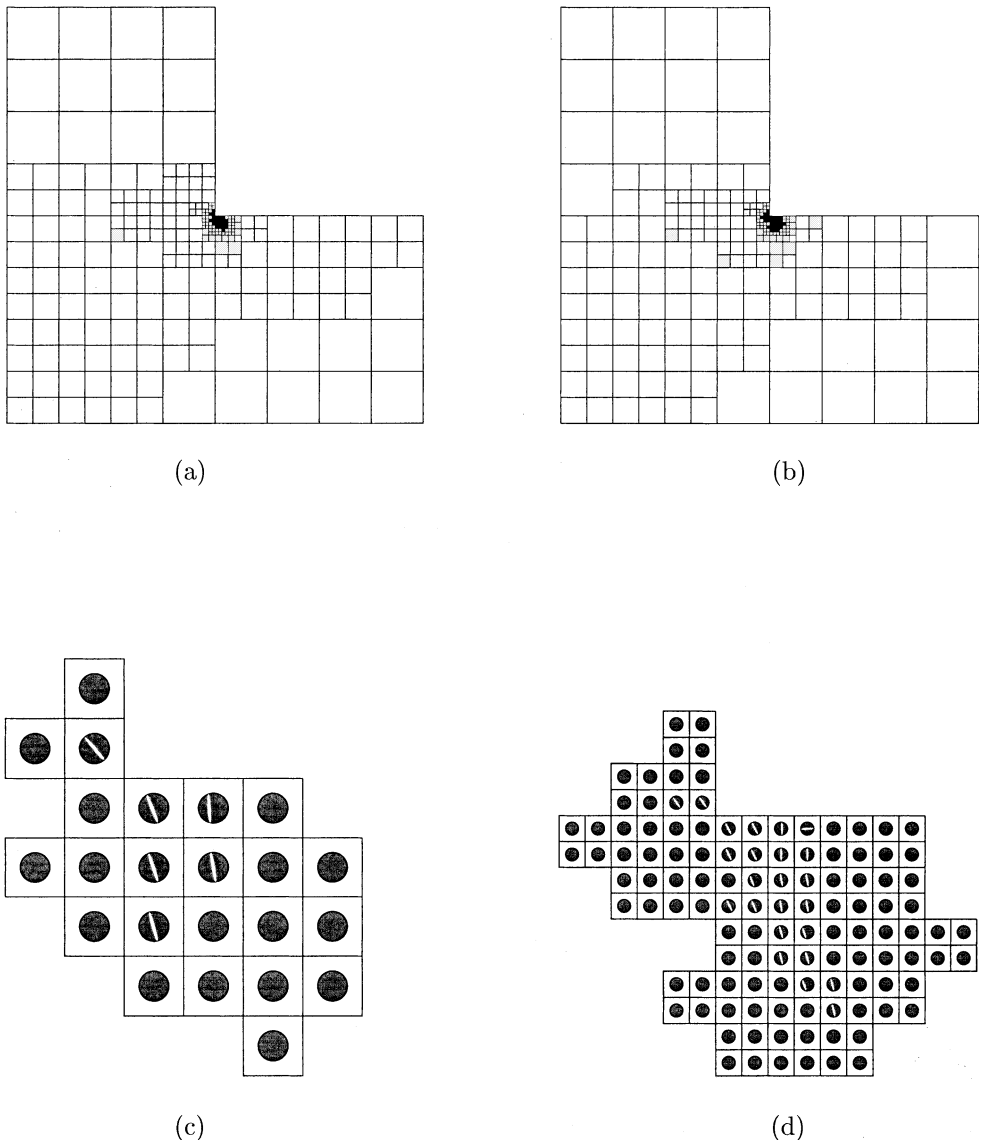

Fig. 16. Macroscopic three level evolved mesh for the composite material at the end of the loading cycle for (a) the larger RVE (ii) and (b) smaller RVE (i); the corresponding level-2 region with the (c) the larger RVE (ii) and (d) smaller RVE (i). Level-0 is with white elements, level-1 is with grey elements and level-2 is with black elements.

Table 3
Evolution of elements at various levels with straining for composite microstructure

% of Total displacement	Level-0 elements		Level-1 elements		Level-2 elements		Total	
	RVE (i)	RVE (ii)	RVE (i)	RVE (ii)	RVE (i)	RVE (ii)	RVE (i)	RVE (ii)
50	199	204	1	0	4	4	204	208
75	181	201	22	17	10	7	213	225
90	167	188	34	34	15	18	219	240
100	162	178	42	43	29	25	234	246

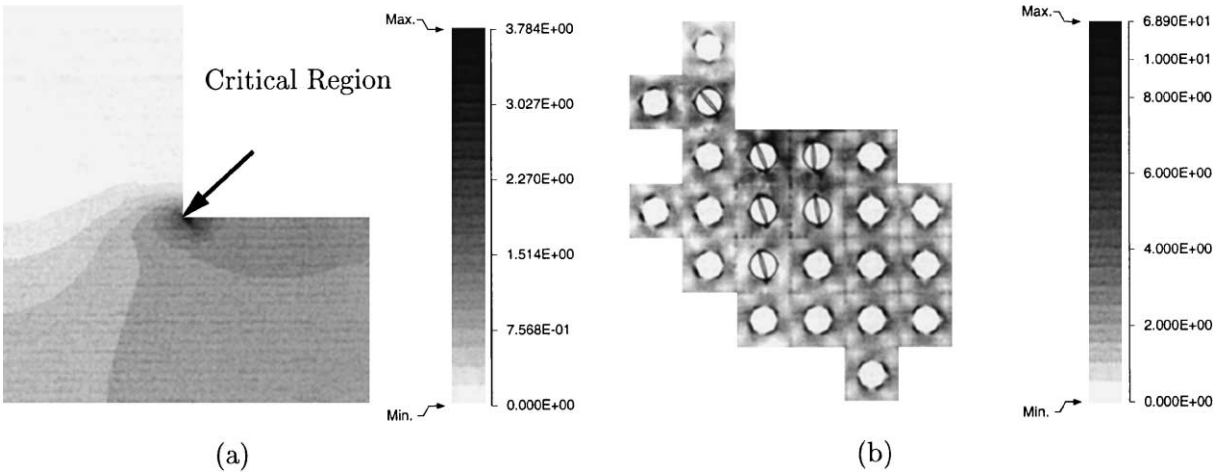

Fig. 17. Contour plot of plastic strain $\bar{e}^p$ for the composite square plate: (a) the macroscopic averaged strain and (b) the level-2 microscopic strain at the critical region for the larger RVE (ii) model.

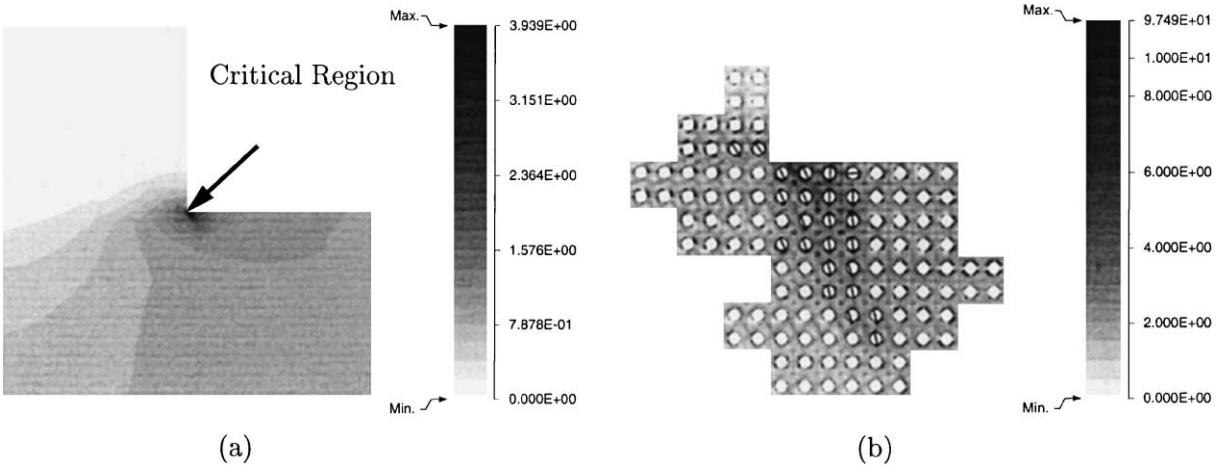

Fig. 18. Contour plot of plastic strain $\bar{e}^p$ for the composite square plate: (a) the macroscopic averaged strain and (b) the level-2 microscopic strain at the critical region for the smaller RVE (i) model.

to particle damage. The histogram of the evolution of particle cracking however shows a considerably different pattern and a much higher rate of cracking for RVE (i).

The same problem is solved for porous microstructures with the two sized RVE's, but with a total displacement of 0.4 mm. The evolved levels and meshes in the computational models at the end of loading are shown in Fig. 21(a) and (b) and the corresponding level-2 microstructures in Fig. 21(c) and (d). The evolution of the computational domain is also charted in Table 4. It is interesting to note that the difference in response for the two RVE's is insignificant this case. This may be attributed to lack of matrix damage or softening in the model. The plastically hardening matrix does not trigger adequate difference in the adaptation criteria as the particle cracking does for composites. A larger level-1 domain opens up with the adaptation criteria for elements which appear to be on the verge of strain localization, but subsequently do

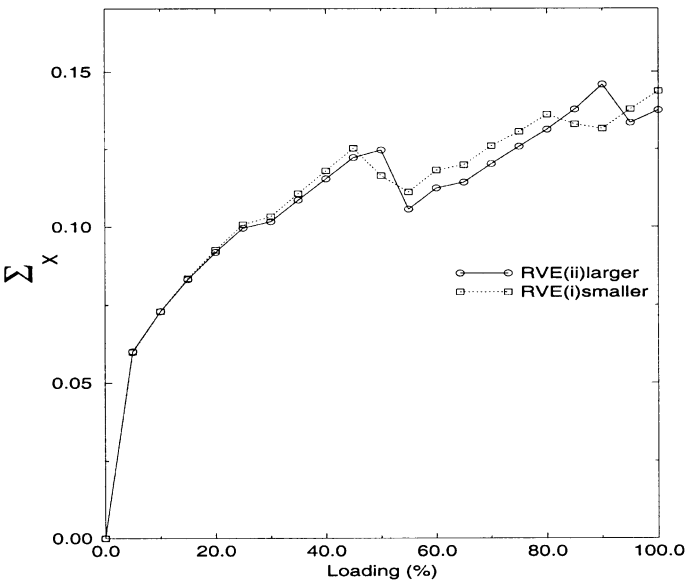

Fig. 19. The evolution of Σ_{xx} at the corner node of square hole for the two microstructures.

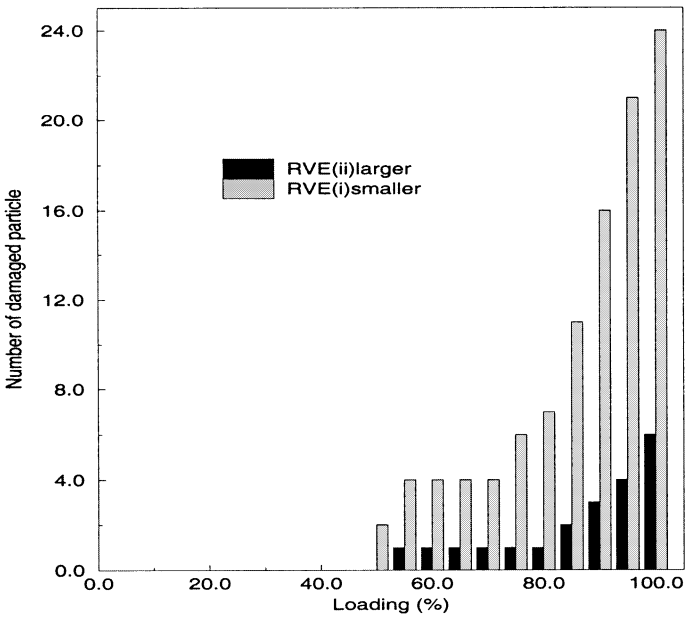

Fig. 20. Histogram of the number of damaged particles as a function of straining.

not make the transition to level-2. The contour plots of macroscopic and microscopic plastic strain distribution in Figs. 22 and 23, show similar macroscopic strain distributions, but higher strains for the microscopic model with smaller porosity RVE (i), due to the proximity of voids. This again shows the scale effect on the solution.

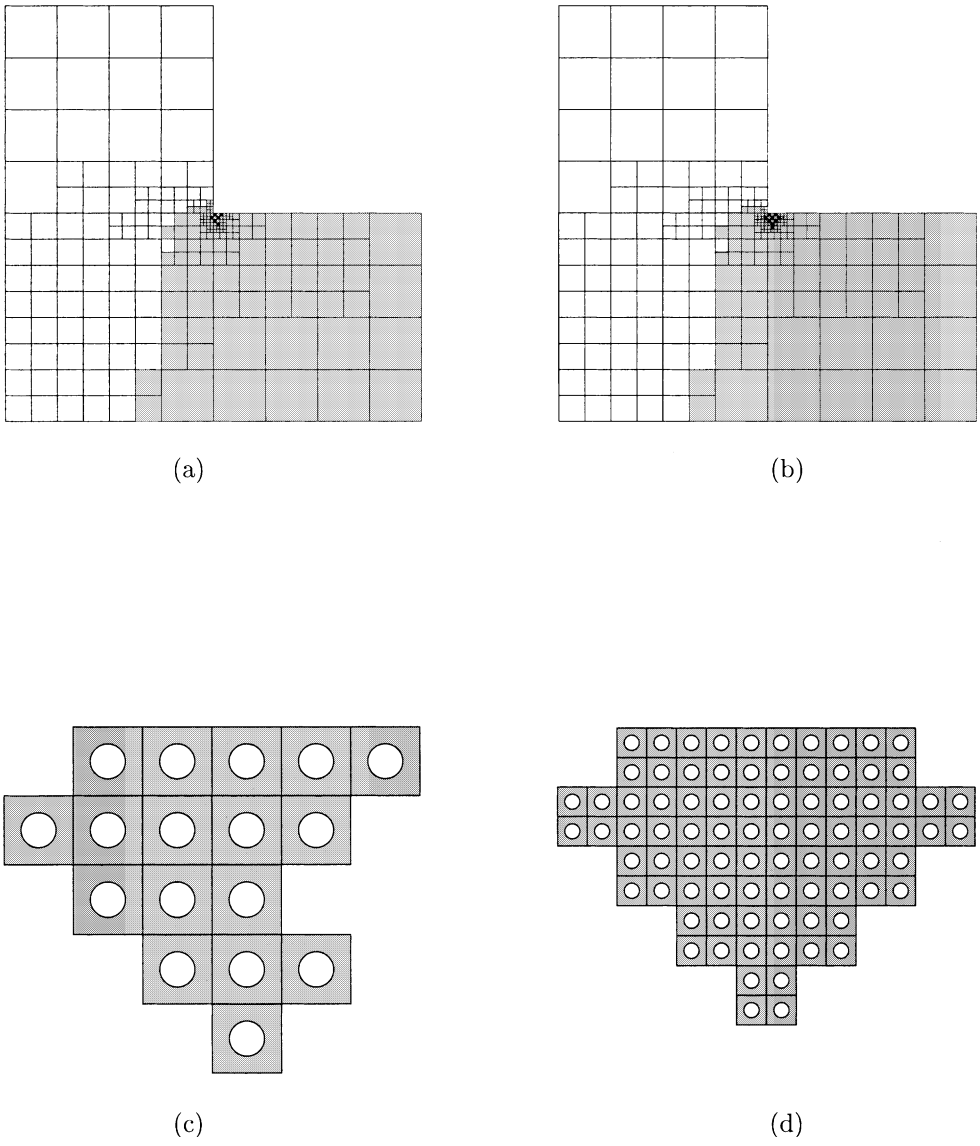

Fig. 21. Macroscopic three level evolved mesh for the porous material at the end of the loading cycle, for (a) the larger RVE (ii) and (b) smaller RVE (i); the corresponding level-2 region with the (c) the larger RVE (ii) and (d) smaller RVE (i). Level-0 is with white elements, level-1 is with grey elements and level-2 is with black elements.

Table 4
Evolution of elements at various levels with straining for porous microstructure

% of Total displacement	Level-0 elements		Level-1 elements		Level-2 elements		Total	
	RVE (i)	RVE (ii)	RVE (i)	RVE (ii)	RVE (i)	RVE (ii)	RVE (i)	RVE (ii)
25	196	196	2	2	0	0	210	210
50	175	175	21	21	4	4	201	201
75	128	128	68	68	7	7	204	204
100	94	94	111	111	17	17	222	222

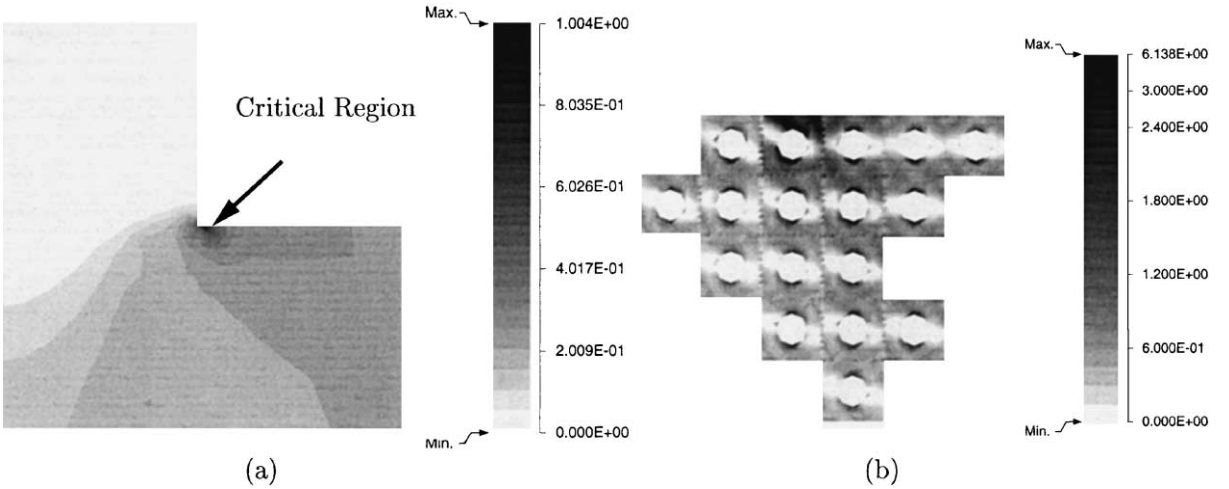

Fig. 22. Contour plot of plastic strain $\bar{e}^p$ for the porous square plate: (a) the macroscopic averaged strain and (b) the level-2 microscopic strain at the critical region for the smaller RVE (ii) model.

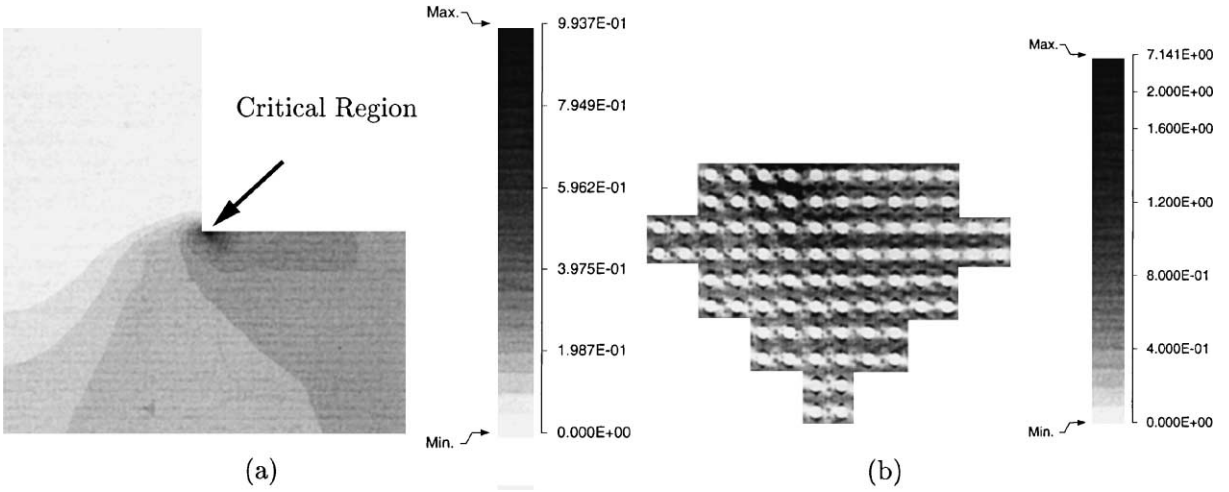

Fig. 23. Contour plot of plastic strain $\bar{e}^p$ for the porous square plate: (a) the macroscopic averaged strain and (b) the level-2 microscopic strain at the critical region for the smaller RVE (i) model.

10.2. Homogenization vs. multi-level simulation

The effect introducing level-2 elements on both macroscopic and microscopic response is studied by comparing a pure level-1 simulation of the square composite plate in the previous example with a multi-level simulation. The results shown are for the larger particles in RVE (ii). The Fig. 24 shows the microstructure near the inside corner by the two models at the end of loading. The boxed RVE's in Fig. 24(a) symbolize their periodic repetition. The periodicity constraint results in a considerably large portion of the microstructure being damaged for the homogenized simulation. The direction of the damage evolution

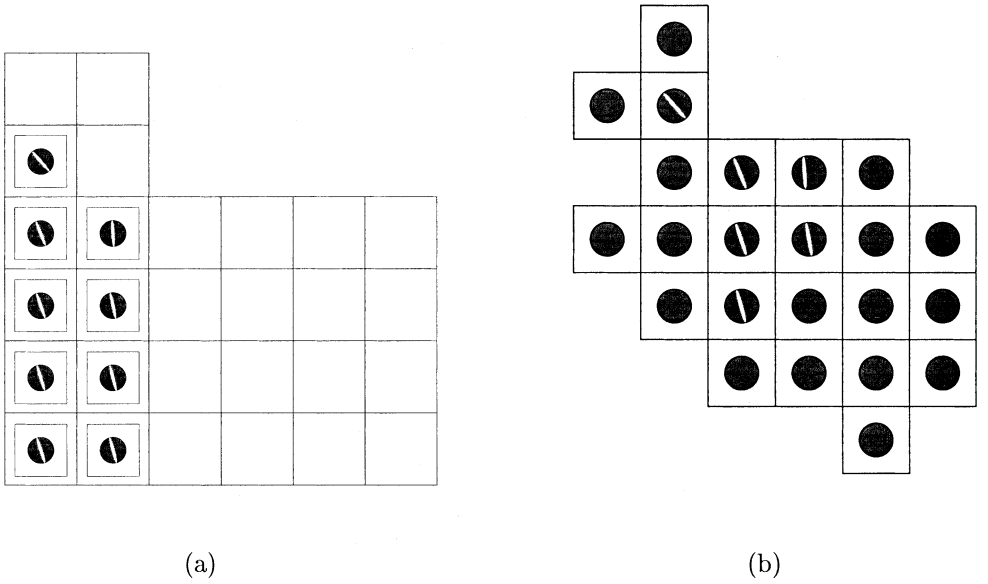

Fig. 24. A comparison of the microstructural evolution near the inside corner by (a) complete level-1 analysis and (b) adaptive multi-level analysis.

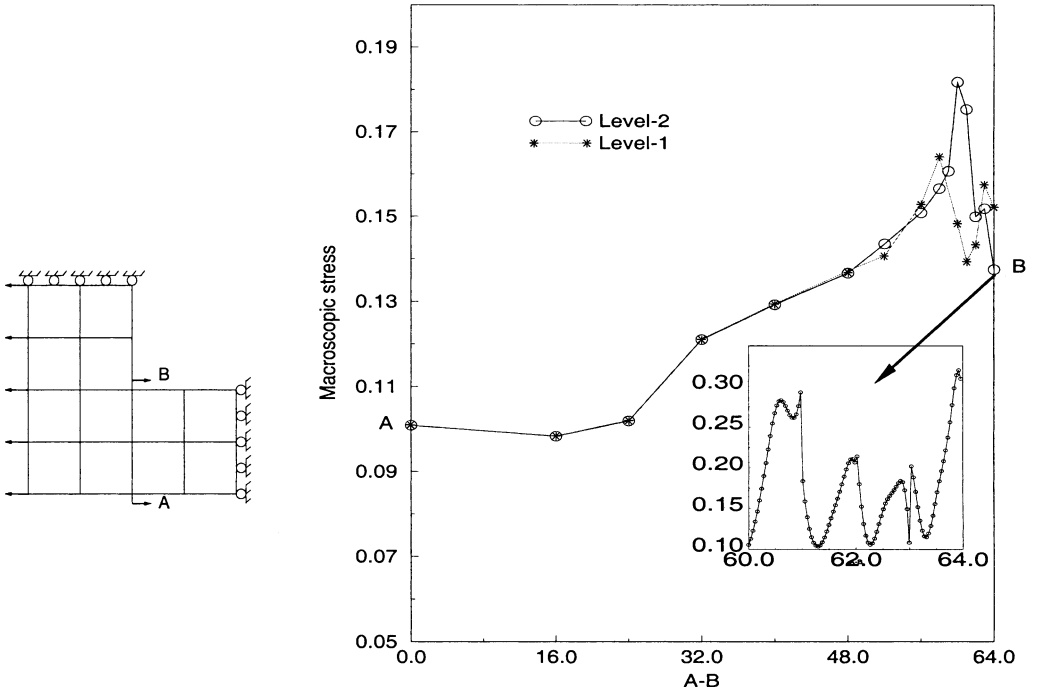

Fig. 25. Comparison of macroscopic stress Σ_{xx} along section A–B by level-1 and multi-level analysis.

indicated by the homogenized model is also different from the level-2 simulations. The stress Σ_{xx} along section A–B is plotted in Fig. 25 to evaluate the effect of homogenization on stress concentrations near the

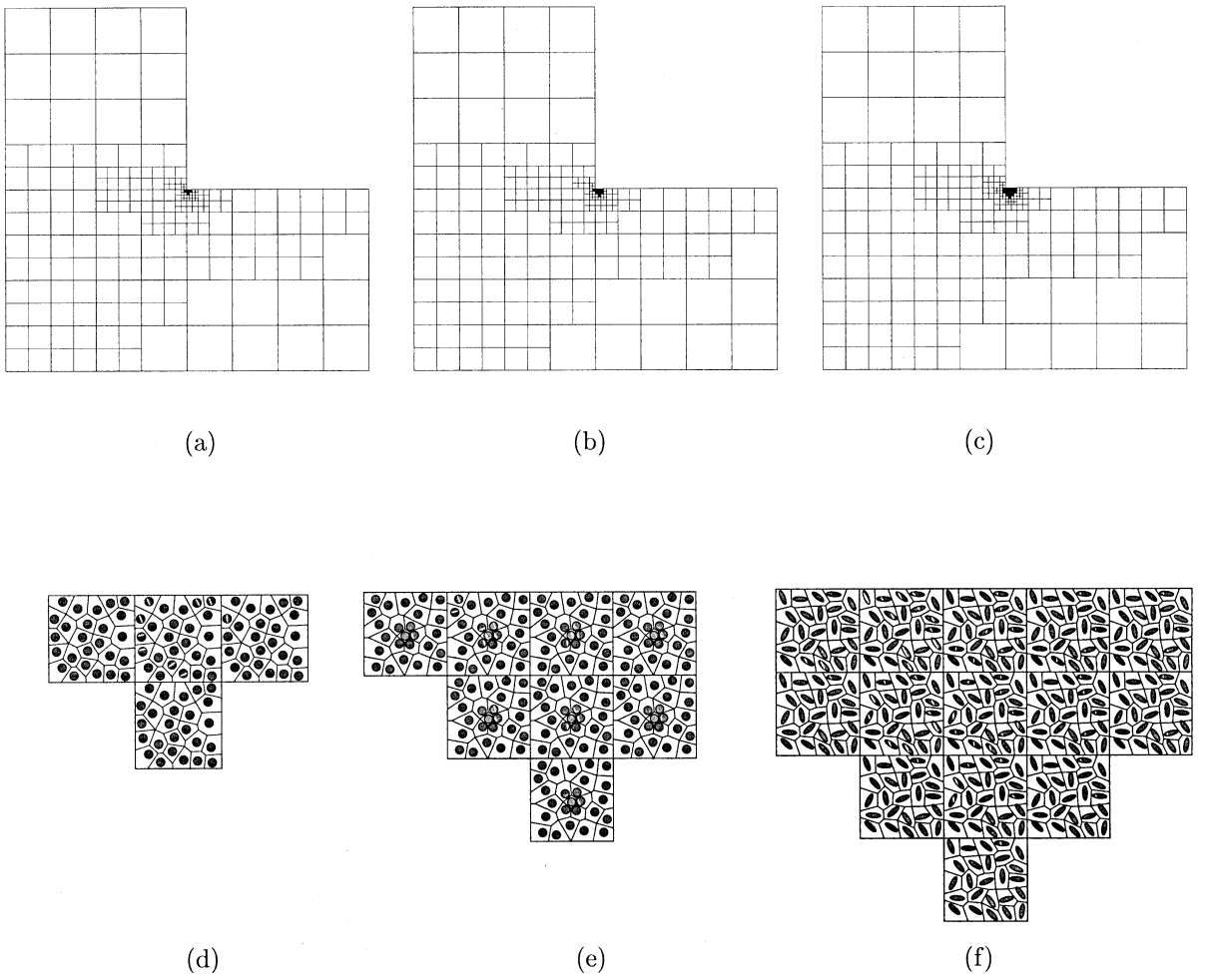

Fig. 26. Macroscopic three level evolved mesh for the composite material at the end of the loading cycle for (a) hardcore distribution with circular particles, (b) clustered distribution with circular particles, and (c) hardcore distribution with elliptical particles, the corresponding level-2 microstructures for (d) hardcore (e) clustered and (f) elliptical RVE's.

corner and free edge. The two models behave similarly upto the neighborhood of the corner. While the multi-level model predicts a higher peak near the corner, it subsides considerably to meet the traction free edge conditions. The corresponding microscopic level-2 stress variations for the multi-level model are shown in the inset.

10.3. Effect of heterogeneity distribution and shape

To illustrate the influence of particle distribution on the macro-microscopic damage response, two RVE's are selected with same volume fraction (20%), size (1.0 mm) and number of particles (25). One has a hardcore distribution (Fig. 15(b), iii), which is a random distribution with a minimum permissible distance between particles, while the other has one cluster in a hardcore background. Proximity of particles within the cluster is known to initiate damage in discrete microstructures. The starting macroscopic mesh is the

same as in the previous examples and a total displacement of 0.55 mm is applied on the edge in equal increments. The smallest allowed size of macroscopic elements by *h*-adaptation is set to 1 mm such that each E_{l2} element consists of one RVE.

The evolved macroscopic models for the two RVE's, at the finish of the loading cycle, are shown in Fig. 26(a) and (b). The level-2 region (black) for the clustered RVE is larger than that for the hardcore RVE. Within the E_{l2} elements, only one element for the hardcore distribution experiences particle damage as shown in Fig. 26(d). However, several E_{l2} elements for the clustered microstructure exhibit particle damage, mainly within the cluster (Fig. 26(e)). While the macroscopic averaged plastic strains show very little difference for the different microstructures in Figs. 27(a) and 28(a), the microscopic plots in Figs. 27(b) and 28(b) clearly depict the influence of distribution. Much higher levels of effective plastic strain values are observed within the cluster, compared to significantly lower levels in the hardcore RVE. Fig. 29 shows the evolution of macroscopic stress Σ_{xx} at the corner of the square hole and the number of damaged particles as a function of straining. The stress drops to lower values for the clustered RVE due to a larger damage microstructure. More than twice the number of particles are damaged for the clustered case as shown in the histogram.

To investigate the influence of shape, a RVE (Fig. 15(b) (iv)) with the same volume fraction (20%), size (1.0 mm) and number (25) is considered. The particles are elliptical with aspect ratio 3.0 and randomly distributed and oriented. The evolved macroscopic model in Fig. 26(c) shows a larger level-2 region compared with other two microstructures, with several E_{l2} elements exhibiting particle damage. The much larger number of cracked particles is also observed from the histogram of Fig. 29(b). For this case, both macroscopic and microscopic plastic strains in Fig. 30 are also considerably larger. The macroscopic stress Σ_{xx} shows a larger drop due to the increased damage in the microstructure.

10.4. A heterogeneous plate with a macroscopic holes

A different macroscopic domain, viz. a plate with periodically repeated square diagonal array of circular holes is considered in this final example. The plate is incrementally loaded using prescribed displacement on

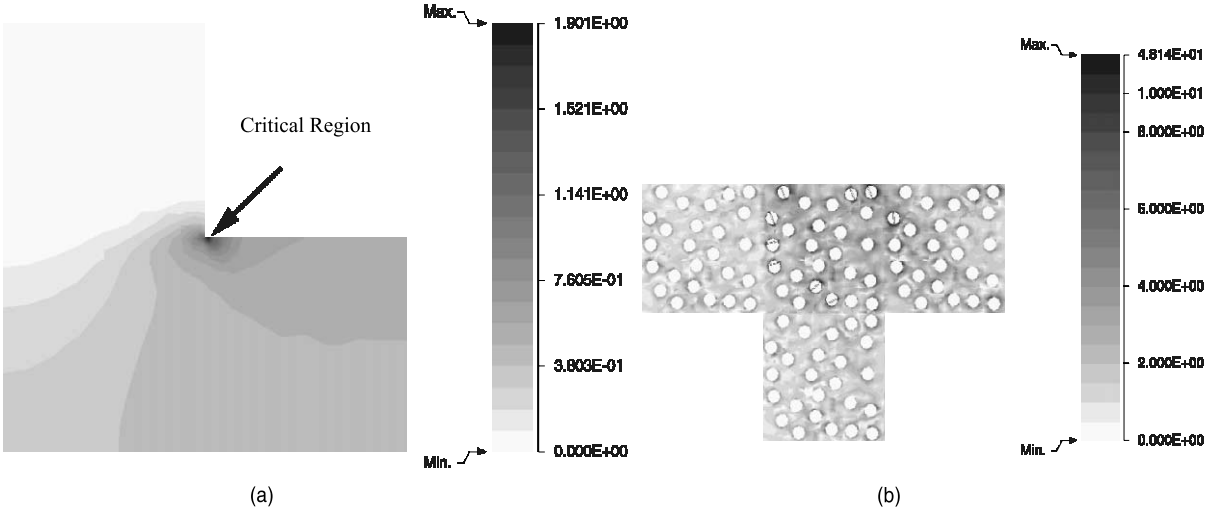

Fig. 27. Contour plot of plastic strain $\bar{e}^p$ for the composite square plate: (a) the macroscopic averaged strain and (b) the level-2 microscopic strain at the critical region for the hardcore RVE model.

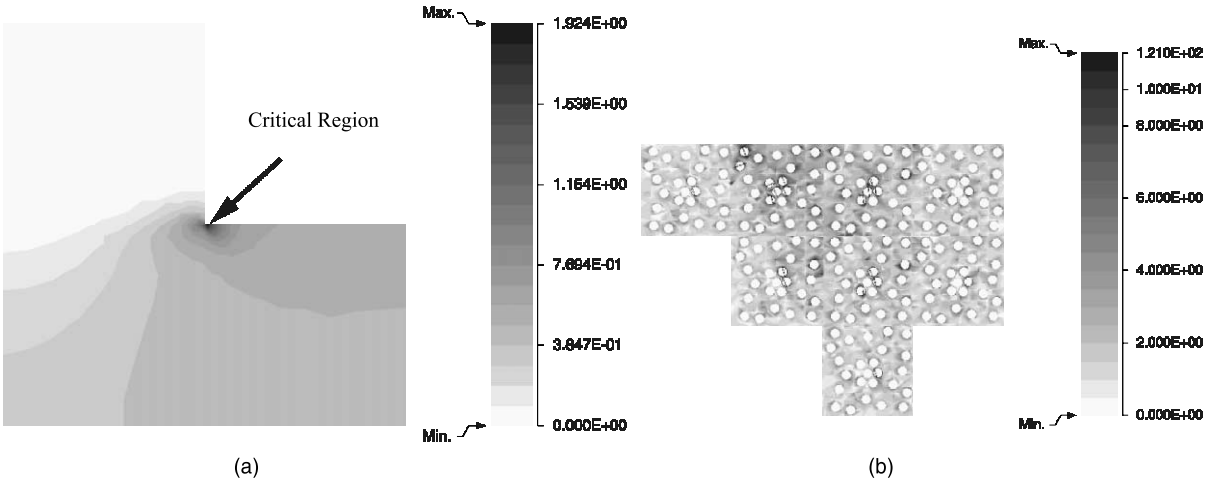

Fig. 28. Contour plot of plastic strain $\bar{e}^p$ for the composite square plate: (a) the macroscopic averaged strain and (b) the level-2 microscopic strain at the critical region for the clustered RVE model.

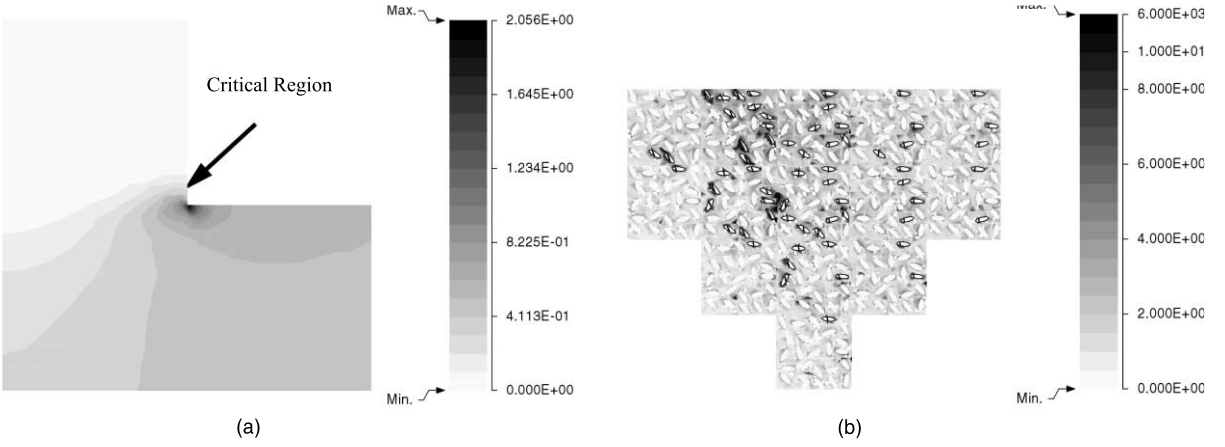

Fig. 29. The evolution of (a) Σ_{xx} at the corner node of square hole and (b) the number of damaged particles for the three microstructures.

the top and bottom surfaces to a total extension of 0.15 mm. Due to periodicity and symmetry, only a part of domain is modeled as shown in Fig. 31. The radius of the circular holes are 50 mm for the 100 mm $\times$ 100 mm square plate as shown in Fig. 31. The microstructural RVE is a 20% volume fraction 0.4 mm $\times$ 0.4 mm square region with a single circular particle. The same material properties as in the previous example are used with the only exception being that the critical particle cracking stress $\sigma^{cr} = 0.2$ GPa.

The adapted multi-level computational domain is shown in Fig. 32 and the number of elements in each levels with increasing are tabulated in Table 5. The level-2 elements are created along a clear path connecting the holes due to localization by particle cracking. Extended portions of the damaged microstructure in level-2 regions are shown in Fig. 32. The macroscopic plastic strain contour in Fig. 33(a) gives

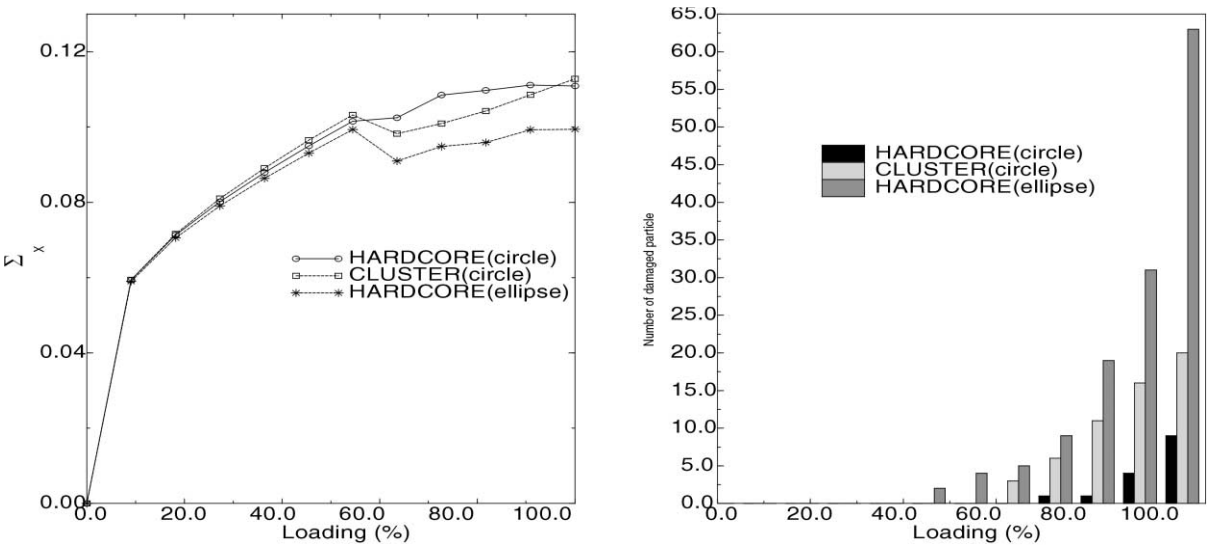

Fig. 30. Contour plot of plastic strain $\bar{e}^p$ for the composite square plate: (a) the macroscopic averaged strain and (b) the level-2 microscopic strain at the critical region for the clustered RVE model.

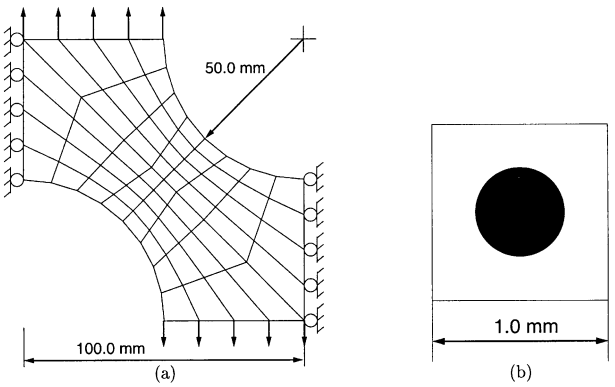

Fig. 31. (a) Finite element model for a part of the composite plate with two circular holes and (b) the VCFE model of the microstructural composite RVE.

an indication of 'hot spots' of evolving damage near the central region. The microscopic strain plots in Fig. 33(b) show a large fraction of particles cracked and may be interpreted as the initiation of localization to cause failure between the holes.

11. An example on convergence of the multi-level method

To provide convergence characteristics of the multi-level model, an example problem of an elastic fibrous composite with a free-edge and loaded in the out of plane direction, is considered. This classical

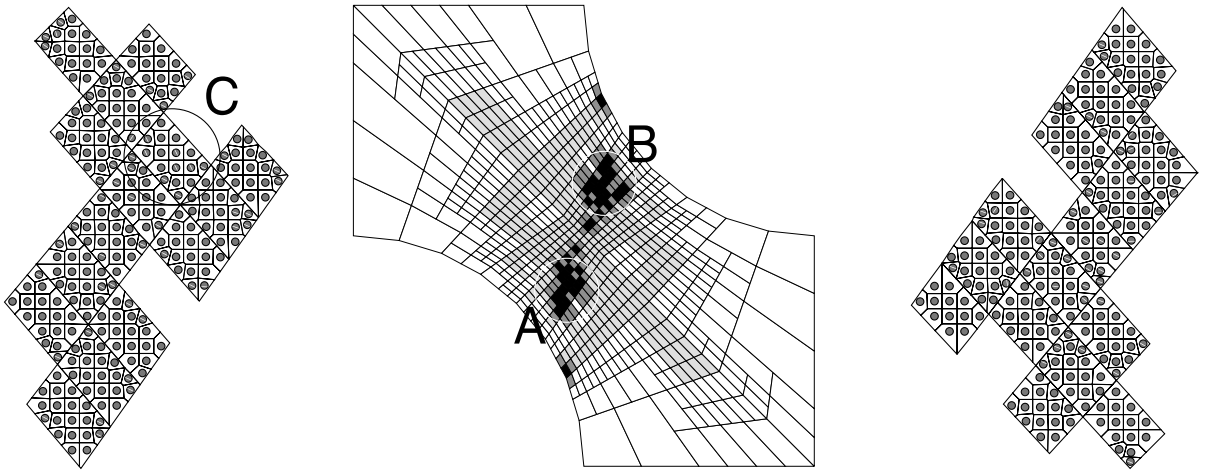

Fig. 32. Macroscopic three level evolved mesh for the composite plate with two holes at the end of loading. The level-2 regions in the microstructure are shown at the two regions A and B.

Table 5
Evolution of elements at various levels with straining for plate with holes

% of Total displacement	Level-0 elements	Level-1 elements	Level-2 elements	Total
16.6	100	0	0	100
33.2	142	0	0	142
49.8	134	20	0	154
66.4	284	98	0	382
83.0	296	164	0	460
91.5	329	237	68	634
100.0	326	272	102	700

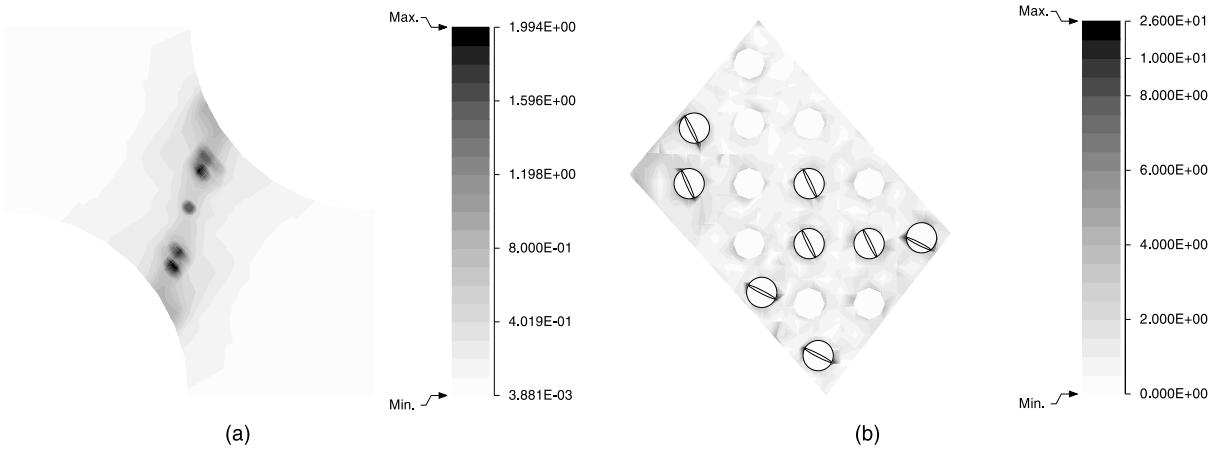

Fig. 33. Contour plot of (a) the macroscopic plastic strain $\bar{\varepsilon}^p$ and (b) level-2 microscopic plastic strain $\bar{\varepsilon}^p$ at the region C of the microstructure in Fig. 32.

problem was proposed by Pagano and Rybicki (1974) to demonstrate the limitations of effective modulus or homogenization theory in predicting stress states in laminated composites, especially near the free-edge. The problem consists of a composite cross-section as shown in Fig. 34(a). The upper half of the cross-section consists of n periodic rows of aligned cylindrical fibers, arranged in a square array, while the bottom half is the homogeneous matrix material. The ratio of fiber radius to edge length in the local RVE of Fig. 34(b) is $r/l = 0.3$, corresponding to a local volume fraction of 28.2%. The body is subjected to a generalized plane strain loading with out-of-plane loading, prescribed as $\epsilon_{zz} = 1$. Due to symmetry in the xz and yz planes only one quarter of the laminate is modeled (Fig. 34(a)). Symmetric boundary conditions are employed on the surfaces $x = 0$ and $y = 0$, and the top and right surfaces are assumed to be traction free. The material properties for the boron fiber and epoxy matrix are prescribed as $E_{\text{boron}} = 60 \times 10^6$ psi, $v_{\text{boron}} = 0.2$, $E_{\text{epoxy}} = 0.5 \times 10^6$ psi and $v_{\text{epoxy}} = 0.34$.

11.1. Microscale VCFEM simulations

To establish convergence of solutions at the microscale, the adaptive Voronoi cell finite element model (AVCFEM) developed in Moorthy and Ghosh (2000) is coupled with the multi-level computational model. In AVCFEM, two error measures are introduced to measure the quality of the solution. They are (i) the traction reciprocity error, derived a-posteriori from solved traction discontinuity at the element boundary and matrix-inclusion/void interface, and (ii) the error in kinematic relationships that is equated to an error in the strain energy, in each of the element constituent phases. Displacement adaptations that minimize traction discontinuity, are implemented to approach 'optimal' directions for displacement fields on the boundary/interface. These directions optimize the virtual work due to traction discontinuity and are obtained as components of the traction discontinuity in directions, orthogonal to the original displacement field. It is achieved through h-adaptation by adding displacement degrees of freedom in the x- or y-directions on the boundary/interface. This is followed by polynomial or spectral p-enrichment of boundary element interpolation functions [**L**]. The error in kinematic relations may be minimized by enhancing the stress functions by polynomial enrichment or $^{\text{enr}}p$-adaptation in the matrix and inclusion phases. Since the enrichments are carried out simultaneously for all elements, the adaptation has elements of minimizing

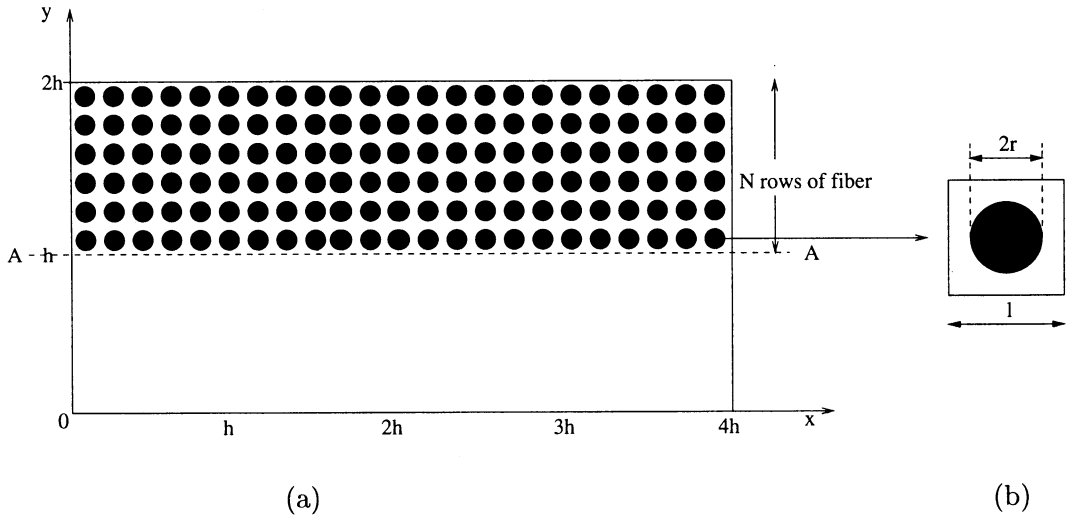

Fig. 34. A composite cross-section with n periodic layers of circular fibers, (b) a representative volume element for the effective medium theory calculations.

both local and pollution errors in the microstructure. Numerical analyses of several microstructures with different distributions, sizes and shapes of heterogeneities have shown a superior convergence rate with these adaptations.

The adaptive VCFEM of Moorthy and Ghosh (2000) is incorporated to reduce error in microstructural simulations, especially in level-2 elements. To illustrate the effect of microscale adaptation, a simplified form of the problem posed above, with one row of four fibers is considered. The mesh consists of 4 Voronoi cell elements as shown in Fig. 35(a). The matrix stresses in the hybrid formulation are constructed from an Airy's stress function consisting of a 12 term fourth-order polynomial expansion and a 36 term reciprocal function (Moorthy and Ghosh, 1996, 2000). The inclusion stresses are constructed using a 25 term, sixth-order polynomial function. Displacement fields corresponding to Eq. (22) are constructed with linear shape functions for element boundaries and quadratic shape functions for curved interface elements. The sequence of adaptations consists of two cycles of h – followed by a cycle of p-adaptation of displacement degrees of freedom, followed by a cycle of $^{\mathrm{enr}}p$-adaptation of the stress functions. The adapted mesh, showing added displacement degrees of freedom, is illustrated in Fig. 35(a). The pre-adaptation nodes are marked with a •, the x direction nodal adaptations are marked with a □ while those in the y direction are shown with △. The convergence of the VCFEM solutions is shown in Fig. 35(b), only for the average traction reciprocity error or (ATRE) as a function of the total degrees of freedom. The ATRE is calculated as (Moorthy and Ghosh, 2000)

$$\mathrm{ATRE} = \frac{\sum_{\tilde{e}_E=1}^{\tilde{N}_E} e_T^E + \sum_{\tilde{e}_I=1}^{\tilde{N}_I} e_T^I}{\tilde{N}_E + \tilde{N}_I}, \tag{48}$$

where $\tilde{N}_E$, $\tilde{N}_I$, e_T^E and e_T^I correspond to the total number of segments and the traction reciprocity error on the element boundary and interface elements, respectively. The degrees of freedom (DOF) correspond to

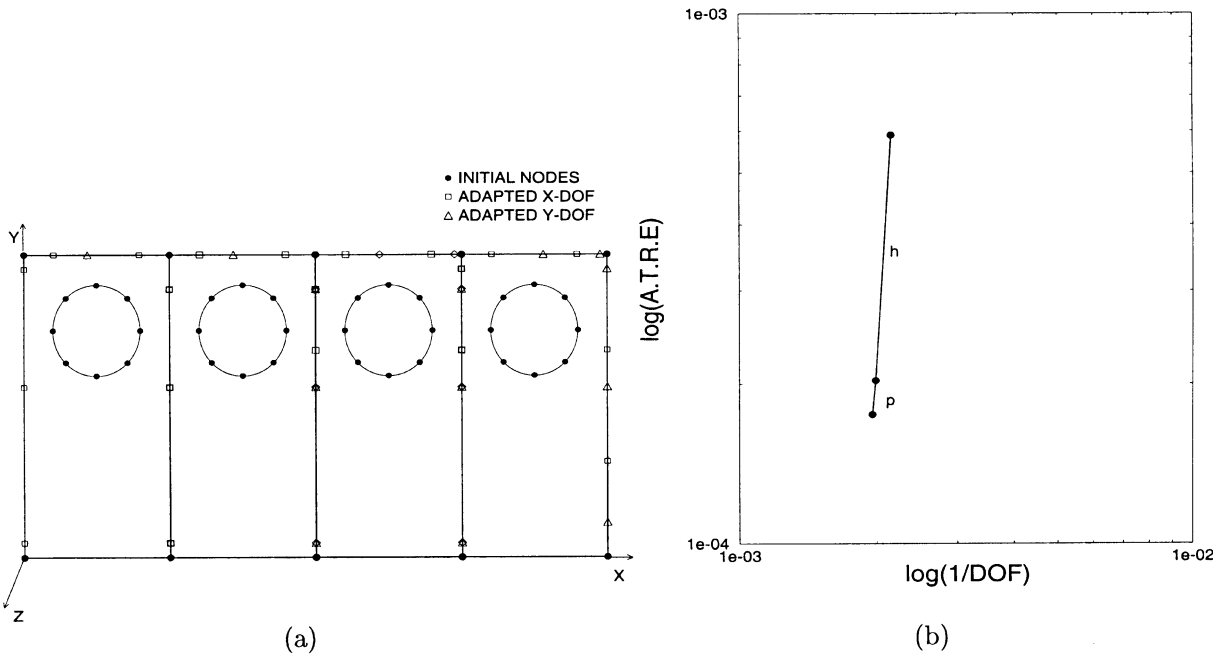

Fig. 35. (a) A microstructural h–p-adapted VCFEM mesh showing locations of the initial and added nodes with x- and y-DOF; (b) solution convergence rate in terms of average traction reciprocity error (ATRE) as functions of inverse of the DOF.

Table 6
Statistics of *h*–*h*–*p*-adaptation for the elastic composite materials with circular fibers

Adaptation	Initial	*h*-1	*h*-2	*p*
DOF	464	569	748	807
ATRE	0.03592	0.011933	0.003726	0.002417

the sum of the total number of nodal degrees of freedom and the number of β stress parameters, i.e. $\mathrm{DOF} = 2 * N_{\mathrm{nodes}} + N_{\beta}$. Table 6 and Fig. 35(b) provide numerical details of ATRE with added degrees of freedom due to each adaptation, on the boundary and interface only. Discrete points in the figure correspond to the different stages of adaptation. The first two drops are for the two consecutive cycles of *h*-adaptation and the third for *p*-adaptation. The traction reciprocity error reduces rather drastically in the *h*-adaptation cycles, i.e. a 90% change in ATRE is obtained with a 61% increase in DOF. With the subsequent *p*-adaptation, and additional 4% change in ATRE is obtained with a further 13% increase in DOF. Since very little ATRE reduction is gained beyond two cycles of boundary *h*-adaptations, only these are employed for the multi-scale simulations of this section.

A comparison study is made with the solutions in Pagano and Rybicki (1974) (the same results are also generated by the commercial code ANSYS). The ANSYS mesh, for which convergence is achieved has 4230 QUAD4 elements and 4352 nodes. The microscopic in-plane stress σ_{yy} plots along horizontal sections $y = h$ are compared for the unadapted VCFEM, adapted VCFEM and the ANSYS model in Fig. 36. It should be noted that the transverse stress σ_{yy} is approximately two orders lower compared to the leading order stress σ_{zz} and hence convergence is harder to achieve. Results of the adapted VCFEM results agree very well with those of the converged ANSYS model. This is therefore a strong attestation of the accuracy of the adaptive VCFEM solutions. The figure also shows the singular nature of the solution in the free edge region when effective modulus theory by homogenization is used. Since this is physically unattainable, detailed micromechanics solutions are needed in this region.

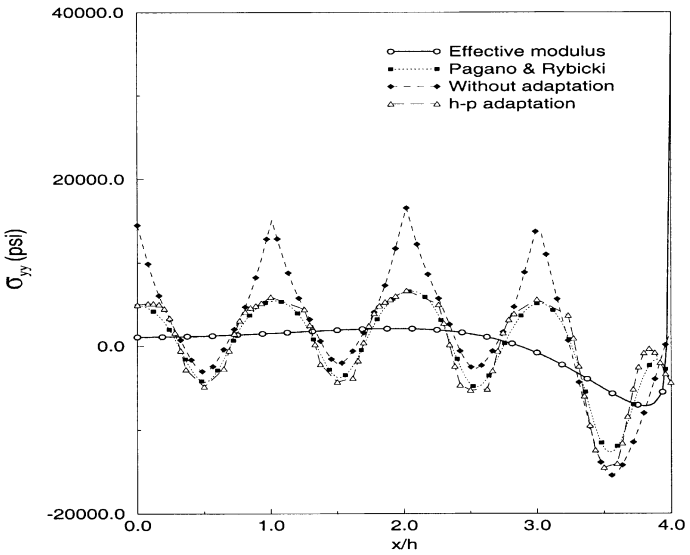

Fig. 36. σ_{yy} distribution at Section A–A ($y = h$) for the composite section with one row of fiber.

11.2. Multi-level simulations

To test convergence of the overall model qualitatively, the composite problem with 40 ($n = 40$) rows of 6400 fibers is simulated by the multi-level code. The level-0/1 h-adaptation criterion is based on a traction jump criterion across adjacent element boundaries, stated as

$$\text{Refine element if } E_i \geqslant \text{C1} * E_{\text{avg}} \quad \text{where } E_{\text{avg}} = \frac{\sum_{i=1}^{NE} E_i}{NE}, \quad E_i = \frac{\int_{\partial Y} ([|T_x|]^2 + [|T_y|]^2)^{1/2} \mathrm{d}\partial Y}{\int_{\partial Y} \mathrm{d}\partial Y}, \tag{49}$$

where NE is the total number of level-0/1 elements. This criterion is intended for signaling and zooming in on regions high stress gradients. For level-0 to level-1, the transition is made based on element jump in the significant stress σ_{yy}, in addition to the traction jump condition of Eq. (49), stated as

$$\text{Level-0} \rightarrow \text{Level-1} \quad \text{if } E_i \geqslant \text{C2} * E_{\text{avg}} \text{ or } {}^{y}E_i \geqslant \text{C2} * {}^{y}E_{\text{avg}} \quad \text{where } {}^{y}E_i = \frac{\int_{\partial Y} [|\sigma_{yy}|] \mathrm{d}\partial Y}{\int_{\partial Y} \mathrm{d}\partial Y}, \tag{50}$$

where C1, C2 are prescribed constants. Finally, the level-1 to level-2 transition is made from observations made in the microstructural RVE's of level-1 elements. It is based on the ratio of local energy density (at each integration point of VC element) to the average energy density for the entire RVE (aggregate of VC elements). The procedure followed for determining this is:

- Solve the RVE problems with periodicity boundary conditions and four sets of applied macroscopic strains, viz. (i) $e_{xx} = 1,\ e_{yy} = 0,\ e_{xy} = 0,\ e_{zz} = 0$, (ii) $e_{xx} = 0,\ e_{yy} = 1,\ e_{xy} = 0,\ e_{zz} = 0$, (iii) $e_{xx} = 0,\ e_{yy} = 0,\ e_{xy} = 1,\ e_{zz} = 0$ and (iv) $e_{xx} = 0,\ e_{yy} = 0,\ e_{xy} = 0,\ e_{zz} = 1$.
- For all cases (i–iv) evaluate the energy densities at integration point of the matrix and inclusion phases as $U^{\text{mat/incl}} = S_{ijkl}^{\text{mat/incl}} \sigma_{ij} \sigma_{kl}$, where S_{ijkl} is the compliance tensor.
- Evaluate the energy density concentration factors:

$$R^{\text{mat}} = \frac{\text{Maximum } U^{\text{mat}} \ (= U^{\text{mat}}_{\text{max}})}{RVE \text{ Averaged } U^{\text{mat}} \ (= U^{\text{mat}}_{\text{aver}})} \quad \text{and} \quad R^{\text{incl}} = \frac{\text{Maximum } U^{\text{incl}} \ (= U^{\text{incl}}_{\text{max}})}{RVE \text{ Averaged } U^{\text{incl}} \ (= U^{\text{incl}}_{\text{aver}})}.$$

- In the multi-level problem with actual strain components, the transition is made according to

$$\text{Level-1} \rightarrow \text{Level-2 if } {}^{\text{actual}}U^{\text{mat}}_{\text{max}} \geqslant R^{\text{mat}} \bigstar {}^{\text{actual}}U^{\text{mat}}_{\text{aver}} \text{ or } {}^{\text{actual}}U^{\text{incl}}_{\text{max}} \geqslant R^{\text{incl}} \bigstar {}^{\text{actual}}U^{\text{incl}}_{\text{aver}}, \tag{51}$$

at more than 1% of all integration points.

The initial mesh consists of 200 level-0 QUAD4 elements. To examine the dependence of results on adaptation parameters, two sets of parameters viz. ($\text{C1} = 1.5, \text{C2} = 2$) and ($\text{C1} = 1.25, \text{C2} = 1.5$) are experimented with. Fig. 37(a) and (b) show the h-adapted level-0/level-1/level-2 meshes with the different adaptation parameters. The first set leads to 391 level-0 elements, 0 level-1 elements, six transition elements and four level-2 elements, while the second set has 475 level-0 elements, four level-1 elements, nine transition elements and six level-2 elements. The microstructural RVE or unit cell is assumed to be of dimension $l = h/80$ and the level-2 elements are assumed to contain a single unit cell. The same problem is also solved using the commercial code ANSYS with a mesh of 30 000 elements, for which a 3×3 array of fibers near the free-edge and laminate interface are modeled explicitly (see Fig. 37(c)). In Fig. 38(a) the macroscopic response of level-0 elements, with homogenized effective moduli, is plotted. The figure shows the effect of mesh dependence in the solutions near the free-edge. With increasing cycles of adaptations the artificial stress singularity moves towards the free edge and gains intensity. In Fig. 38(b) the microscopic level-2 stresses are plotted in the vicinity of the free edge (indicated as L2 in Fig. 38(a)). It is clearly seen that are artificial singularity of homogenized solutions no longer exist and there is no mesh dependence near the free

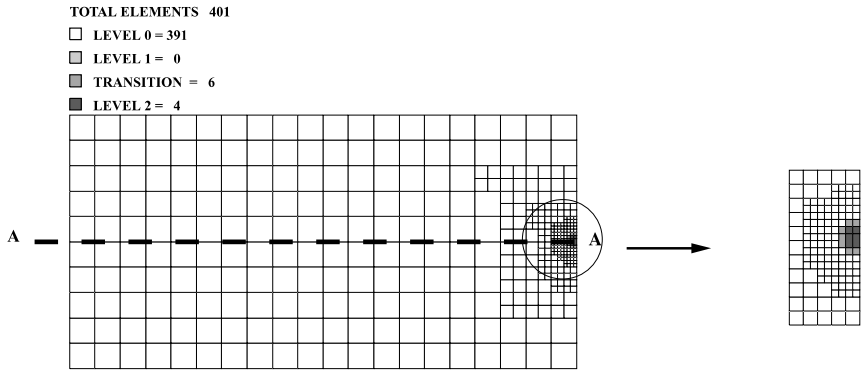

(a)

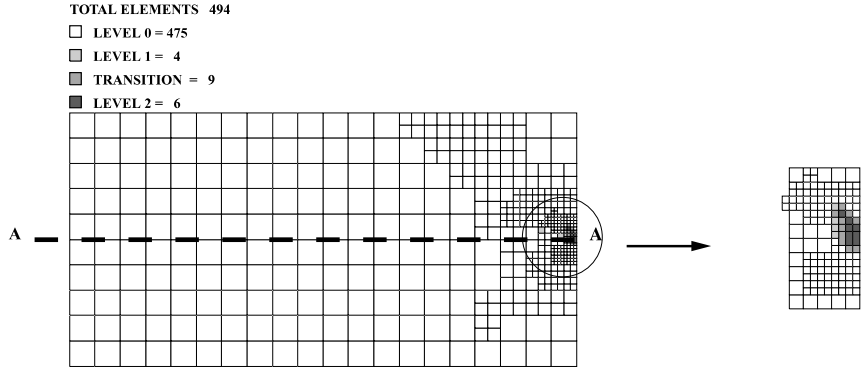

(b)

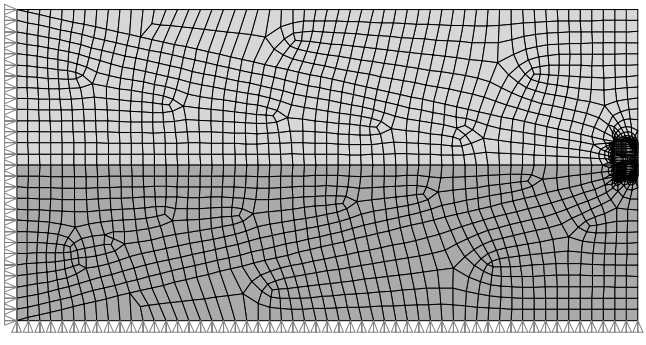

(c)

Fig. 37. (a,b) *H*-adaptive multi-level mesh showing level-0, level-1 and level-2 for two different parameters in transition criteria, and (c) a corresponding ANSYS mesh with detailed microstructure modeled near the free edge.

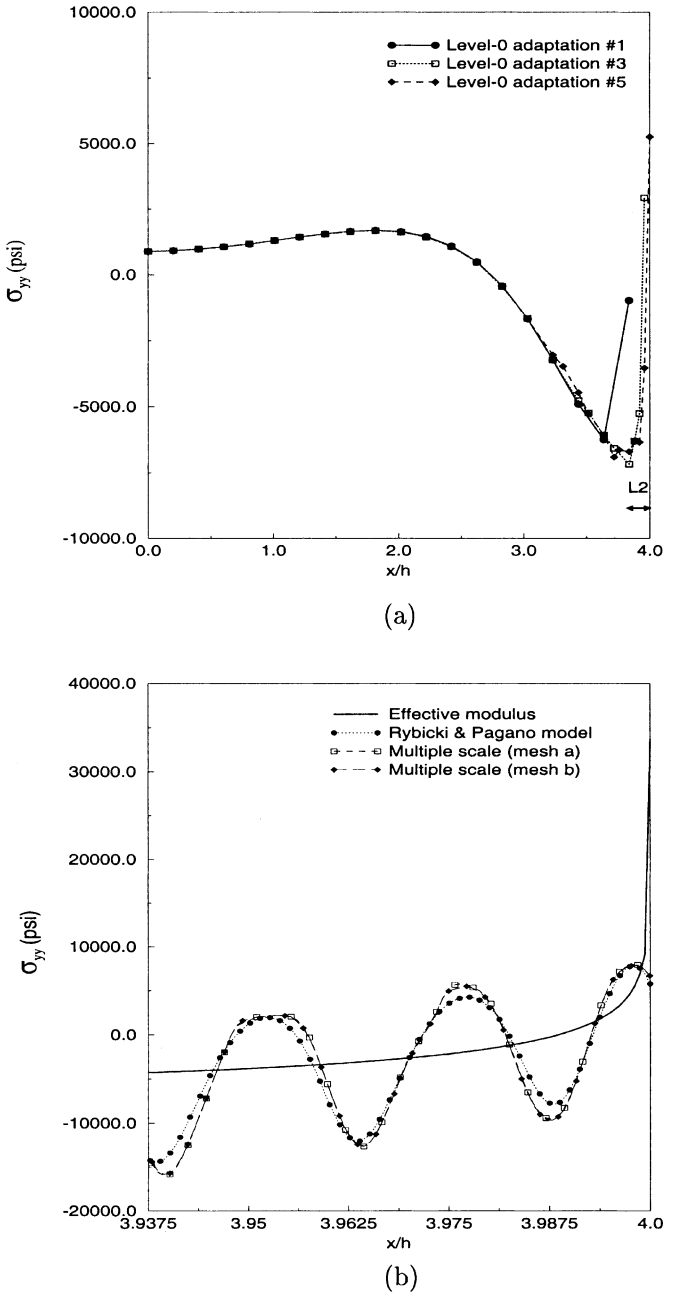

Fig. 38. Convergence of stress σ_{yy} at Section A–A ($y = h$): (a) macroscopic stress plots using the homogenized moduli and level-0 elements, (b) microscopic level-2 stress plots near the critical free-edge region.

edge. The two multi-level meshes of Fig. 38(a) and (b) and the ANSYS model all produce similar results. Thus, through this example, the convergence characteristics of the multi-level model is qualitatively verified and confidence is gained about its application.

12. Discussion and conclusion

Adaptivity in the computational modules for multiple scale problems entails minimizing two types of errors, viz. the discretization error and the modeling error. In this paper, an adaptive multi-level method is proposed to primarily focus on reducing the modeling error and predicting the evolution of stresses, strains and damage at the structural and microstructural scales. The microstructural analysis is conducted with the VCFEM for elastic–plastic constituents with particle cracking. VCFEM allows for continuous change in element topology due to progressive damage with high accuracy as shown in Moorthy and Ghosh (2000) and Ghosh and Moorthy (1998). The efficiency of the method, due to embedding micromechanics in FEM formulation, makes modeling of large microstructural regions relatively easy. A conventional displacement based elastic–plastic FEM code is developed for macroscopic analysis. Adaptive mesh refinement and level transition strategies are developed to create a hierarchy of computational subdomains with varying resolutions. This differentiates between non-critical and critical regions and helps in increasing the efficiency of computations by preferential 'zoom in'.

Three levels of hierarchy, viz. level-0, level-1 and level-2, evolve in the multi-scale model with progressive deformation. A piecewise continuous elastic–plastic constitutive law is developed for level-0 simulations. The specialty of this model is that since it is developed from rigorous micromechanical simulations with precise material morphology, it is sensitive to variations in the microstructural distribution. The constitutive relation leads to very high efficiency in simulations when compared with two-scale analysis by homogenization (e.g. Guedes and Kikuchi, 1991).

Level-0 simulations are accompanied by mesh-refinement using h-adaptation techniques, to reduce discretization error in the computational model and zoom in on regions of evolving localization due to microscopic non-homogeneity. The criteria for h-adaptation are based on gradients or jumps in plastic work or stresses. While these error criteria are effective in equi-distributing discretization errors where solutions are relatively regular, they are also helpful in identifying regions of localization or singularity due to steep gradients in the solution variables. It should however be mentioned that the proposed refinement schemes and error criteria are by no means optimal. For example, it has been shown in Guo and Babuska (1986) and Rank and Babuska (1987) the h–p-adaptation, which combines local mesh refinement with increase of the polynomial order of interpolants, enjoy exponential rate of convergence and excellent accuracy especially for problems with singularity. Additionally, it has been demonstrated in Oden and Feng (1996) and Babuska et al. (1994), that local error estimation techniques are incapable of detecting pollution error particularly when singularities are present. A robust mesh adaptation procedure for reducing errors should therefore incorporate pollution error reduction criteria, as well as h–p-adaptation. Much of the ongoing and future efforts by the authors are focussed on introducing these techniques. Since the focus of this paper is more on the modeling errors, these implementations are deferred to future publications.

When imminent damage and localization are sensed by the code, the level-0 elements automatically switch to level-1 elements, which use computations both at the macroscopic and microscopic scales. The criteria for signaling such transition are non-unique and a number of them are considered in this study. Among those that yielded effective results are (i) when the homogenized constitutive relation has reached its limit; (ii) when the maximum macroscopic principal stress or hydrostatic stress exceeds a certain fraction of the microscopic fracture stress or (iii) when the macroscopic effective plastic strain or the dilatation exceeds certain pre-determined values. With the rise in local gradients of macroscopic variables or with microstructural damage, the pre-assumed representative volume element in the microstructure are no longer effective and a shift to complete microscopic simulations is necessary. Extended portions of the microstructure are directly modeled by VCFEM in these level-2 elements. An adaptive VCFE model (AVCFEM) is used to study convergence of the microstructural analysis model. In AVCFEM, traction reciprocity error and error in kinematic relationships are optimized through boundary/interface enrichment in the form of additional displacement degrees of freedom and interpolation orders, as well as through stress function

enhancement. In Moorthy and Ghosh (2000), excellent convergence rate of AVCFEM has been established for elastic and elasto–plastic microstructural analysis. For the problem considered in this paper, two cycles of boundary *h*-adaptation is found to achieve desirable results in the level-2 elements.

Several numerical examples are conducted with the multi-level model to examine the effect of various microstructural morphologies on the multi-scale response of composite and porous structural components. Specifically scale effects, effects of microstructural distribution and shapes and structural geometry, on the mechanical and damage response are investigated. In conclusions, the multi-level model has addressed a number of difficult issues in solving multi-scale problems. However, a number of avenues for further model enhancements remain. For example, the Newton–Raphson iteration scheme used for non-linear problems struggle for convergence, as more and more level-2 elements with damage emerge. The migration of boundaries between different levels within each iteration loop has an adverse effect on convergence as well. Also for the level-1 elements, an iterative loop is necessary for convergence of steps (a), (b) and (c) in Section 6. In addition, the issues of adaptivity mentioned above remain. These issues are currently being dealt with for making this an effective tool in the prediction of structural failure.

Acknowledgements

Support of this work by the Unites States Army Research Office through grant No. DAAHO4-95-1-0176 (Program Director: Dr. M.A. Zikry and Dr. K.R. Iyer), and by the National Science Foundation through NSF Young Investigator grant (Grant No. CMS-9457603) (Program Director K. Chong) is gratefully acknowledged. Computer support by the Ohio Supercomputer Center through grant # PAS813-2 is also gratefully acknowledged. The authors are also grateful to an anonymous reviewer for very insightful comments that helped improve this paper.

References

Babuska, I., Strouboulis, T., Mathus, A., Upadhyay, C.S., 1994. Pollution error in the h-version of the finite element method and the local quality of a-posteriori error estimators. Finite Elem. Anal. Des. 17, 273–321.

Bakhvalov, N.S., Panasenko, G.P., 1984. Homogenization in periodic media. Mathematical Problems of the Mechanics of Composite Materials. Nauka, Moscow.

Bao, G., Hutchinson, J.W., McMeeking, R.M., 1991. Plastic reinforcement of ductile matrices against plastic flow and creep. Acta Metallur. et Mater. 39.

Bass, J.M., Oden, J.T., 1987. Adaptive finite element methods for a class of evolution problems in viscoplasticity. Int. J. Engng. Sci. 25 (6), 623–653.

Belytschko, T., Fish, J., Bayliss, A., 1994. The spectral overlay on the finite element solution with high gradients. Comput. Meth. Appl. Mech. Engng. 81, 71–89.

Benssousan, A., Lions, J.L., Papanicoulau, G., 1978. Asymptotic analysis for periodic structures. North Holland, Amsterdam.

Cheng, C.-H., 1992. Modeling of the elasto-plastic behavior for composite materials using homogenization method. Ph.D. Dissertation, University of Michigan, MI.

Demkowicz, L., Devloo, Ph., Oden, J.T., 1985. On an h type mesh refinement strategy based on a minimization of interpolation error. Comp. Meth. Appl. Mech. Engng. 3, 67–89.

Devries, F., Dumontet, H., Duvaut, G., Lene, F., 1989. Homogenization and damage for composite structures. Int. J. Num. Meth. Engng. 27, 285–298.

Dvorak, G.J., Benveniste, Y., 1992. On transformation strains and uniform fields in multiphase elastic media. Proc. R. Soc. Lond. A 437, 291–310.

Fish, J., Belsky, V., 1995. Multigrid method for periodic heterogeneous media, part II: multiscale modeling and quality control in multidimensional case. Comp. Meth. Appl. Mech. Engng. 126, 17–38.

Fish, J., Nayak, P., Holmes, M.H., 1994. Microscale reduction error indicators and estimators for a periodic heterogeneous medium. Comput. Mech. 14 (4), 323–338.

Fish, J., Shek, K., Pandheeradi, M., Shephard, M.S., 1997. Computational plasticity for composite structures based on mathematical homogenization: theory and practice. Comp. Meth. Appl. Mech. Engng. 148, 53–73.

Fish, J., Wagiman, A., 1993. Multiscale finite element method for a locally non-periodic heterogeneous medium. Comput. Mech. 12, 164–180.

Ghosh, S., Lee, K., Moorthy, S., 1995. Multiple scale analysis of heterogeneous elastic structures using homogenization theory and Voronoi cell finite element method. Int. J. Solids Struct. 32 (1), 27–62.

Ghosh, S., Lee, K., Moorthy, S., 1996. Two scale analysis of heterogeneous elastic–plastic materials with asymptotic homogenization and Voronoi cell finite element model. Comp. Meth. Appl. Mech. Engng. 132, 63–116.

Ghosh, S., Moorthy, S., 1998. Particle fracture simulation in non-uniform microstructures of metal-matrix composites. Acta Mater. 46 (3), 965–982.

Ghosh, S., Nowak, Z., Lee, K., 1997. Quantitative characterization and modeling of composite microstructures by Voronoi cells. Acta Metall. et Mater. 45 (6), 2215–2234.

Guedes, J.M., 1990. Non-linear computational model for composite material using homogenization. Ph.D. Dissertation, University of Michigan, MI.

Guedes, J.M., Kikuchi, N., 1991. Preprocessing and postprocessing for materials based on the homogenization method with adaptive finite element methods. Comp. Meth. Appl. Mech. Engng. 83, 143–198.

Guo, B., Babuska, I., 1986. The h-p version of the finite element method. J. Comput. Mech. 1, 21–42.

Gurson, A.L., 1977. Continuum theory of ductile rupture by void nucleation and Growth-I, Yield criteria and flow rules for porous ductile media. J. Engng. Mater. Tech. 99, 2–15.

Hill, R., 1965. A self consistent mechanics of composite materials. J. Mech. Phys. Solids 13, 213–222.

Hollister, S.J., Kikuchi, N., 1992. A comparison of homogenization and standard mechanics analysis for periodic microstructure. Comput. Mech. 10, 73–95.

Hughes, T.J.R., 1995. Multiscale phenomena: Green's functions, the Dirichlet-to-Neumann formulation, subgrid scale models, bubbles and the origins of stabilized methods. Comp. Meth. Appl. Mech. Engng. 127 (1–4), 387–401.

Koh, B.C., Kikuchi, N., 1987. New improved hourglass control for bilinear and trilinear elements in anisotropic linear elasticity. Comp. Meth. Appl. Mech. Engng. 65, 1–46.

Lene, F., 1986. Damage constitutive relations for composite materials. Engng. Frac. Mech. 25 (5), 713–728.

Ladeveze, P., Oden, J.T. (Eds.), 1998. Advances in adaptive computational methods. Studies Applied Mechanics, 47, Elsevier, Amsterdam.

Lee, K., Moorthy, S., Ghosh, S., 1999. Multiple scale computational model for damage in composite materials. Comp. Meth. Appl. Mech. Engng. 172, 175–201.

Melosh, R.J., Marcal, P.V., 1977. An energy basis for mesh refinement of structural continua. Int. J. Num. Meth. Engng. 11 (7), 1083–1092.

Moorthy, S., Ghosh, S., 1996. A model for analysis of arbitrary composite and porous microstructures with Voronoi cell finite elements. Int. J. Numer. Meth. Engng. 39, 2363–2398.

Moorthy, S., Ghosh, S., 1998. A Voronoi cell finite element model for particle cracking in composite materials. Comp. Meth. Appl. Mech. Engng. 151, 377–400.

Moorthy, S., Ghosh, S., 2000. Adaptivity and convergence in the Voronoi cell finite element model for analyzing heterogeneous materials. Comp. Meth. Appl. Mech. Engng. 185, 37–74.

Oden, J.T., Feng, Y., 1996. Local and pollution error estimation for finite element approximations of elliptic boundary value problems. J. Comput. Appl. Math. 74 (1–2), 245–293.

Oden, J.T., Vemaganti, K., Moes, N., 1999. Hierarchical modeling of heterogeneous solids. Comput. Meth. Appl. Mech. Engng. 172, 3–25.

Oden, J.T., Zohdi, T.I., 1997. Analysis and adaptive modeling of highly heterogeneous elastic structures. Comput. Meth. Appl. Mech. Engng. 148, 367–391.

Pagano, N.J., Rybicki, E.F., 1974. On the significance of effective modulus solutions for fibrous composites. J. Comp. Mat. 8, 214–228.

Parton, V.Z., Kudryavtsev, B.A., 1993. Engineering Mechanics of Composite Structure. CRC Press, Boca Raton, FL.

Paulino, G.H., Menezes, I.F.M., Cavalcante Neto, J.B., Martha, L.F., 1999. A methodology for adaptive finite element analysis: towards an integrated computational environment. Comp. Mech. 23, 361–388.

Rank, E., Babuska, I., 1987. An expert system for the optimal mesh design in the h–p version of the finite element method. Int. J. Numer. Meth. Engng. 24, 2087–2106.

Robbins, D.H., Reddy, J.N., 1996. An efficient computational model for the stress analysis of smart plate structures. Smart Mater. Struct. 5 (3), 353–360.

Sanchez-Palencia, E., 1980. Non-homogeneous Media and Vibration Theory. Lecture notes in Physics, vol. 127., Springer, Berlin.

Sun, C.T., Chen, J.L., 1991. A micromechanical model for plastic behavior of fibrous composites. Comp. Sci. Tech. 40, 115–129.

Suquet, P., 1985. Local and global aspects in the mathematical theory of plasticity. In: Sawczuk, A., Bianchi, G. (Eds.), Plasticity Today – Modeling Methods and Applications, Elsevier, London.

Suquet, P., 1987. Elements of homogenization theory for inelastic solid mechanics. In: Sanchez-Palencia, E., Zaoui, A. (Eds.), Homogenization Technique for Composite Media, Springer, Berlin, pp. 194–275.

Terada, K., Kikuchi, N., 1995. Nonlinear homogenization method for practical applications. In: Ghosh, S., Ostoja-Starzewski, M. (Eds.), Computational Methods in Micromechanics, ASME AMD 212, 1–16.

Tvergaard, V., 1982. On localization in ductile materials containing spherical voids. Int. J. Frac. 18 (4), 237–251.

Xie, M., Adams, D., 1995. A plasticity model for unidirectional composite materials and its applications in modeling composite testing. Comp. Sci. Tech. 54, 11–21.

Zhu, J.Z., Zienkiewicz, O.C., 1988. Adaptive techniques in the finite element method. Comm. Appl. Num. Meth. 4, 197–204.

Zhu, J.Z., Zienkiewicz, O.C., 1992. The superconvergent patch recovery and a posteriori error. part 2: error estimates and adapativity. Int. J. Num. Meth. Engng. 33 (7), 1365–1382.

Zhu, J.Z., Hinton, E., Zienkiewicz, O.C., 1993. Mesh enrichment against mesh regeneration using quadrilateral elements. Comm. Num. Meth. Engng. 9, 547–554.

Zohdi, T.I., Oden, J.T., Rodin, G.J., 1996. Hierarchical modeling of heterogeneous bodies. Comput. Meth. Appl. Mech. Engng. 138, 273–298.